Nanoscale examinations on the sequestration of Cu by organic material in contaminated surface soils in Timmins, Ontario

by

Haley Mantha

A thesis submitted in partial fulfillment
of the requirements for the degree of
Master of Science (MSc) in Chemical Sciences

The Faculty of Graduate Studies
Laurentian University
Sudbury, Ontario, Canada

THESIS DEFENCE COMMITTEE/COMITÉ DE SOUTENANCE DE THÈSE
Laurentian Université/Université Laurentienne
Faculty of Graduate Studies/Faculté des études supérieures

Title of Thesis
Titre de la thèse: Nanoscale examinations on the sequestration of Cu by organic material in contaminated surface soils in Timmins, Ontario

Name of Candidate
Nom du candidat: Mantha, Haley

Degree
Diplôme: Master of Science

Department/Program
Département/Programme: Chemical Sciences

Date of Defence
Date de la soutenance: July 24, 2018

APPROVED/APPROUVÉ

Thesis Examiners/Examinateurs de thèse:

Dr. Michael Schindler
(Supervisor/Directeur de thèse)

Dr. Nelson Belzile
(Committee member/Membre du comité)

Dr Graeme Spiers
(Committee member/Membre du comité)

Dr. Eugene S. Ilton
(External Examiner/Examinateur externe)

Approved for the Faculty of Graduate Studies
Approuvé pour la Faculté des études supérieures
Dr. David Lesbarrères
Monsieur David Lesbarrères
Dean, Faculty of Graduate Studies
Doyen, Faculté des études supérieures

ACCESSIBILITY CLAUSE AND PERMISSION TO USE

I, **Haley Mantha**, hereby grant to Laurentian University and/or its agents the non-exclusive license to archive and make accessible my thesis, dissertation, or project report in whole or in part in all forms of media, now or for the duration of my copyright ownership. I retain all other ownership rights to the copyright of the thesis, dissertation or project report. I also reserve the right to use in future works (such as articles or books) all or part of this thesis, dissertation, or project report. I further agree that permission for copying of this thesis in any manner, in whole or in part, for scholarly purposes may be granted by the professor or professors who supervised my thesis work or, in their absence, by the Head of the Department in which my thesis work was done. It is understood that any copying or publication or use of this thesis or parts thereof for financial gain shall not be allowed without my written permission. It is also understood that this copy is being made available in this form by the authority of the copyright owner solely for the purpose of private study and research and may not be copied or reproduced except as permitted by the copyright laws without written authority from the copyright owner.

Abstract

The deposition and alteration of particulate matter (PM) in soils is a world-wide health concern. This study investigates the fate of Copper in organic-rich surficial soil layers (0-5 cm) contaminated by mining related activity at the Timmins Kidd Creek metallurgical site, Canada. The sequestration and mobilization of Cu by organic material (OM) in the soil layer is investigated using focused ion beam (FIB) technology and transmission electron microscopy (TEM). Copper occurs as incidental metallic Cu and covellite (CuS) nanoparticles (NPs), formed via ion reduction by humic substances and magnetite. Additionally, TEM analysis of the colloidal fraction, extracted via ultracentrifugation from the surface soil layer, indicates the occurrence of incidental covellite NPs in close association with dissolved OM. This study shows for the first time that Cu is sequestered as incidental metallic Cu and covellite NPs within OM and magnetite in surficial organic-rich soil layers. Furthermore, the mobility of Cu is facilitated through the transport of covellite nanoparticles embedded within organic colloids.

Keywords: Metallic, Copper, Covellite, Incidental, Nanoparticles, Particulate matter, Transmission electron microscopy, Organic material, Humic substances, Magnetite, Mobile, Sequester, Timmins, Kidd Creek

Co-Authorship Statement

Chapter 1 of this thesis is meant to provide background information of main topics discussed in this study. It includes both a review of past and current literature as well as an introduction into the main instrumental technique employed. While Michael Schindler assisted with the outline and offered edits, I am the sole author of the chapter.

Chapter 2 of this thesis is to be submitted to the peer-reviewed journal, Environmental Science: Processes and Impacts. Additionally, a portion of this chapter was presented at the American Chemical Society conference (2018). I am the first author and Michael Schindler is the second author. The third author, Michael F. Hochella (Virginia Polytechnic Institute; Pacific Northwest National Laboratory), has contributed nanoscale analyses and interpretations of sections in this study.

Chapter 3 of this thesis offers a general conclusion as well as a section regarding future work which can aid researchers in this area of study. I am the sole author of this chapter with input from Michael Schindler.

I acknowledge that this statement is correct.
April 25, 2018

Michael Schindler

Acknowledgements

I would like to start by thanking my supervisor, Dr. Michael Schindler, for his constant support and guidance. As I experienced many new challenges researching a branch of chemistry I was not accustomed to, your patience and assistance was greatly appreciated. I also want to thank you for making this project very interesting and allowing me to become familiar with new techniques and experiences. The processes capable of occurring at the nanoscale will forever intrigue me, and I will always dream about the perfect lattice fringe.

I would also like to thank my committee members, Dr. Nelson Belzile and Dr. Graeme Spiers. I appreciate the numerous insights you have provided me, as well as allowing me to audit your classes. Additionally, a big thank you to Dr. Spiers for the assistance and various tips on soil sampling and analysis procedures. Thank you to the Goodman School of Mines for their generous scholarship, as well as the Chemistry/Biochemistry department for my awarded bursaries.

Of course, without the support of the technicians, this project would not have gone as smoothly as it did. Each technician in the Laurentian chemistry department has helped me in some way, from advice to reassurance or to lending me their equipment. Additionally, the Earth Sciences technicians, Willard Desjardins, Dr. William Zhe, and Rémy Poulin, were also a great help. I am also very thankful for the associates at Virginia Tech for their expertise in regard to sample preparation, analysis, and interpretations.

Finally, I would like to thank my entire, outstanding family. This includes my immediate and extended family, my boyfriend, and my friends who are considered family. Every single one of you have always believed in me and never stopped encouraging me to reach my full potential. To my mom, dad, brother, and gramma: you continue to inspire me, and for that I am thankful.

Table of Contents

List of Tables

List of Figures

List of Appendices

List of Abbreviations

BF	Bright Field
BSE	Backscattering Electron
CEC	Cation Exchange Capacity
DOM	Dissolved Organic Matter
EDS	Electron Dispersive X-Ray Spectroscopy
EELS	Electron Energy Loss Spectroscopy
Eh	Reduction Potential
EXAFS	Extended X-Ray Absorption Fine Structure
FA	Fulvic Acids
FFT	Fast Fourier Transformations
FIB	Focused Ion Beam
HA	Humic Acids
HAADF	High Angle Annular Dark Field
HS	Humic Substances
ICP-MS	Inductively Coupled-Plasma Mass Spectrometry
MSC	Mineral Surface Coatings
NP	Nanoparticle
OM	Organic Material
PM	Particulate Matter
PZC	Point of Zero Charge
SAED	Selected Area Electron Diffraction
SEM	Scanning Electron Microscopy
SOM	Soil Organic Matter
STEM	Scanning-Transmission Electron Microscopy
TEM	Transmission Electron Microscopy
WDS	Wavelength-Dispersion Spectroscopy
XRD	X-ray Diffraction
μ-XRF	Micro X-ray Fluorescence

Chapter 1

1.1 Soil contamination by mining-related activities

Industrial processes, especially mining and smelting activities, have contaminated the air, soil, and water around the world.[1] Common pollutants released from mining activities primarily include particulate matter (PM) and aerosols. Many studies have been conducted on contaminated soils at various locations for the purpose of determining the magnitude and type of contamination,[2-5] the bioavailability of metal(loid) species,[6-8] and to establish in-depth characterization of the interactions and processes that occur between PM and soil constituents.[9-12]

1.1.1 Particulate matter

As already noted, the occurrence and processes of PM has been extensively characterized by many researchers. Despite this, continuous research is required on this particular topic as the reactions and consequences of PM are extremely diverse and differing environmental conditions will influence the processes that take place. Reclamation strategies may be employed in areas with significant contamination, but in order for these processes to be effective, appropriate strategies must be applied. Knowledge on the lifecycle of PM is important to assess the environmental fate and impact in different localities so that appropriate remediation efforts are taken. The stages of PM include formation, release, transport, deposition, and finally weathering and dissolution. Particle formation processes have significant control on the final fate and environmental impact as it determines the structure and composition of the contaminant.

1.1.1.1 Smelter-derived particles

Prior to the onset of strict environmental regulations, companies did not employ the use of filters for smelter stacks which led to the significant release of smelter-derived particles.[3] Despite the introduction of equipment for flue gas cleaning, a small fraction of particulates are still released by stacks in times of filter degradation.[9] Characterized as being spherical in shape with high-temperature features, including dendritic, skeletal, tabular, and porphyritic patterns, these particles are composed of various metal(loid)s that can become mobile in the soil environment.[11] Smelter-derived particulates are produced during high-temperature smelting processes and the subsequent cooling process where metal(loid)s are quenched into small melt droplets through collisions between solid and liquid particles or through gaseous condensation processes.[13] Metal(loid) composition and structure is therefore dependent on furnace temperatures and methods used, as well as the physical material processed within the smelters.

1.1.1.2 Windblown dust

Unlike particulates derived from the smelting-processes, angular or irregular shaped particulates observed in soils often originate from tailing sites or waste piles. Hence, their formation and their aeolian transport from ore and waste-rock piles is related to daily mining operations. These particulates contain minerals formed during (a) the ore formation process, (b) the weathering of the ore in the vadose zone of the ore deposit, (c) ore processing processes, or (d) the weathering of ore and waste rock piles.[9] The particulates often undergo alteration processes in soils such as oxidation and dissolution–precipitation and consequently exhibit noticeable weathering rims.[9] The chemical and mineralogical composition and susceptibility for weathering of wind-blown particulates will affect the fate of their released metal(loid)s upon soil deposition.

1.1.2 Contaminant deposition

Upon contaminant release to the atmosphere, the resultant spatial distribution is dependent on particle size and the wind direction/speed. Smaller particulates travel further than their larger counter-parts, however distance can be impeded by structural obstacles such as buildings or trees.[5,14,15] A variety of processes can occur upon the deposition of PM into soils, the results of which are primarily dependent on the composition of the contaminant and the surrounding environmental conditions. Of these, the principal factors that determine the fate of PM revolves around the constituents of the soil matrix, as this will define the pH, reduction potential, and complexing agents (Section 1.3).

Elements released during the weathering of PM have been shown to be limited within soil profiles as they are primarily retained by the surficial soil layers.[16-18] Because of this, concentration depth-profiles generally show an exponential decrease of metal concentration when contamination is attributed to anthropogenic, airborne deposition. However, total metal concentration is not directly related to the concentration that can harm biological species.[19,20] While most metal(loid)s are sequestered in a bio-unavailable form, over time these metals can be released during weathering of their host phases. The extent and speed of this weathering process must be determined for individual minerals and environmental conditions in the corresponding soils, which is the primary reason why this area of research must be consistently investigated. For example, delafossite ($Cu^{1+}Fe^{3+}O_2$) has been shown to be quite stable under short-term weathering conditions,[21] however Lanteigne *et al.* reported significant weathering of this mineral in smelter-contaminated soils of the Sudbury area.[11]

1.2 Kidd Creek complex

Base metals, including copper (Cu), zinc (Zn), lead (Pb), and nickel (Ni), are important commodities for commercial and industrial purposes. In Canada, Cu is the second most common element mined and produced, only falling behind iron.[22] A prominent mining complex in Canada, the Kidd Creek mine site, is the deepest base metal mine in the world and is located 20 km North of the Timmins city center. The ore mined at this site includes chalcopyrite ($CuFeS_2$), pyrite (FeS_2), pyrrhotite ($Fe_{(1-x)}S$ x=0-0.2), sphalerite (ZnS), and galena (PbS), all hosted in felsic rocks.[23] The metallurgical site, located 27 km South-East of the mine, was closed in 2010 after being in operation for 30 years. A Cu and Zn smelter operated in the lower SE section of the complex prior to its closure. The copper smelter was based on the Mitsubishi smelting process which utilized three furnaces, with a typical temperature of 1200-1270 °C.[24] High-temperature features within spherical particulates identified within nearby soils are attributed to this process while angular or irregular-shaped anthropogenic grains found in nearby soils likely originated from ore and waste rock piles within the complex (this study).

In 2003, the prevailing wind direction in Timmins was from the North-West and North.[25] This suggests that the largest amount of PM wind-blown from the metallurgical site would have been predominantly deposited SE to S. The soils in this area are from glaciolacustrine fine-grained deposits[26] and exhibit well-defined profiles, provided they are undisturbed. The chemistry and processes that can occur within these soils are discussed in the next section.

1.3 Soil chemistry

Soil is an extremely complex matrix with many different layers, constituents, and properties. In addition to this, soils derived from different geographic locations or even local environment variances will result in a matrix with distinctive properties. In undisturbed areas, soil may exhibit discrete horizons to form a soil profile. These horizons can be classified by their colour, texture, and most importantly, their composition. A complete discussion of soil profiles is beyond the scope of this review and therefore, for the purposes of this review, only the topsoil will be discussed in depth. While topsoil is roughly defined as the uppermost layer of soil, clear inconsistencies of exact depth is demonstrated in the literature as some researchers define a depth value while others consider the natural horizons developed in the profile.[2,5] In this study, we have defined the upper 0-5 cm organic layer as the topsoil, where the organic-rich fraction was the predominant constituent.

As is common with soils, the composition of surficial soils is extremely diverse. In general, these components can be divided in three fractions: biological, inorganic, and organic species. Biological species of course refer to living organisms such as earthworms or microbial activity. The mobility and diversity of these species greatly impact the chemistry of soils as they can consume, alter, and deposit natural and anthropogenic material. However, earth worms are not always present in certain soil types or localities, and therefore the mobility of metals in areas with earthworm activity may be different than areas without these species. The inorganic components include mineral groups such as feldspars, clay minerals, and aluminum/manganese/iron oxides, all of which have their own chemical and mineralogical properties and therefore affect the soil chemistry in different ways. The third component of typical topsoil is the organic fraction, which is the matrix in focus of this thesis.

The organic fraction is composed of both soil organic matter (SOM) and organic residues, which are any undecayed plant and animal tissues or their partial decomposition products. Soil organic matter is a broad term that includes both humic substances (HS) and non-humic substances, but does not include organic residues. Humic substances is a generic term that includes many high-molecular weight substances formed by secondary synthesis reactions.[27] They are arguably the most important component of the organic fraction and as such will be covered in depth below. Non-humic substances are comprised of a variety of biochemical compounds including, but not limited to, amino acids, carbohydrates, and organic acids. The reduction potential (Eh) is a very important parameter that defines the chemistry of a soil, indicating whether a given soil is reducing or oxidizing. While the overall reduction potential is not controlled by SOM, it can contribute reducing capabilities of a soil layer (Section 3.2.2).

Soil organic matter influences soil chemistry in many ways through both its existence and decay. Soils high in SOM may demonstrate great buffering activity which prevents large pH variations. Similarly, SOM significantly increases the cation exchange capacity (CEC) of a given soil, which influences the ability to hold nutrients and also contributes to the buffering capability of SOM. Upon decomposition, SOM yields important polyvalent ions and molecules such as carbon dioxide (CO_2), ammonium (NH_4^+), nitrate (NO_3^-), phosphate (PO_4^{3-}), and sulfate (SO_4^{2-}).[27]

Soil does not only contain solid material, but also liquids and gases. Through the structure of a soil profile, there are many pore spaces of varying sizes creating a nano- and micro-environments. The chemistry within these pore spaces often cannot be represented by the bulk chemistry of a soil due to the occurrence of chemical and mineralogical reactions at solution-particle interfaces. Soil pore water facilitates the transport of natural and anthropogenic material. As such, researchers often consider the chemistry of the pore water to be representative of the bulk

chemistry of a given soil by measuring the soil pH, reduction potential, and dissolved organic matter (DOM). Within pore spaces, DOM may comprise a significant component of the soil pore water. This type of organic matter is composed of organic acids or HS that can pass through a 0.45 μm filter. As will be later discussed, DOM plays an important role in the mobility of contaminants by ways of adsorption and incorporation.

1.3.1 Humic substances

Major components of SOM are the heterogeneous, high molecular weight humic substances which can be subdivided into humic acid (HA), fulvic acid (FA), and humin. These divisions are based on the relative solubility of the different components, where HAs are soluble under alkali conditions, FAs are soluble under acidic conditions, and humin are not soluble under either acidic nor alkaline conditions.[27] The formation of these substances can be attributed to different pathways, however they are all derived from the slow decomposition of plant residues.Aquatic HS can be derived from the decomposition of algal or bacterial residues.[28] While soil HS contain more aromatic functional groups, those derived in aquatic environments generally contain more aliphatic groups due to the organic precursor.[28]

The most reactive components of organic matter are HAs and FAs. The reactivity of these acids is attributed to their solubility and the high density of available functional groups such as carboxyl and phenolic groups.[29] As there is a higher proportions of acidic functions groups on FAs, they demonstrate a higher total acidity than HAs.[27]

Other functional groups include enols and quinones (acidic), alcoholic and carbonyls (neutrals), and amines and amides (basic).[27] Because of their reactive capabilities, HS has a strong influence on the mobility of free and complexed metal species by a variety of mechanisms. As a

note, some authors consider humic substances an artifact of extraction, while some authors believe they do occur in the environment.[30]

1.3.2 Interactions of soil components with metal species

Upon weathering of PM, metal(loid)s will be released and enter the soil pore water. Various soil constituents can subsequently bind the metal(loid)s through different mechanisms. Metal(loid)s can be sorbed to surfaces by physical or chemical interactions. Physical interactions include van der Waals forces and electrostatic forces, which in addition to hydrogen bonds, occur predominantly as outer-sphere complexes.[31] As these interactions are considered to be relatively weak, formation of outer-sphere complexes occurs rapidly and is reversible.[27] Conversely, adsorption through the formation of chemical bonds between substrate and sorbent occurs through inner-sphere complexations, a process often considered to be irreversible in the environment. Another process considered irreversible is isomorphic substitution of a trace metal where similarly-sized atoms replace the original atom within a mineral lattice (ie. Zn^{2+} substituting Fe^{2+} in Fe-oxides).[32] The type of adsorption or incorporation mechanism that occurs is often dependent on a number of factors including the pH and ionic strength of the solution as well as the properties and surface loading capability of a given sorbent.[27] For example, inner-sphere complexes involving cations are dominant in solutions with a higher pH and ionic strength (pH 7 vs. 6).[33]

One of the main properties that dictates binding is attributed to the surface charge of sorbents, a value based on a given point of zero (pzc) charge due to surficial functional groups. The pzc of a compound corresponds to the pH value where the net surface charge density is zero. Hence, when the pH is less than a given pzc, the compound is positively charged, and if the pH is greater than the pzc, the surface charge is negative. Because the majority of functional groups on

HS are carboxyls and phenolic groups, the typical pzc value of most organic based compounds in soil is 2-3, indicating that surface charge of organic material at pH values typical for soils (pH > 4.5) will be negative.[27,34] This allows for significant electrostatic interactions between organic material and cationic species in the pore solution.

While Ca^{2+} is abundant in soil solutions, trace metals such as Cu^{2+} and Pb^{2+} have been demonstrated to preferentially sorb to the negative binding sites on SOM.[35] In fact, many studies have indicated that trace metals such as Cu^{2+} are predominantly sequestered by organics.[36-40] Other researchers have found contradicting results where Cu^{2+} was found to be preferentially bound to Fe-(hydr)oxides.[41,42] This contradiction is a result of the interpretation of extended x-ray absorption fine structure (EXAFS) data. Here, Yang *et al.*[42] argued that similar bond lengths between Cu-O and Cu-N can lead to false conclusions with respect to the bonding of Cu to organic matter. The authors therefore used a combination of EXAFS and micro x-ray fluorescence (μ-XRF) to study the occurrence of Cu in contaminated soils. Their study indicated that Fe-(hydr)oxides were the dominant host for Cu in contaminated mineral soil. However, the authors indicated that the soils analyzed in their study had a much lower SOM amount compared to previous studies (0.55 % vs. 2.2-75 %).[38-40] Hence, the authors suggested that at low SOM content, Cu would bind predominantly to Fe-(hydr)oxides.[43] Studies have shown that Cu primarily binds to Fe-(hydr)oxides through inner-sphere complexations which suggests a stronger retention of Cu by Fe-(hydr)oxides than by organic material, where Cu appears to be more weakly bonded.[42,44,45]

Not only can binding mechanisms cause metal immobilization, they can also influence the properties of minerals or induce speciation changes. The sorption of different constituents to others (ie. DOM onto the surface of Fe-(hydr)oxides) can alter the surface reactivity of the sorbent.[46] Additionally, surface precipitation processes can lead to the formation of metal-bearing phases on

the sorbent surface.[47] This mechanism typically only occurs when there is a high coverage of metal species sorbed to a surface. Contrary to this, when there is a low surface coverage, complexation is more likely to occur.[48] Not only do surface precipitates influence the speciation of a metal, they also result in the modification of the surface properties which can affect subsequent binding of the mineral to solute in solution.

The speciation of metal ions can also be changed by sorption onto specific functional groups of HS that are capable of inducing reduction. Redox-active moieties on HS have been demonstrated to accept electrons from microorganisms in the soil and then subsequently donate those electrons to metal species.[49] The functional groups that exhibit this redox activity are quinone-hydroquione and phenolic moieties.[50,51] Both soil and aquatic HS have been shown to induce the reduction of many metal species, including the formation of metallic species.[28,49,52-54]

1.3.2.1 Factors that influence metal mobility in soils contaminated by atmospheric deposition

In addition to the sorption of metal(loid)s to OM and mineral surfaces, their chemical distribution in the soil profile is also controlled by the sorption of PM onto surficial soil constituents (ie. organic material). This sorption prevents the mobilization of smaller PM and therefore limits exposure to pore waters. The mobility of metal(loid)s or metal(loid)-bearing PM in the soil profile depends on many factors such as grain size, surface charge, pH, Eh, bacterial activities, and type of organic matter and DOM. For example, DOM has significant influence on metal mobility as it can strongly bind metals and, due to their nanometer size, be easily mobile in the soil profile upon release.[27] Additionally, DOM can also sorb to mineral surfaces. High DOM loading on mineral surfaces leads to coatings which alter the surface composition and charge. When this occurs, the surface charge of the DOM coated mineral can become neutral or even reversed, depending on the soil pH

and the type of adsorbed DOM.[46] Mineral surface coatings composed of DOM may lead to higher cation retention, especially under acidic conditions where the surface of the coated mineral is commonly negatively charged.[55]

Colloid-facilitated transport has been demonstrated to be an important mechanism for metal mobility. The efficiency of this transport mechanism depends on the stability and relative mobility of a given colloid, as well as its surface area and charge.[4] While the charge of a given colloid is generally controlled by the pzc, its charge may be modified by the adsorption or formation of DOM or Fe-(hydr)oxide surface coatings.[46] These coatings commonly increase the relative stability of a colloid[55] but can also result in an increase of the metals adsorbed or incorporated into the colloid. An important mechanism of colloid release can be attributed to heavy rainfall or upon the snow-melt in spring, as this instigates a significant influx of low ionic strength water causing a decrease in chemical and physical forces, thus favouring the release of colloids attached to larger particles.[56]

To summarize, transport and retention mechanisms of metals are influenced by many different variables such as the soil pH, Eh, constituents present, as well as the composition of the particulate being weathered. These variables are so diverse, even within one location, that mechanisms of metal mobility cannot be generalized for soils contaminated by atmospheric deposition of metal(loid)-bearing PM. Furthermore, the size and diversity of surface binding sites and colloids commonly limits an in-depth characterization using bulk analytical tools such sequential extraction methods and synchrotron-based spectroscopy methods. Hence, nanoscale analysis techniques such as transmission electron microscopy are often required to truly understand retention, mobility, and speciation of metals in the environment.

1.4 Transmission electron microscopy

The study of environmental processes often requires the application of many techniques to fully characterize basic to complex features in the collected samples which can reveal past or present processes. An important subsection of analytical instruments involves the use of an electron beam to form images or to produce secondary radiation (electrons or x-rays). The greatest advantage of electron beam instruments is the ability to focus on and discern nanoscale components within a sample, which cannot be accomplished using bulk analytical methods. The in-depth characterization of a distinct specimen on the nanoscale can be achieved with transmission electron microscopy (TEM). The difference between TEM and other electron beam techniques is its ability to observe and identify features on the 10^{-9} to 10^{-6} meter-scale. Scanning electron microscopy (SEM) is primarily used to characterize samples at the micrometer scale (10^{-4} to 10^{-2} m). The characterization of a sample with SEM is often an important step prior to TEM analysis as it ensures that the area selected for TEM analyses is representative. Transmission electron microscopy is not a routine method for contaminant characterization due to both cost and the requirement for skilled operation. Nonetheless, more researchers are beginning to apply this technique to evaluate environmental processes and impacts of PM. In fact, without the use of TEM, researchers would not have identified toxic, incidental titanium oxide phases in air, soil, and water around the world.[57-59] Scanning-TEM (STEM) combines the capabilities of SEM and TEM, allowing for the analysis of thin samples by the addition of scanning coils and appropriate detectors. Transmission electron microscopes can either be a hybrid of TEM and STEM or they can be a dedicated STEM. In STEM mode, a small electron probe is scanned over the specimen in a raster pattern and the transmitted electrons are collected.[60] For simplicity purposes, only the TEM acronym will be used for the remainder of this chapter.

The basis of TEM relies on the detection of various electron-specimen interactions. As shown in Figure 1, there are many scattering events that can occur upon the interaction of an electron beam with a sample, however not every event may be possible or detected in a single analytical technique. For imaging purposes in TEM, only electrons that are transmitted through the specimen are detected and translated into an image.[60] Both the direct and diffracted electron beam can form an image and beam selection determines the imaging mode. Most transmission microscopes also have an attached detector for the purpose of chemical analysis which can acquire and quantify either incident x-rays or electrons, dependent on the detector.

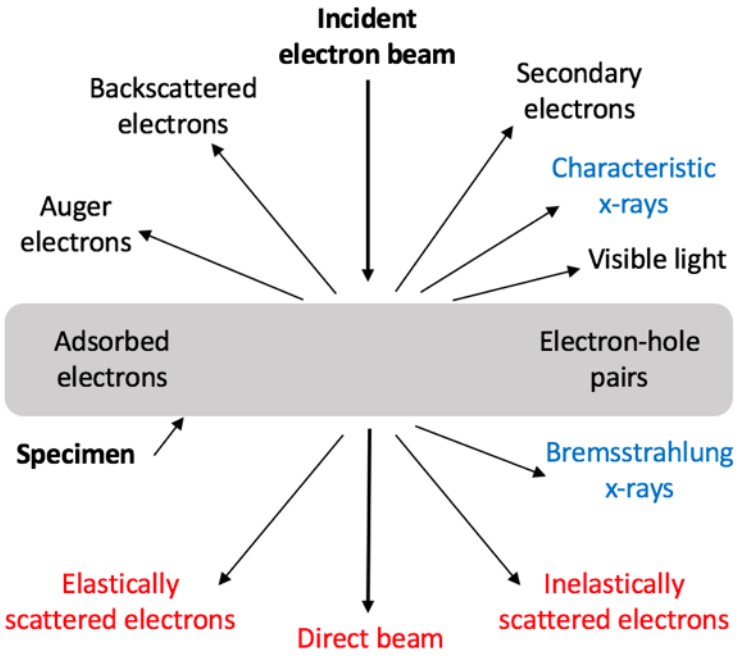

Figure 1. Possible scattering events that can occur in electron beam analysis. Red text indicates important scattering events for TEM imaging and blue text indicates important scattering for EDS quantification. Adapted from [60].

Electron dispersive x-ray spectroscopy (EDS) quantifies characteristic x-rays released from a specimen upon electron bombardment. When an incident electron knocks out an inner shell electron, an electron in an outer shell will fill the vacancy. As an electron is moving from a higher energy to a lower energy shell, the energy difference that is associated with this transition is released as a characteristic x-ray.[60] Emitted x-rays have an energy that correspond with the element

it originated from and the specific electron transition that transpired, involving the shell and subshell of both the electron hole and of the location where the electron transferred out.[61] The data is plotted as energy versus intensity and the characteristic spectral lines are superimposed onto the background represented by the bremsstrahlung pattern, which is formed by the energy loss of the direct beam through the deceleration of the incident electron.[60]

Electron energy loss spectroscopy (EELS) is a method that quantifies the energy distribution of inelastically scattered electrons produced and transmitted during the interaction of the direct beam with the electrons in a specimen. The quantified energy is related to the local environment of the electrons that interacted with the primary beam and therefore information about the chemical and physical properties of a given area of the specimen can be gained.[62] Like the requirements for TEM, the application of EELS requires thin samples for sample analysis.

1.4.1 Imaging modes in TEM

Nanoscale analysis using TEM can be accomplished by a variety of methods. As noted above, chemical data can be gathered using EDS or EELS, however morphological and mineralogical data can also be gathered through various imaging modes (Fig. 2). Upon the interaction between the incident electron beam and the sample, the diffracted electrons pass through an objective lens that focusses the electrons onto the back focal plane of the instrument, producing a diffraction pattern.

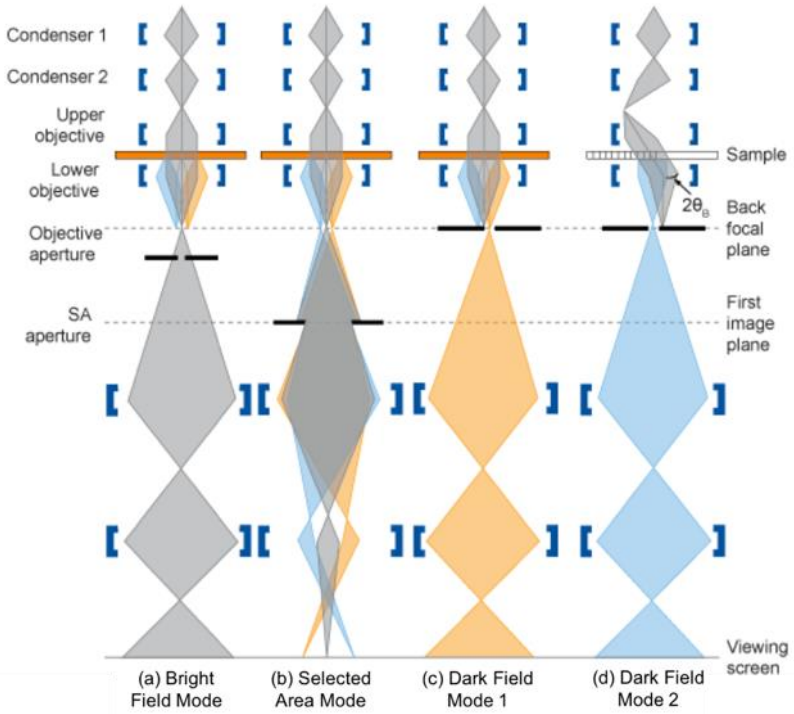

Figure 2. Beam paths for the different operational modes of TEM. The directly transmitted beam is represented by the gray line and the diffracted beams are shown by the blue and yellow lines. Adapted from [63].

In conventional imaging, an objective aperture is inserted near the back focal plane to select a single beam of electrons, and its exact location defines the type of imaging mode. A bright field image (BF) is created by placing the objective aperture below the back focal plane. This creates an image of the transmitted beam (Figure 2a) in which darker and brighter tones defines areas of high and low interaction between the primary beam and the atoms in the sample, respectively. Dark field (DF) imaging is accomplished by obstructing the beam that is not diffracted and collecting only the diffracted electrons for image formation, which can be accomplished by two methods.[63] Dark field mode 1, shown in Figure 2c, occurs when the objective aperture is positioned so that it excludes the transmitted beam but allows for a portion of the diffracted beam to pass through. Dark field mode 2 occurs when the incident electron beam is tilted prior to interaction with the specimen causing the beam path of the un-diffracted electrons to be blocked by the objective aperture, allowing the electrons that are diffracted along a specific angle to travel along

the central axis to pass through the aperture (Figure 2d).[63] As such, darker and brighter tones in the DF image represent low and high interactions with the specimen, respectively.

If the objective aperture is removed, both the transmitted and diffracted beam will be allowed to pass through the column (Figure 2b). When the diffracted and transmitted electrons are allowed to pass through the column, interference between the diffracted electrons results in a diffraction pattern on the viewing screen.[60] These diffraction patterns are formed by electrons that are diffracted by a regular array of atoms in a crystal,[64] following Bragg's law:

$$n\lambda = 2dsin\theta \qquad \text{Eqn. 1}$$

where n is the order of diffraction, λ is the wavelength of the incident electrons, d is the lattice spacing between planes, and θ is the incident angle of the electrons.[60] Additionally, because diffraction patterns are caused by interference between coherently scattered waves, to have a strong diffraction signal, the waves must be in phase to allow for constructive interference.[65]

The addition of a selected area (SA) aperture allows the recording of a diffraction pattern from a site-specific location through blocking electrons from the surrounding sample. Recording selected area electron diffraction patterns allows for the identification of larger nanoparticles or an assemblage of smaller nanoparticles with diameters as small as d = 170 nm.

1.4.2 Focused ion beam technology

Samples that are analyzed using TEM must be extremely thin (< 100 nm) for basic operation as the various imaging modes rely on the physical transmission of the incident electron beam. If samples are too thick, incident electrons will only undergo alternative interactions with the specimen (e.g. become backscattered or form secondary electrons). As such, specific sample preparation techniques are required to ensure electron transparency. There are multiple methods

that can be chosen for sample preparation and the method selected is often dependent on the characteristics of a given sample (hard vs. soft, inorganic vs. biological). For samples that are composed of soft material, a common, inexpensive approach is the use of an ultramicrotome, which allows the slicing of electron transparent sections with a diamond or glass knife. However, for environmental soil samples with a mineral component, the use of an ultramicrotome is limited due to the hardness of many soil components (e.g. quartz with a hardness of 7). An alternative method is the use of focused ion beam (FIB) technology. Despite the high costs and skills required for preparation, this technique is often selected due to its high specificity and versatility. Unlike the preparation of a sample with an ultramicrotome, FIB sectioning is site specific as it allows the selection of the area prior to extraction. The examination of a FIB section with TEM allows researchers to study chemical, mineralogical, and textural features of a specific micrometer-size area in a chemical and geological sample.

The preparation of FIB sections is achieved with an instrument combining FIB and SEM. The FIB component in this instrument is used to extract and mill out the section. The SEM component is used to monitor the extraction and milling process. Although there are different methods for FIB preparation, this discussion is focused on the lift-out technique which can be broken into two main sections: trenching and thinning (Fig. 3). At the first stage, the operator deposits Pt glue over the area of interest for protective purposes. A beam of Ga^+ ions is subsequently used to mill out trenches on either side of the sample; i.e. a few microns underneath the platinum glue and at the boundary between the desired area and the bulk material. The section is removed from the bulk material using a nanomanipulator needle and then mounted onto a holder. Using a low current beam of Ga^+ ions with a small incident angle, the section is subsequently milled down to electron transparency.

In any sample preparation procedure, the production of artifacts is a serious issue. During FIB extraction, artifacts are formed through the deposition of Ga^+ or Pt within soft material, the removal of water from hydrous phases, or the creation of an artificial topography. The deposition of metallic Ga often occurs within soft phases but can be identified through the analysis of diffraction patterns with TEM. In some cases, the bombardment of a sample with Ga^+ ions can result in phase transformations such as the formation of $FeGa_3$ precipitates upon reaction of the Ga^+ ions and Fe in a sample.[66] Dehydration of a hydrous phase commonly occurs under vacuum in the FIB-SEM or TEM and can be sometimes associated with morphological deformations.[67,68]

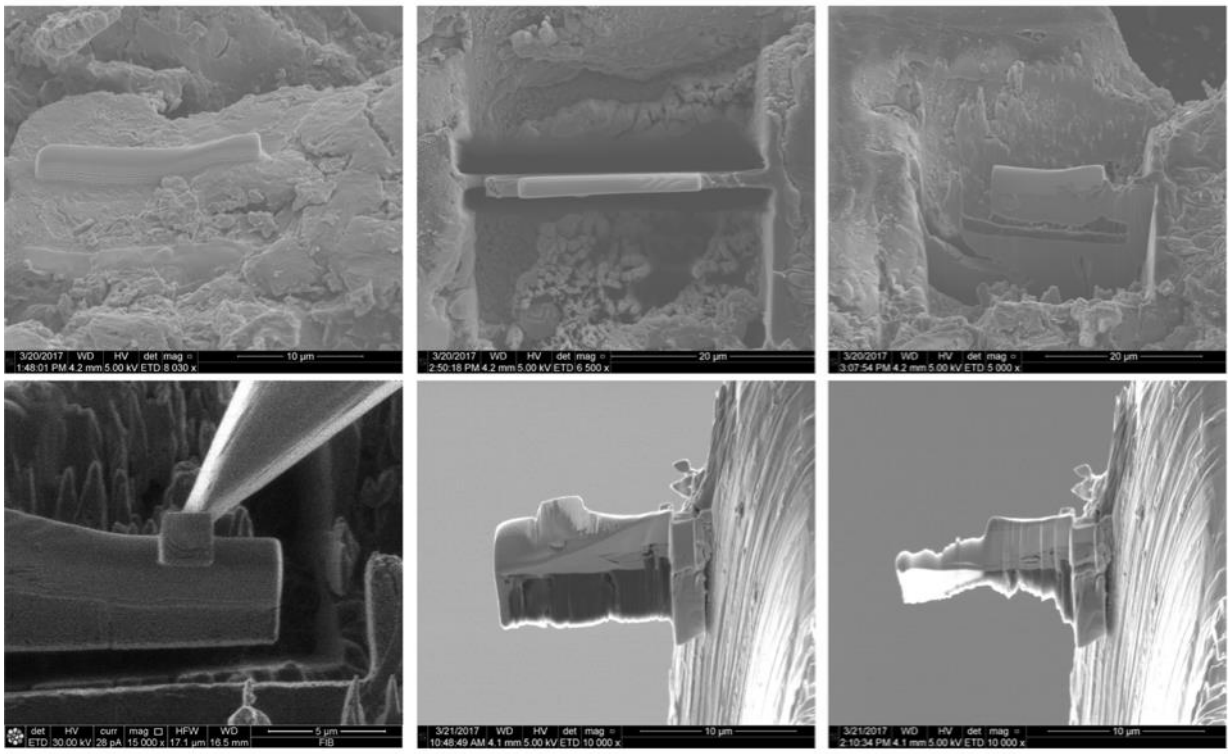

Figure 3. SEM backscattering electron images of the FIB extraction process.

Chapter 2

Abstract

This study investigates the fate of Cu in organic-rich soils contaminated by mining related activities at the Timmins Kidd Creek metallurgical site, Ontario, Canada. The surficial soil layers (top 5 cm) contain on average 13000 ppm Cu, predominantly in the form as Cu-Fe-sulfide PM attached to organic residues. The sequestration of Cu by organic material (OM) is investigated with a combination of focused ion beam (FIB) technology and transmission electron microscopy (TEM). FIB sections are extracted from the interior of OM as well as along the interface between OM and a Cu-Fe sulfide grain. Nanoscale analyses show that Cu occurs as incidental metallic Cu and covellite (CuS) nanoparticles (NPs) within the OM. These NPs can occur along the interface towards the attached Cu-Fe sulfide grain, in remote pore spaces in the interior of the OM, and in association with magnetite precipitates within the OM. These occurrences suggest that Cu is sequestered by OM through various redox and precipitation mechanisms, induced by ferrous iron or humic substances. Additionally, the colloidal (mobile) fraction of the upper 1 cm of the studied soil was extracted through column experiments and ultra-centrifugation. Subsequent TEM examinations indicate that the Cu-bearing colloidal fraction is predominantly composed of incidental covellite NPs embedded within colloidal OM. These observations indicate that Cu is recycled in surficial organic-rich soil through repetition of (a) sequestration processes within OM, (b) decomposition of OM resulting in the release of Cu-bearing incidental NPs, and (c) re-adsorption to newly formed OM as solutes or incidental NPs.

2.1 Introduction

Metal-bearing particulate matter (PM) released from mining related activities are often deposited onto surrounding soils, resulting in elevated concentrations of metals. For example, in 2015, industrial activities just within Canada resulted in the release of approximately 3 million tonnes of PM and aerosols to the atmosphere.[69] Upon deposition, particulates typically remain in the surficial layers of soil, however environmental conditions induce weathering and subsequently the release of metal(loid)s from altered PM surfaces. Processes that drive PM weathering are dependent on the atmospheric and soil matrix conditions, pore water volume, and composition as well as the chemical and mineralogical composition of the particulates.[70]

The majority of studies assessing deposition and fate of PM are primarily focused on spatial distributions or total and bioavailable metal concentrations within soils surrounding a specific contaminant source.[2,10,11,16,71,72] Although these studies are important, they often do not specifically characterize the PM or determine the speciation of the metals within particulates or secondary phases. This characterization is required to understand how metal(loid)s are sequestered and transported within soils, allowing for a better comprehension on the level of contamination as well as providing the capability of designing targeted reclamation strategies. Specific, in-depth characterization of the fate of metal(loid)s in soils can be accomplished using electron beam techniques such as scanning electron microscopy (SEM) or transmission electron microscopy (TEM). For example, Buatier *et al.*[73] used TEM to characterize the speciation of Zn and Pb in smelter-contaminated soils in France. Knight and Henderson[72] characterized smelter dust in humus layers from Rouyn-Noranda using SEM imaging and although they showed evidence of weathering, they did not characterize sequestration and transport of released metal(loid)s. Mantha *et al.*,[74] Lanteigne *et al.*,[10,11] and Caplette *et al.* [75] characterized PM in sandy soils and on rock

coatings around the smelters in Sudbury, ON and Trail, BC (both Canada) using TEM and other techniques to determine mineralogical and chemical compositions, as well as alteration products of PM. Schindler and Hochella[12,57,76] and Schindler *et al*.[77] examined mineral surface coatings (MSC) and mineralized organic matter (MOM) in smelter-contaminated soils in the Sudbury, ON and Trail, BC areas using a combination of the focused ion beam technology (FIB) and TEM. These authors showed that metal(loid)s released by PM are sequestered within pore spaces of MSC and MOM in the form of oxy-salt minerals such as jarosite ($KFe_3(OH)_6(SO_4)_2$) or anglesite ($PbSO_4$) or minerals of the spinel group such as trevorite ($NiFe_2O_4$), gahnite ($ZnAl_2O_4$), and franklinite ($ZnFe_2O_4$).

Classical sequential-extraction methods of organic-rich soils contaminated by atmospheric deposition have suggested that organic material can be an important (even dominant) sorbent for metals in the surface horizons of soils, dependent on the type of organic matter, and the ratio between the total surface areas of organic matter and minerals.[2,47,78] However, synchrotron-based spectroscopy and diffraction studies have not provided a uniform picture of the fate of metal(loid)s in surficial soils containing minerals and organic material (OM). For example, some studies state that Cu predominantly sorbs to OM,[39] whereas other work reports a close association of Cu with Fe-(hydr)oxides.[42] The latter observations indicate an uncertainty with respect to the sequestration of metal(loid)s by OM in soil horizons containing both organic and inorganic material. In an organic-rich environment, metals such as Cu can be complexed by a variety of organic molecules that are derived from the decomposition of natural soil organic matter (SOM). A wide array of compounds form throughout these processes, leading to the formation of humic substances (HS), which are classified as humic acids (HA), fulvic acids (FA), and humin.[79] There are many different organic molecules capable of binding metals and numerous metal-organic interactions can occur,

including inner- and outer-sphere complexation. Carboxylic acid functional groups were found to be important in Cu-HS binding, however the presence of phenolic groups induced an increase in binding strength.[80] However, Cu-HS complexes are heavily dependent on a variety of factors such as the type/origin of the HS, pH, and ionic strength, and therefore the extent of binding is dependent on local conditions.

This study reveals insights into previously unknown sequestration and transport processes of Cu by organic matter and colloids in an organic-rich surficial soil layer in proximity to the former Kidd Creek metallurgical site in Timmins, Ontario. Using a combination of FIB and TEM, this study shows for the first time that Cu-bearing PM is transformed on the surface and within pore spaces of organic material into secondary incidental nanoparticles (NPs) that are composed of metallic Cu and Cu-sulfides. It further shows that Cu can be transported in the colloidal fraction as incidental Cu-sulfide nanoparticles embedded within larger organic colloids.

In this study, organic material is used to describe the overall organic fraction (i.e. organic residues and matter) whereas the term organic matter defines decomposed organic material (i.e. humic substances). Similarly, dissolved organic matter (DOM) is defined as the fraction of organic matter that is capable of passing through a 0.45 μm filter, and therefore is no longer considered particulate organic matter. Additionally, in this study, the colloidal fraction is defined as the fraction that deposits during centrifugation, colloids are considered particles with diameters between 50 and 450 nm and the term nanoparticle is used when particles have diameters smaller than 50 nm.

2.1.1 Environmental Significance Statement

The deposition of metal(loid)-bearing particulate matter (PM) on soils adjacent to and downwind from a contaminant source is a world-wide environmental issue. The exponential decrease in the concentration of metal(loid)s with depth in these soils suggests that they are retained by inorganic and organic constituents in the surficial layers of these soils. An in-depth nanoscale investigation of the interaction of Cu-bearing PM with organic material (OM) in Cu-contaminated soils reveals for the first time that even under oxic conditions in surficial soil layers, the Cu pollutant can be sequestrated by OM in the form of metallic Cu and covellite (CuS) incidental nanoparticles (NPs). Furthermore, this study provides insights into potential mobilization mechanisms for Cu in organic-rich soils as it identifies covellite NPs embedded within mobile organic colloids.

2.2 Materials and Methods

2.2.1 Background information on the Kidd Creek Smelter

The Kidd Creek metallurgical site, located within the city limits of Timmins, Canada, was in operation for 30 years, closing in 2010. The ore processed at this location predominantly contained chalcopyrite ($CuFeS_2$), pyrite (FeS_2), pyrrhotite ($Fe_{(1-x)}S$ x=0-0.2), sphalerite (ZnS), and galena (PbS).[23] The ore was shipped by train from the mine site (27 km away) to the metallurgical site for processing. The Mitsubishi copper smelting process was employed at start-up with furnaces operating around 1200-1300 °C.[24] From 2002-2009, the average amount of total PM (< 100 μm) released to the atmosphere was 844 tonnes/year.[81]

2.2.2 Sample collection

Surficial soil samples (~upper 5 cm) were collected in October 2016 from various sites surrounding the former Kidd Creek smelter. The selected sites exhibited well-developed and undisturbed soil profiles. The surficial sample from site 1 was thoroughly characterized on the nano to micrometer scale (Fig. 4). Site 1, located 10 m from the highway within a birch stand with a grassy understory, exhibits 5 cm of an LFH layer with a 10 cm A_{heg} layer (Fig. S1). Site 2 and 3 were used as control sites, with site 2 exhibiting a 4 cm LFH layer, 6 cm A_{heg} layer, and a 5 cm A_{eg} layer and site 3 exhibiting a 3 cm LFH layer and a 14 cm A_h layer (Fig. S2, S3). Sampling at site 1 continued in May 2017, when samples were collected at 1 cm increments to a depth 10 cm. All samples were transported to the lab in a cooler, dried at 80 °C, sieved (< 1.4 mm), and stored under dry conditions.

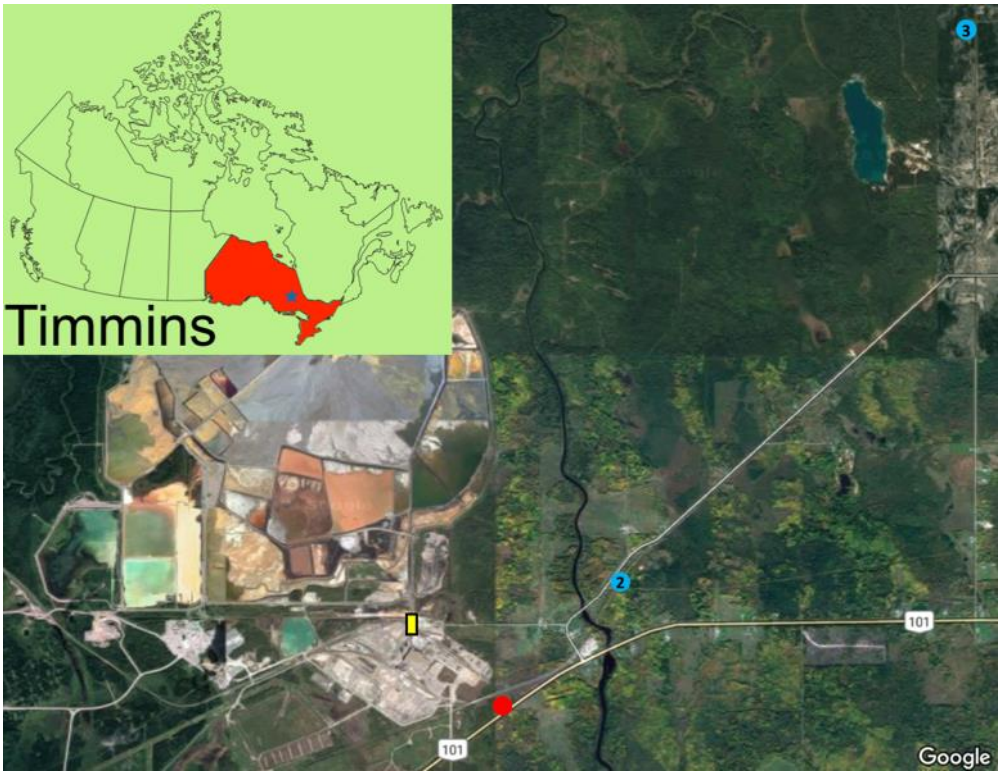

Figure 4. Satellite image of the area surrounding the Kidd Creek metallurgical site; the main sample location is indicated by the red dot and the two control sites are designated and labelled by the blue dots; the yellow rectangle indicates where the copper smelter was located prior to its removal; an inset image shows the location of Timmins within Ontario.

2.2.3 Chemical analysis

Soil pH was measured by mixing 2 g of soil with 10 mL of a 0.01 M $CaCl_2$ solution (1:5 soil:solution ratio). After stirring multiple times over a 30-minutes period, the mixture was allowed to settle for 15 minutes before the pH measurement. Reduction potential was measured in triplicate analysis from five separate wet surficial samples, taken within a 10 x 10 m area at site 1. For the control sites (site 2 and 3), dried and sieved samples were measured. Samples were prepared by mixing 2 g of soil with 10 mL of distilled water, stirred for 5 minutes and allowed to settle for 30 minutes. Samples were then measured using a Ag/AgCl reference electrode which was calibrated with ORP standard. The uncertainty of the measured soil pH and reduction potential are 0.2 units and 10 mV, respectively.

Total carbon and sulfur within the 0-5 cm fraction of site 1 was measured in the Ontario Geological Survey Geoscience Laboratories (Geo Labs) with a LECO CS844. In short, approximately 0.2 g of soil was combusted in a stream of purified O_2 gas and passed over a heated catalyst, oxidizing total S and C to SO_2 and CO_2, respectively, which are then detected by two non-dispersive infrared cells.[82] Total soil digestion and inductively coupled plasma-mass spectrometry (ICP-MS) measurements of the 0-5 cm fractions were completed by Testmark Laboratories with a ELAN DRC II (Perkin Elmer) instrument. Soils were digested using a concentrated HNO_3/HCl mixture, as per the BC SALM protocol[83] and then analyzed using the SW846-6020A method for ICP-MS. Chemical analyses of the samples collected in the depth profiles (ten samples for the first 10 cm and one sample for the 10-15 cm depth) were analyzed at the Geo Labs, Sudbury, ON, Canada. Samples were prepared in a reverse aqua-regia digest following the method of Burnham[84] and analyzed with an iCAP Q ICP-MS (Thermo Scientific).

2.2.4 Preparation of soils for electron microscopy and focused ion beam extraction

The interaction between PM and OM occurs at the nanoscale and can be studied best through the extraction of focused ion beam (FIB) sections along their interfaces. However, extraction and subsequent thinning of a FIB section requires that the area to be extracted is free of fractures or larger pore spaces. From our experience, these topographic homogenous areas can be best located with SEM on surfaces of sand-size grains. Hence, the interaction of PM with OM, including the chemical characterization of PM, were mainly investigated in the fine to coarse sand size fraction (180 μm - 1.4 mm) of the surficial soil layer of site 1. Samples of both the clay to sand size fraction (< 180) and fine sand to coarse sand size fraction (180 μm - 1.4 mm) were embedded into epoxy pucks and then carefully polished to prevent damage or loss of OM.

The diffusion of epoxy into pore spaces stabilizes interfaces between OM and attached minerals which allowed efficient extraction of sections along these interfaces with FIB technology (see below). Some mineral phases may alter under ambient conditions during storage, which may have been limited through the storage of the samples under dry conditions. Significant mineralogical and chemical transformations can occur under high vacuum and exposure to electron- and ion-beams during FIB extraction and TEM usage. Examples of these alterations include the potential for either the removal of phases, phase transformation (e.g. dehydration of hydrous minerals) or deposition of (semi)metallic Ga and Pt nanoparticles in soft materials. These processes have been studied in depth[66-68] and therefore artifact fabrication is carefully considered and caution is taken so that the significance of results is not overstated.

2.2.5 X-ray powder diffraction, scanning electron microscopy, and electron microprobe analysis

Powder X-ray diffraction (XRD) was done with an automated Philips PW3050/60 and PW 1729 X-ray diffractometers using Co Kα radiation (1.79 Å) at a voltage and current of 40 kV and 30 mA, respectively. X-ray diffraction patterns from well-mounted powdered samples were collected over a scan range of 5-65° 2θ with a step size of 0.02° 2θ and a dwell time of 2 s. Chemical analyses of PM were performed with a Cameca SX50 electron microprobe. Data was collected by wavelength-dispersion spectroscopy (WDS) with counting times of 30 s on the peak and 10 s on the background. The operating voltage was 20kV, beam current of 20 nA, and a focused beam of 20 nA. Data reduction was done with a PAP routine[85] using the XMAS software package. Chalcopyrite was used as the standard for Cu ($L\alpha$), Fe ($K\alpha$), and S ($K\alpha$). Characterization of the (semi-quantitative) chemical composition of organic material was accomplished using scanning electron microscopy (SEM) with a JEOL 6400 SEM, operating with an accelerating voltage of 20 kV and a beam current of 1 nA, in combination with energy dispersive X-ray spectrometry (EDS).

2.2.6 Focused ion beam technology and transmission electron microscopy

An interface between a sulfide grain and organic residue (Fig. 5a,b) and the interior of a Cu-rich organic residue (Fig. 5c,d) were selected for extraction of FIB sections with a FEI Helios 600 NanoLab FIB (March, July 2017). The sections were subsequently lifted using a platinum gas-glue, thinned to electron transparency by ion gas milling (Ga^+ ions) and mounted on a molybdenum holder. Transmission electron microscopy was conducted with a JEOL 2100 transmission electron microscope (a field thermionic emission analytical electron microscope) at the Virginia Tech National Center for Earth and Environmental Nanotechnology Infrastructure (NanoEarth) (April, August 2017). Measurements were taken with an accelerating voltage of 200 kV and a beam

current of approximately 107 mA. EDS point analyses and maps were acquired in STEM mode with JEOL bright field (BF) and JED-2300T EDS detectors. Selected area electron diffraction (SAED) patterns were acquired using a Gatan Orius SC200D detector. Nanoparticles and larger crystals were identified using a combination of SAED, fast Fourier transformations (FFT) of lattice fringes, and EDS-STEM chemical distribution maps.

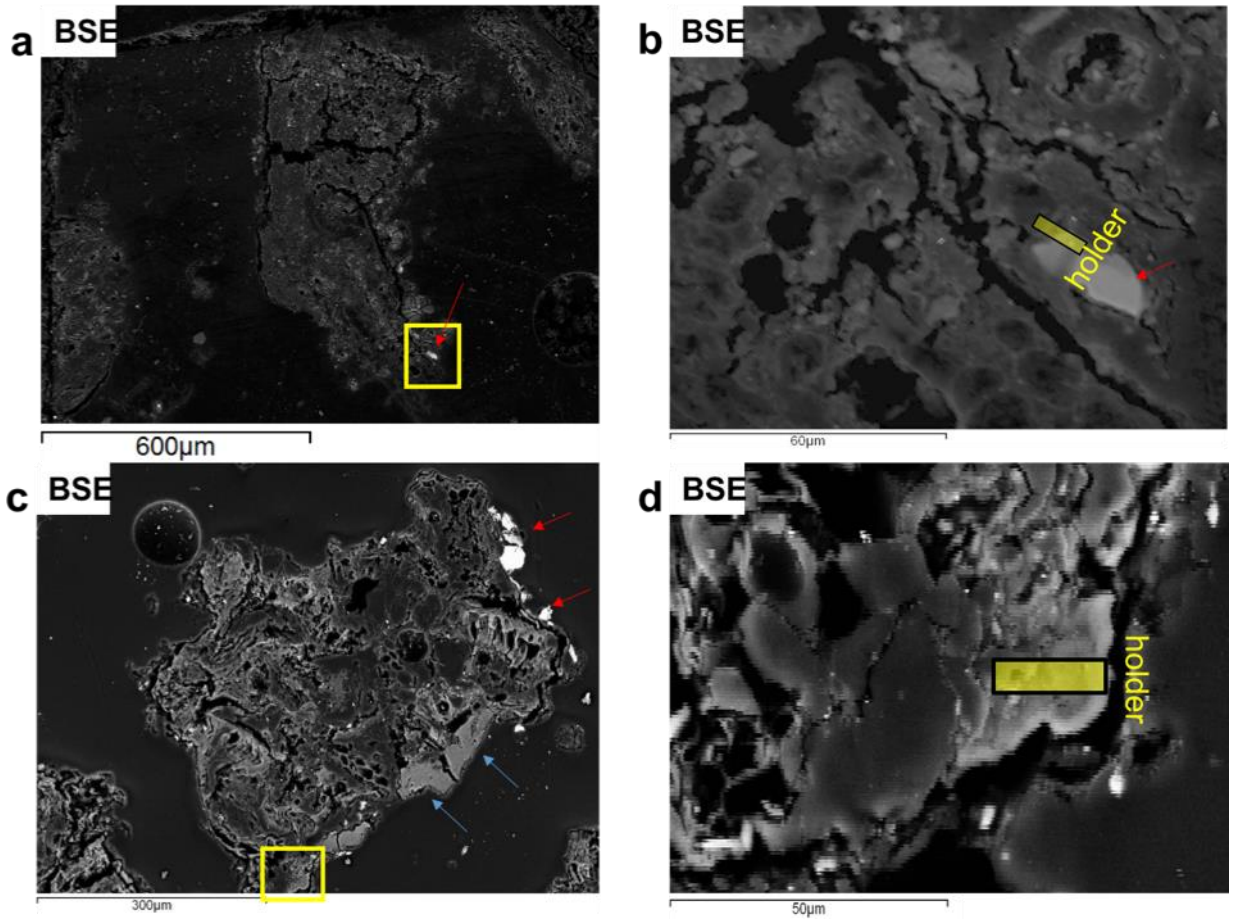

Figure 5. SEM back-scattered electron images (BSE) of organic residues from site 1 within a 0-5 cm coarse fraction chosen for nanoscale analysis. (a,b) extraction site of FIB section 1 (c,d) extraction site of FIB section 2; open rectangles in (a) and (c) indicate the the location of the areas shown in (b) and (d); filled rectangles in (c) and (d) indicate the exact locations of the FIB sections; red and blue arrows indicate the occurrences of sulfide silicate grains, respectively.

2.2.7 Colloid preparation and transmission electron microscopy

Soil leachates were collected during a column leaching experiment. Hollow, plastic tubes were filled with approximately 0.8 g of the dried and sieved (< 1.4 mm) 1 cm fraction with a small layer of inert and plastic beads on the top and bottom of the soil sample. A 0.01 μM $CaCl_2$ solution was passed through the column at an approximate rate of 3 mL/hr until 30 mL was collected in a tube below the column. A fraction of the leachate was centrifuged using a Beckman Coulter JA-17 centrifuge rotor 8000 rpm at 480 minutes which, according to the Stokes equation, will remove all spherical particles (density=8.96 g/cm^3) greater than 12 nm from solution. A second fraction (neat) was filtered using a 0.45 μm membrane. Neat and centrifuged leachates were acidified prior to analysis by ICP-MS to determine the total and dissolved metal concentration. Samples were acidified to 1 % HNO_3 and analyzed on a ELAN DRC II (Perkin Elmer) instrument at the Geo Labs. Concentrations of the metal(loid)s in the colloidal fraction (> 12 nm) were calculated by subtracting their concentrations in the solutions after centrifugation from the total metal(loid) concentration (which has not been centrifuged).

To prepare the colloids for TEM analysis, soil leachates were centrifuged using a Sorvall ST16 centrifuge equip with a TX-400 swing-bucket rotor. A molybdenum TEM grid (400 mesh lacey carbon, 100 μm) was fixed to an epoxy support at the bottom of the centrifuge tube and the tube was then filled with 2 mL of the leachate. According to the Stokes equation, spherical particles greater than 16 nm (density=8.96 g/cm^3) deposit onto the grid with a speed of 5000 rpm for 8 hours. The colloidal fraction on the TEM grid was examined with a field emission TEM FEI Talos F200x at the Manitoba Institute of Materials. Imaging and SAED was performed with an accelerating voltage of 200 kV in bright and dark field mode with a 16 MB ceta camera and a

Fischicone high angle annular dark field (HAADF) detector. Compositional analysis was performed in STEM-EDS mode with 4 SDD detectors.

2.3 Results

2.3.1 Bulk soil chemistry

The brownish black humic gley soils are oxic, slightly acidic and organic-rich soils with a pH/Eh of 5.0/726 mV at the time of sampling (Table 1). At site 1 the concentrations of Cu, Pb, and, Zn exponentially decrease with depth from 9220 ppm (Cu), 447 ppm (Pb), and 3280 ppm (Zn) at depth 0-1 cm to 265 ppm, 38ppm, and 964 ppm at depth 9-10 cm, respectively (Table S1, Fig. S4). The concentrations of these metals also decrease with distance from the contaminant source; the concentrations of Cu, Pb, and Zn in the surface layers at the two control sites (sites 2 and 3) are approximately 100 ppm (Table 1). These significant drops in metal concentration with depth and distance (Table 1 and S1) are typical for soils contaminated by atmospheric depositions from a point source, that being the former Kidd Creek smelter complex.[2,86]

Table 1. Selected trace metal concentrations and physiochemical parameters of the 0-5 cm fraction of site 1. Trace metal concentrations are given for two control sites (site 2 and 3) for reference.

Site	Trace Metal Concentration (ppm)[a]				Physiochemical Parameters				Distance to former smelter complex (km)
	Cu	Zn	Pb	Fe	pH	Eh (mV)	Total C (wt %)	Total S (wt %)	
1	13000	8210	685	2.07 %	5.0	726	> 110	0.411	1.3 SE
2	117	123	31	4135	4.8	626	-	-	2.5 ENE
3	92	163	15	5720	5.1	613	-	-	7.5 NE

[a] Concentration reported in ppm except where noted.

2.3.1.1 Mineralogical composition

The fine to coarse sand size fraction (> 180 µm) of the surficial soil layer at site 1 (0-5 cm) is composed predominantly of OM with minor amounts of quartz (SiO_2) and traces of digenite (Cu_9S_5), talnakhite ($Cu_9(Fe,Ni)_8S_{16}$), and magnetite (Fe_3O_4, Fig. S5). The finer clay to sand size fraction (< 180 µm) contains mainly quartz, hematite (Fe_2O_3), and albite ($NaAlSi_3O_8$) (Fig. S6). Scanning electron microscope analyses indicate that many organic residues in the coarse fraction contain dispersed Cu- and Si-bearing particles on their surfaces and within their pore system (Fig. S7). Electron microprobe analyses (n = 63) indicate that the majority of grains attached to organic residues are composed of Fe- and Cu-Fe-sulfides with minor amounts of Fe-oxides (Fig. S8). The fine fraction lacks organic residues containing Cu-bearing phases but contains a higher proportion of silicified organic grains, spherical smelter-derived particulates and angular silicate-based particles (Fig. S9).

2.3.2 Chemical and mineralogical composition at the interface

The first FIB section was extracted along the interface of a Cu-Fe-sulfide (mooihoekite, $Cu_9Fe_9S_{16}$) grain attached to a highly porous organic residue (Fig. 5a, Fig. S10). The organic material around the sulfide grain contains elevated concentrations of Cu in the range of 0.5-2.0 wt %, which can be recognized as brighter areas in backscattering electron images (BSE, Fig. 5b). The FIB section itself has been severely damaged but contains an intact sulfide grain and residuals of the organic material (Fig. 6)

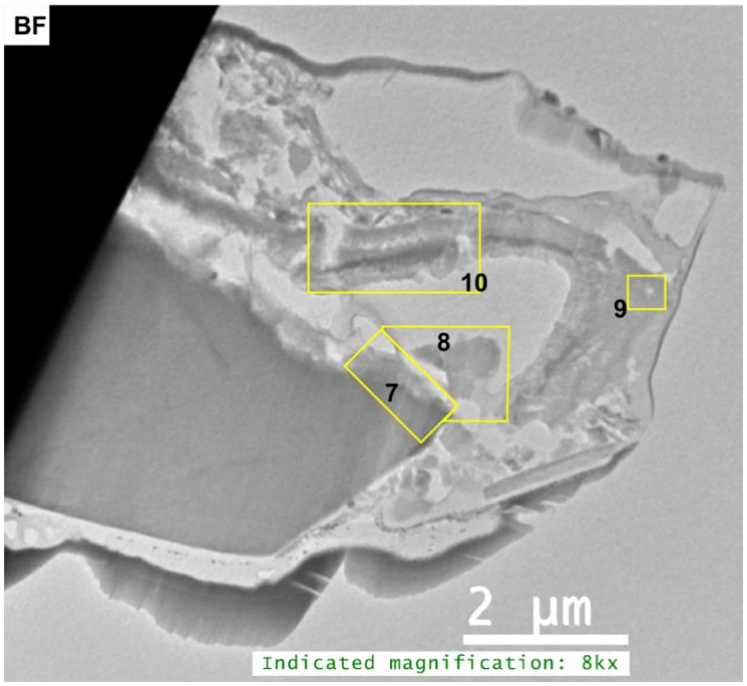

Figure 6. Bright field (BF) STEM image of the entire FIB section 1. Numbered rectangles indicate the locations of the TEM images shown in the Figures 7-10.

Chemical analyses, STEM imaging, and electron diffraction patterns indicate the presence of a porous magnetite/maghemite (Fe_3O_4 / Fe_2O_3) layer that formed along the exterior of mooihoekite and occurs along the interface of the organic material (Fig. 7, S11). Magnetite and maghemite are isostructural and therefore cannot be distinguished with electron diffraction. The diameter of the magnetite/maghemite layer varies between 30 and 160 nm. Elongated pore spaces occur throughout the layer with diameters in the range of 3-9 nm and with orientations parallel and perpendicular to the interface (Fig. 7b). Fragments of magnetite/maghemite also occur within OM in close proximity to the interface (Fig. 8b, S12). A Cu-rich area containing minor S and Fe occurs on the edge of the sulfide grain where no magnetite/maghemite surface layer occurs. Fast Fourier transformation patterns of lattice fringes and SAED patterns indicate the presence of the prominent d-spacings of 2.45 and 2.01 Å, however more than 10 other d-spacings occur in the FFT and SAED patterns suggesting the presence of an unknown structural derivative of a Cu-rich sulfide (Fig.

S13). Adjacent to the Cu-rich area occur fragments of boehmite (γ-AlO(OH)) and diaspore (α-AlO(OH)) which are embedded in the organic material (Fig. S14). Copper-bearing nanoparticles < 2 nm occur within the organic material along the interface of the Cu-rich area and the aluminum hydroxide fragments (Fig. S15). Fast Fourier transformations of lattice fringes of these nanoparticles indicate interplanar spacings of 2.10, 1.80, and 1.25 Å, matching the prominent (111), (200), and (220) d-spacings of metallic copper. However, various other d-spacings also occur suggesting that some of the NPs might be composed of a Cu-oxide or -sulfide.

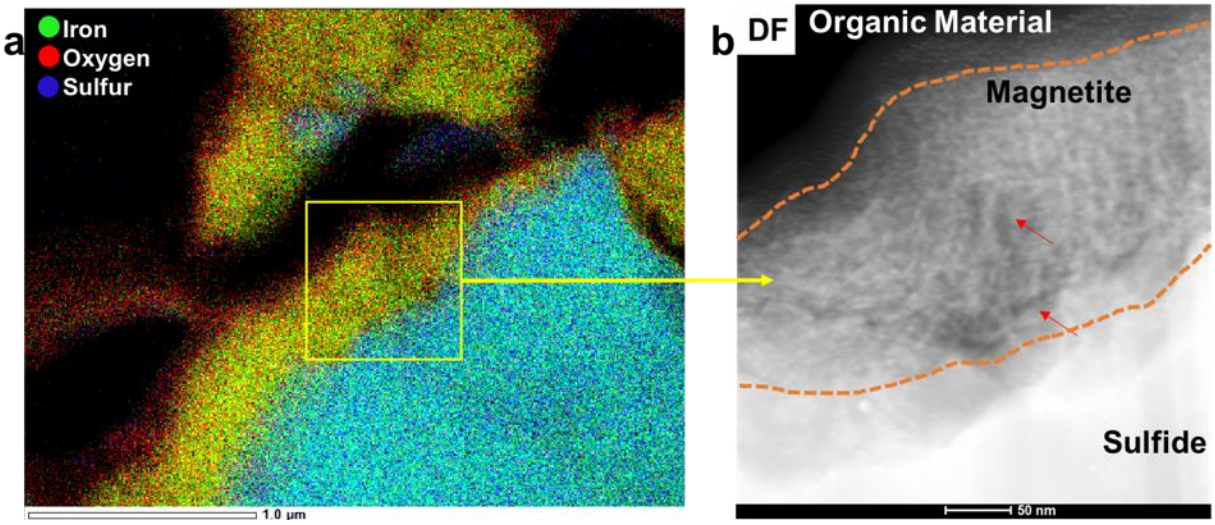

Figure 7. (a) STEM-EDS chemical distribution map for Fe, O and S along the interface between the sulfide grain (blue) and organic material (red), indicating the occurrence of an iron oxide layer in between (yellow); (b) dark field (DF) STEM image of the Fe oxide layer displaying its high porosity; red arrows indicate pore spaces in different orientations and orange dashed lines indicate interfaces between mooihoekite and magnetite/maghemite and magnetite/maghemite and organic material.

2.3.3 Chemical and mineralogical composition of phases within organic material

The FIB section extracted along the interface exhibits numerous porous, carbon-based features which are often associated with magnetite/maghemite. Copper occurs as NPs within both organic material and magnetite/maghemite (Fig. 8a-d). These NPs are a mixture of covellite (CuS), a $Cu^{2+/1+}$ bearing phase, and metallic Cu NPs.

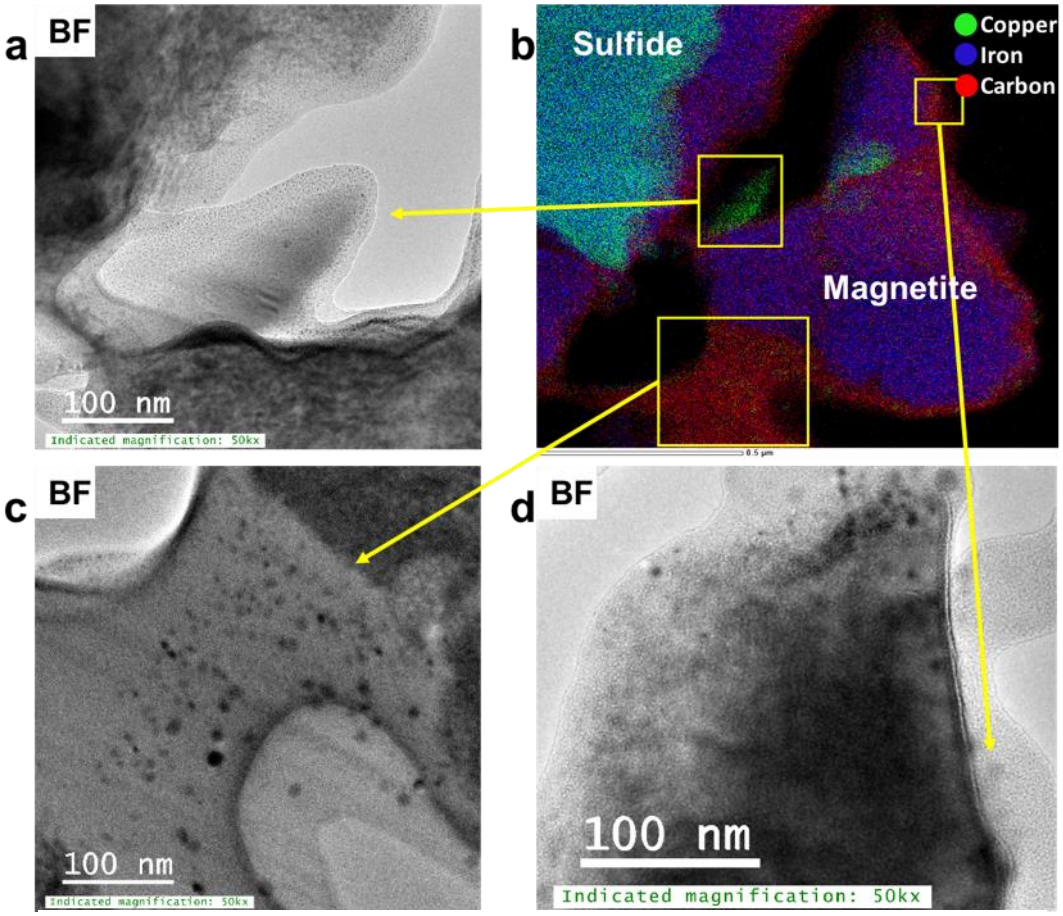

Figure 8. (a, c-d) BF TEM images of copper-bearing magnetite/maghemite fragments near the interface towards the sulfide, (b) STEM-EDS chemical distribution maps of Cu (green), Fe (blue) and C (red).

Covellite (yellow) and metallic Cu (green) are also closely associated in pore spaces of the OM further from the interface and as such, not in association with magnetite/maghemite (Fig. 6, 9). Metallic Cu appears to be attached to spherical NPs of covellite (Fig. 9). Metallic Cu also occurs in close association with bornite ($Cu^{+1}{}_5Fe^{+3}S_4$) and cuprospinel ($Cu^{+2}Fe^{+2}Fe^{+3}O_4$) in the organic material/magnetite matrices (Fig. S16).

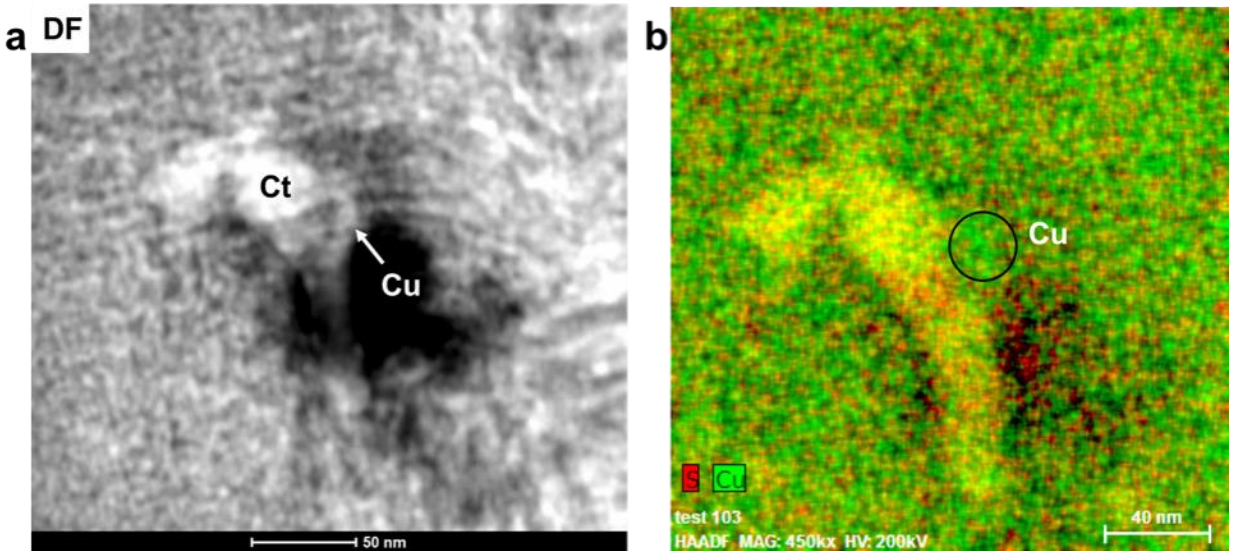

Figure 9. (a) DF STEM image of an inclusion of covellite and metallic copper within a pore space in organic material approximately 2 μm from the sulfide grain (b) corresponding STEM-EDS chemical distribution map of Cu (green) and S (red); the covellite and metallic Cu inclusions are coloured in yellow and green and are labelled as Ct and Cu, respectively.

Approximately 1 μm from the Cu-Fe-sulfide-OM interface, a layer of magnetite/maghemite is embedded within the OM (Fig. 10a, S17). On both sides of the iron oxide layer, Cu-bearing NPs occur predominantly in the surrounding OM, and also in a few cases on the surface of the magnetite. Selected area electron diffraction patterns indicate the presence of both tenorite (CuO) and metallic Cu NPs (Fig. S18).

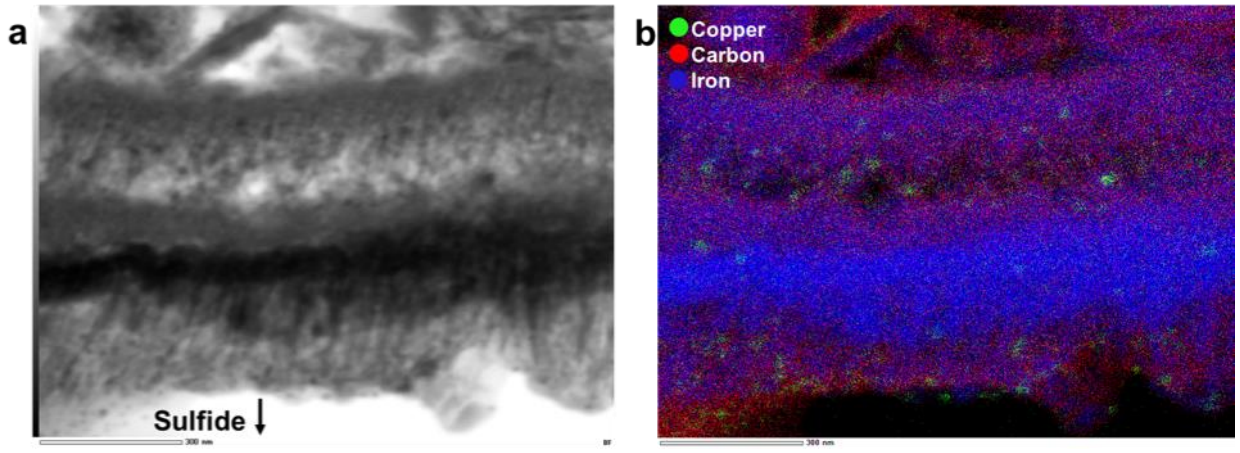

Figure 10. (a) BF TEM image of a magnetite/maghemite layer within organic material (b) corresponding STEM-EDS chemical distribution map of Fe (blue), Cu (green) and C (red); magnetite/maghemite, porous organic material and metallic Cu NPs are indicated in blue, red and green, respectively; an arrow indicates the direction where the main sulfide is located.

2.3.4 Copper NPs within the interior of organic material

A second FIB section was extracted from the interior of an organic residue (Fig. 5d) as the organic matrix in the first FIB section was severely damaged during the extraction. Numerous Cu-sulfide and silicate grains are attached to the organic residue (Fig. 5c). The area around the FIB extraction contains higher Cu concentrations than its surroundings. The organic matrix of the extracted FIB is more homogeneous in terms of mineralogical and chemical features, as well as texture relative to the matrix in FIB section 1 (Fig. 11a). The average Cu-concentrations in the section is 2 wt % (on the basis of STEM-EDS). Scanning-TEM images, SAED patterns, and STEM-EDS chemical distribution maps for Cu (green) and C (red) indicate the occurrence of metallic Cu NPs (Fig. 11b-d, S19). These NPs are relatively uniform in size (6-20 nm) and have an average diameter of 9 ± 3 nm (n= 330). These size ranges do not include aggregates of NPs, which can be composed of up to five spherical NP's (Fig. 11e).

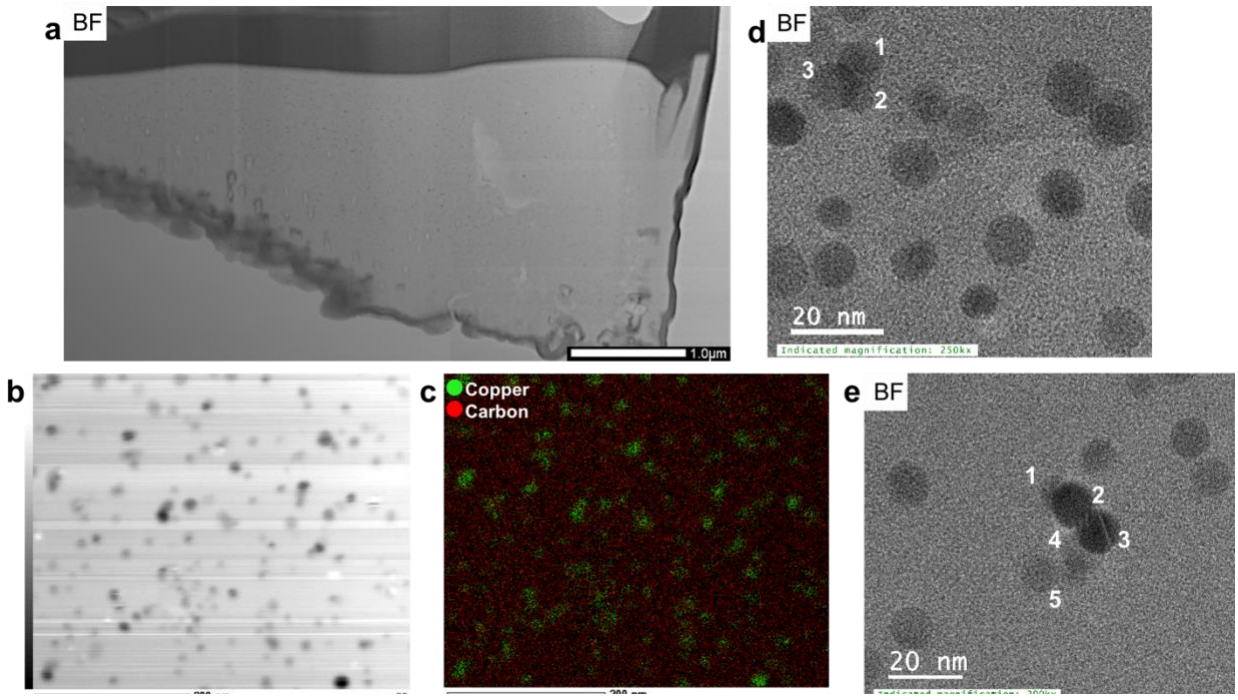

Figure 11. (a) BF STEM overview of FIB section 2 extracted from the interior of an organic residue; (b-c) BF-TEM and corresponding STEM-EDS chemical distribution maps for Cu (green) and C (red) indicating the occurrence of metallic Cu NPs (green) within organic material (red); (d-e) BF high resolution TEM images of individual and agglomerated metallic Cu nanoparticles.

2.3.5 Chemical and mineralogical composition of the colloidal material

The total concentration of Cu in the soil leachate from site 1 (0-1 cm depth) is 6630 ppb. The proportions of the dissolved and colloidal fraction of Cu in the leachate are 88.6 % (5872 ppb) and 11.4 % (758 ppb), respectively. TEM analysis of the colloidal fraction indicates that the bulk of the colloidal material is composed of carbon-based material with particle sizes often greater than 200 nm. Copper-bearing NPs are in close association with these larger colloids and occur either within or are attached to their surface (Fig. 12a,b). Colloids composed exclusively of inorganic based NPs include unidentified titanium oxide nanoparticles with surface precipitates containing Cu and S (Fig. 12c,d, S20).

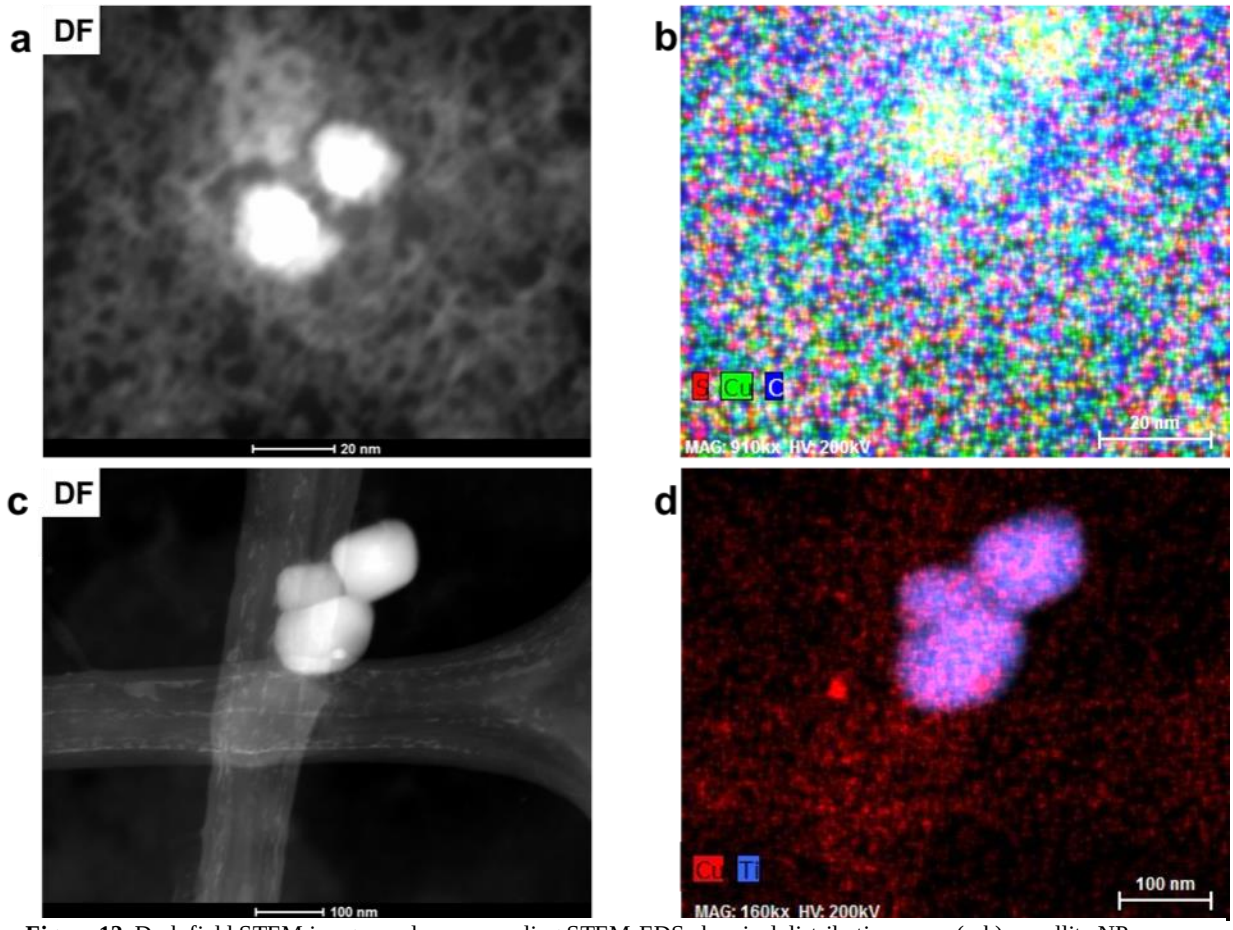

Figure 12. Dark field STEM images and corresponding STEM-EDS chemical distribution maps (a-b) covellite NPs embedded in carbon-based material with Cu in green, S in red and C in blue (c-d) Cu-S-bearing surface precipitates on rounded titanium oxide crystals with Cu in red and Ti in blue.

Scanning-TEM-EDS chemical distribution maps and fast Fourier transformations of lattice fringes indicate that the majority of Cu-bearing NPs in carbon-based colloids (Fig. 13a,b) are composed of covellite with two NPs identified as anilite (Cu_7S_4) and chalcocite (Cu_2S) (Fig. S21). Nanoparticles of covellite are mainly spherical and have diameters in the range of 15-35 nm. They are often composed of smaller nanoparticles which depict lattice fringes with d spacings of 3.08 (102), 2.73 (006), 1.88 (110), and 1.66 (200) Å. In some cases, the NPs are agglomerated in a random fashion with lattice fringes in different orientations whereas in others, fringes depict the same orientation (100, 200), with the exception of newly attaching NPs (Fig. 13c,d). In addition to lattice fringes with different orientations, attachment of NPs with diameters of approximately 1-4 nm to larger particles cause a distortion of their spherical shapes (Fig. 13e). Spherical nanoparticles identified as anilite and chalcocite occur in close proximity (< 5 nm) to each other (Fig. 13f) and have diameters of approximately 26 and 16 nm, respectively.

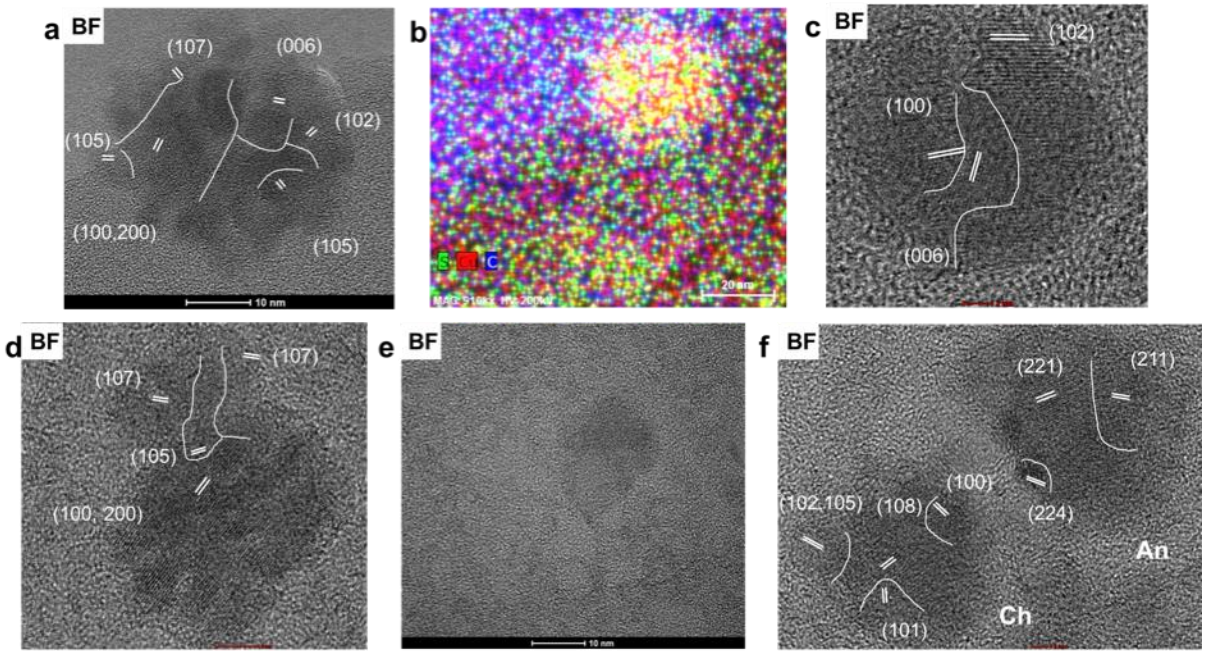

Figure 13. Cu-bearing nanoparticles in organic colloids within the leachate of the 0-1 cm fraction of the soils at site 1 (a-b) BF High resolution TEM image and corresponding STEM-EDS chemical distribution maps with Cu in red, S in green and C in blue of a covellite nanoparticles (in yellow) attached to organic material (blue), (c)-(d) BF high resolution TEM images of covellite nanoparticles with nano-domains of different orientation, (e) TEM image depicting the distortion of the spherical shape of a covellite nanoparticle most likely due to the attachment of new nanoparticles; (f) high resolution TEM image of an anilite (An) nanoparticle in close proximity to a chalcocite (Ch) nanoparticle with nano-domains of different orientations. In (a), (c), (d) and (f) white parallel lines indicate lattice fringes and white lines indicate boundaries between nanoparticles or nano-domains of different orientations; the fringes are labelled with their corresponding (hkl) notations.

2.4 Discussion

Examinations of a soil sample at the nanoscale using a combination of FIB and TEM allows for a site-specific, in-depth chemical and mineralogical analysis of an area of interest. For example, the Cu-Fe-sulfide in FIB section 1 (Fig. 5a) was initially identified as chalcopyrite and assumed to attach directly onto the OM (using SEM). However, the nanoscale investigations in this study indicate the occurrence of the sulfide mooihoekite (with a similar composition relative to chalcopyrite) and the attachment of the mooihoekite grain to OM by a magnetite/maghemite surface layer. The TEM studies show sequestration of Cu by OM occur through metallic Cu and covellite formation, though both phases were not identified using SEM and EMPA.

However, care must be taken to not overstate the significance of findings discovered at the nanoscale. For example, a FIB section is typically only 5 x 20 μm, and the high costs and skills required to prepare FIB sections and operate the TEM limit the preparation of many subsamples at the nanoscale. Furthermore, the soil sample collected for this TEM study originates from only one location in close proximity to the former Kidd Creek smelter. This area was chosen to ensure the presence of anthropogenic Cu-bearing phases. Therefore, it is not realistic to claim that the results presented in this study are representative for the speciation and mobilization of Cu in all organic-rich soils in the Timmins area. For example, the speciation of Cu may differ at sites which are (a) located farther from the former smelter (lower Cu concentrations) or (b) characterized by different environmental conditions (i.e. wetlands or non-forested areas). However, this study provides for the first-time insights into complex nanoscale dissolution-precipitation-reduction processes along the interfaces of PM, Cu-bearing pore solutions, and OM; processes that cannot be visualized using bulk analytical methods such as sequential extraction or synchrotron-based spectroscopy.

2.4.1 Origin of the particulate matter observed in the surficial soil layer of site 1

Atmospheric deposition of PM derived from mining-related activities onto surficial soils can be detrimental to the environment. In this study, Cu-bearing PM is found to be associated with organic residues in the 0-5 cm coarse fraction of soils sampled near the former Kidd Creek smelter complex (Site 1). The observed particulates have angular shapes, are heterogeneous in terms of their mineralogical and chemical composition, and lack cooling or crystallization features such as rims or idiomorphic crystals in a glass matrix.[87] Furthermore, the Cu- and Fe-bearing particulates have a similar chemical composition as the processed ore, with the major ore minerals being

chalcopyrite and pyrrhotite. Hence, the particulates observed on the surfaces of organic residues were most likely wind-blown from waste piles to site 1. Contrary, smelter-derived PM commonly have a spherical shape and display high-temperature features such as dendritic, skeletal, tabular, and porphyritic patterns.[11] The latter particulates occur predominantly in the fine fraction (< 180 μm) but have not been identified on the surface or within organic residues in the coarse fraction (Fig. S6).

2.4.2 Attachment of sulfide grains to organic material

The majority of the grains present in the < 1.4 mm soil fraction are composed of partially decomposed organic material with attached Cu-Fe-sulfides. The latter phases predominantly occur as clay to silt-size grains (< 75 μm) and therefore are expected to occur in the fine fraction after sieving and in the colloidal fraction after extraction. The predominant occurrence of these particles in the coarse sand-size fraction and their absence in the colloidal fraction suggests that (a) attachment is based on electrostatic forces rather than being a result of forced compression and (b) nanometer-size airborne Cu-Fe-sulfides are not stable in the oxic pore water at site 1.

The attachment of sulfide grains to the organic residue via electrostatic forces can be understood when considering the point of zero charge (pzc) of these compounds. The typical pzc value of most organic based compounds in soil is 2 to 3.[27,34] If the surfaces of the organic grains are not modified through mineralization processes, their surface should be negatively charged in the pH environment of the Timmins soils (pH = 5.0). Copper-Fe-sulfides such as chalcopyrite have a pzc value of approximately 2.[88] Hence, the surface of these sulfide grains would be negatively charged and therefore these grains do not electrostatically attach to organic material due to repulsive forces.

The attachment of sulfides to organic material requires a positively charged surface on the sulfide grain. In this study, a nanometer thick surface layer of magnetite/maghemite was identified. This layer most likely had a positive surface charge at the time of attachment as the observed soil pH conditions at site 1 is pH = 5.0 and the pzc of magnetite, maghemite, or a Fe-(hydr)oxide precursor of magnetite is above 6.5.[89] That being said, surfaces of minerals with pzc > 6.5 can be also negatively charged in weak acidic, organic-rich soils due to the presence of adsorbed organic molecules.[90] In such a case, the negatively-charged surface would promote the mobility of a mineral grain or NP in an organic-rich soil column.

2.4.2.1 Formation and properties of the alteration layer

Sulfides are known to readily oxidize in the environment. The oxidation of sulfides exposed by mining activities can be accomplished through atmospheric oxidation prior to soil deposition or by electrochemical oxidation (pH/Eh dependent) after deposition. A combination of the two processes likely contributed to the formation of the magnetite/maghemite surface layer, as suggested by the lower solubility of chalcopyrite relative to other sulfides.[91,92] Studies on oxidation mechanisms of chalcopyrite indicate the formation of Fe-(hydr)oxide surface layers on its surface, though the Fe-(hydr)oxide minerals in these studies are not unequivocally identified.[91,93] The first generation of alteration products on the surface of Fe-sulfide minerals is commonly composed of schwertmannite (under acidic conditions) and ferrihydrite (under weak acidic to alkaline pH conditions).[94] The formation of these nanocrystalline phases follows Ostwald's Rule that a solid phase with the lowest interfacial free energy forms first although it may not be the most stable by bulk thermodynamics. The second generation of Fe-sulfate or hydroxide phases include jarosite at

pH < 4 and goethite, magnetite, maghemite, and hematite at pH > 5.[94] These phases form through the re-arrangement of the iron oxide polyhedra or through dissolution re-precipitation processes.[95]

The observed alteration layer on the surface of the sulfide is composed of magnetite and/ or maghemite (Fig. 7, S11). Magnetite can form from ferrihydrite through a dissolution re-precipitation processes under reducing conditions in alkaline soils or in flooded soils with high Fe (II) concentrations.[94,95] Since oxidation is required for the formation of a Fe-(hydr)oxide alteration layer on a sulfide surface (i.e. oxidation of S^{2-} to SO_4^{2-}), the magnetite surface layer could not have formed in contact with the observed oxic pore water. Hence, the formation of magnetite most likely occurred after attachment to the organic residue as an interface between an organic compound and a sulfide grain should have a lower reduction potential than a surface exposed to oxic pore water. This conclusion is also supported by the observation that a layer of magnetite/maghemite occurs within the OM (Fig. 10). Maghemite commonly forms through oxidation of magnetite, though it can also form from a ferrihydrite precursor under high temperature (> 150 °C) or through the transformation sequence ferrihydrite-goethite-maghemite under alkaline conditions.[96,97] However, the latter two conditions can be ruled out for the surficial weakly acidic soils at site 1.

Hence, we propose the following sequences for the formation/transformation processes on the surface of the sulfide: (1) sulfide oxidation followed by the precipitation of ferrihydrite, (2) transformation of ferrihydrite to magnetite under reducing conditions, and (3) perhaps partial transformation of magnetite to maghemite through the oxidation of Fe^{2+}.

During a mineral replacement reaction, coupling between the dissolution of a parent (sulfide) and precipitation of a daughter (precursor to magnetite) can be achieved when the controlling mechanism is the dissolution rate of the parent and when the activation energy barrier for the nucleation of the daughter is low.[98] This is most likely the case during the alteration of the

sulfide, as ferrihydrite is commonly the precursor of magnetite. Putnis[98] emphasizes that (a) porosity in the product phase is commonly generated when there is a volume deficit reaction and (b) the porosity of the replacing phase allows the mass transfer of material from the solution reservoir to the reaction interface. The observed porosity in the alteration rim (Fig. 7b) suggests that the replacing phases of the first and second generation (ferrihydrite and magnetite) have smaller molar volumes than the phases to be replaced (sulfide and ferrihydrite). This is indeed the case: the molar volumes decrease from mooihoekite (V_m = 363 cm^3/mol) to ferrihydrite (V_m = 167 cm^3/mol) to magnetite (V_m = 44 cm^3/mol). Additionally, molar ratios of parent to daughter minerals confirm this volume deficit (Table S2).

The solution entering the ferrihydrite alteration rim before and after attachment was likely different in terms of composition and reduction potential. The solution entering the ferrihydrite prior to attachment was most likely acidic and oxic (Table 1). The pore solution after attachment would initially pass through the pore spaces of the organic residue and would thus have contained less dissolved O_2 and some dissolved organic matter (DOM). The influx of electron donors (DOM) could induce the reduction of Fe^{3+} to Fe^{2+}, promoting the transformation of ferrihydrite into magnetite.

2.4.3 Metallic copper in the environment

Metallic Cu rarely occurs under natural environmental conditions. Ilton and Veblen[99,100] demonstrate the presence of metallic Cu NPs within the interlayer structure of biotite samples within oxidized rock from various copper porphyry deposits. The authors note that metallic Cu does not occur in Cu-rich chlorites from the same samples and the only reductant present within the biotite samples was Fe^{2+}. This observation suggests that the metallic Cu NPs formed via

reductive alteration processes and not from magmatic hydrothermal events. Ilton *et al.*[101] subsequently provided experimental evidence for the formation of metallic Cu NPs within the interlayer structure of Fe^{2+}-bearing micas through their interaction with $CuSO_4$ solution. Similarly, Ahn *et al.*[102] show that metallic Cu NPs can form in the interlayer structure of Fe-bearing illite.

The formation of metallic Cu in the presence of OM has been observed in bogs, wetlands, and floodplains. For example, metallic Cu can form as sub-micron particles and centimeter-sized masses in permanently flooded parts of a bog under anaerobic conditions.[103,104] Metallic Cu NPs have been identified in laboratory experiments using contaminated floodplain soils and along and within roots of two common wetland plant species. In these experiments, the formation of metallic Cu NPs is found to be promoted through a combination of limited sulfur availability, copper-stressed bacteria (Gram-positive *Clostridium* sp), Fe^{2+} in clays, or by endomycorrhizal fungi under anoxic conditions.[49-54] Upon soil drainage (i.e. exposure to higher fO_2) or the addition of biogenic sulfide, metallic Cu is commonly converted to Cu-bearing aqueous species or Cu-sulfide phases such as Cu_xS phases.[105]

In this study, we propose that the metallic Cu NPs identified in OM are products of the mobilization of Cu in the form of $Cu^{1+/2+}$ aqueous species released during the alteration of the Cu-Fe-sulfide grains. The reduction of the Cu species is induced by Fe^{2+} or by redox-active functional groups present on the surface of humic substances (Fig. 14). In the following sections, possible mechanisms for the mobilization and formation of Cu aqueous species and NP are discussed.

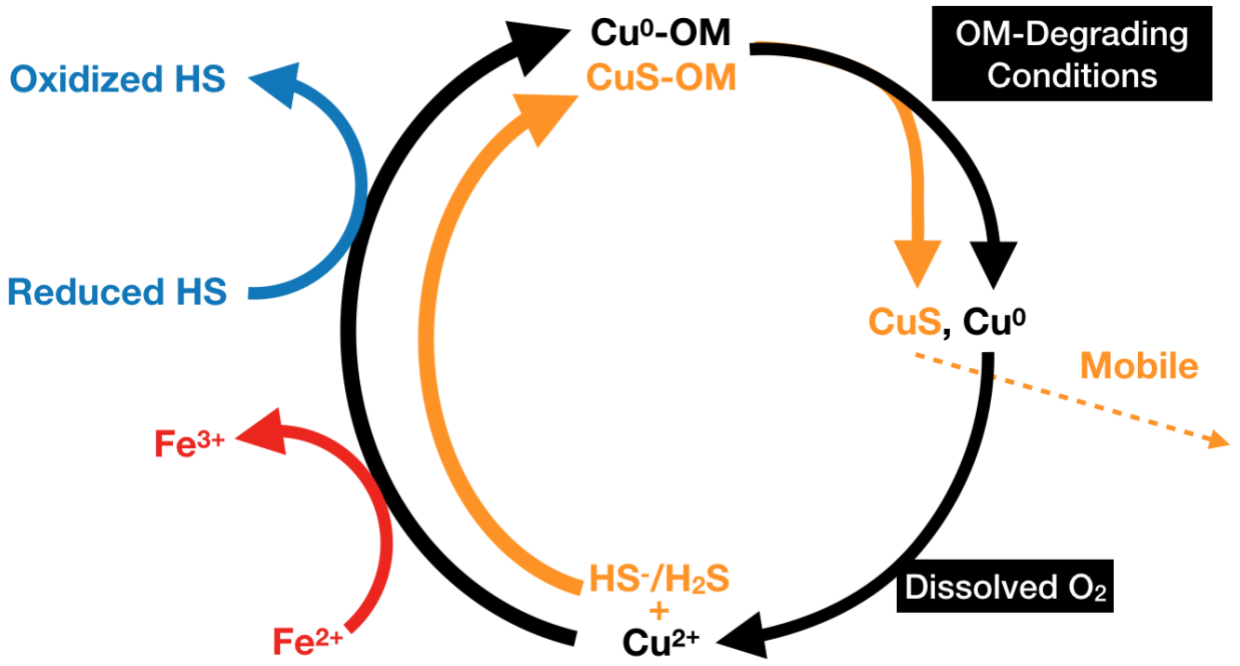

Figure 14. Schematics of the proposed recycling of Cu (black) in organic-rich soils; Cu^{2+} species become reduced by either ferrous iron (red) or reduced humic substances (blue) to metallic copper, which forms nanoparticles in organic residue. Upon degradation of the organic residue, nanoparticles are released. Metallic copper can be re-oxidized by the oxic pore water to form Cu^{2+}, allowing its diffusion into the organic material. The cycle for sulfur (orange) includes the formation of covellite NPs by the reaction of Cu^{2+} and dissolved hydrogen sulfide or bisulfide within organic matter. The particles are released during degradation of the residue and their dissolution results in the formation of Cu^{2+} which can then re-enter an organic residue.

2.4.3.1 Diffusion of Cu into organic material

The replacement of the Cu-Fe-sulfide by Fe-(hydr)oxides after attachment of the sulfide grain may involv an influx of hydrogen and DOM-species and an outflux of H_2S and Cu-bearing species. As such, the continuous mineral replacement reaction may be seen as the driving force for the diffusion of Cu through the porous Fe-(hydr)oxide layer into the porous OM. The transport of Cu through both porous entities might be facilitated by DOM as humic and fulvic acids are known to complex Cu.[106] The results above show that metallic Cu is incorporated or attached to both OM and magnetite/maghemite within the organic residue (Figs. 8-10). This requires porosity along the surface of the organic residue, a diffusion gradient between the interface and interior of the organic residue, and that inner-sphere adsorption complexes between Cu^{1+}-bearing species and negatively-charged functional groups on the surface of the residue did not limit the diffusion of Cu into the

interior of the residue. The latter requirement may have been achieved through neutralization of the negatively-charged surface sites through the formation of inner-sphere Cu^{1+}-OM complexes.

An alternative mechanism of Cu transport may be the diffusion of negatively charged Cu-DOM species into the organic residue. In this case, immobilization of the Cu-DOM species within the OM and subsequent reduction of Cu^{1+} to Cu^{0} would require the removal or reduction of electrostatic forces to allow bridging between available DOM functional groups and the organic residue. A reduction of electrostatic forces can be achieved by an increase in ionic strength[56] which seems, however, an unlikely scenario for a diffusion pathway into the interior of an organic residue. Alternatively, the presence of positively-charged surface groups in the OM could facilitate the adsorption of the negatively-charged Cu-DOM species. Although the surface charge of OM is predominantly negative at a pH of 5, a small fraction of positively-charged amine and amide groups could facilitate the deposition of Cu-DOM complexes within the OM.

Diffusion of Cu into OM at the location of the second FIB section was likely not a result of the weathering of an attached Cu-bearing particulate as the closest attached Cu-Fe sulfides are approximately 500 μm from the location of the FIB section extraction (Fig. 5c). Hence, the Cu observed within this section likely originated from surrounding soil pore solutions. Diffusion into the OM requires porosity, a diffusion gradient, and the absence of attractive electrostatic forces between the Cu-bearing aqueous species (Cu^{1+}, Cu^{2+}, Cu-DOM) and the surface functional groups of the residue.

2.4.3.2 Reduction mechanisms for copper

The accumulation of metallic Cu NPs around and within the magnetite layer (Fig. 10) is best explained by the reduction of $Cu^{1+/2+}$ by Fe^{2+}. Ilton et al.[101] demonstrates that octahedrally

coordinated ferrous iron in micas can induce the reduction of Cu^{2+} to metallic Cu. Additionally, ferrous iron in magnetite and green rusts (Fe^{2+} bearing species) can induce the reduction of redox-sensitive metal ions into their respective elemental species.[107,108] As such, Cu ions adsorbed to magnetite embedded in the organic material were most likely reduced by Fe^{2+} on magnetite surfaces. The oxidation of Fe^{2+} would result in the subsequent transformation of magnetite into maghemite.

However, these conclusions seem to contradict the absence of metallic Cu NPs in the magnetite/maghemite layer along the interface to the sulfide. The absence of Cu NPs in the alteration product along the sulfide grain but presence within the interior of the OM may be due to differences in their mineralogical, chemical, and textural features. Possible reasons for the absence of metallic Cu within the alteration layer are as follows:

(1) A higher abundance of maghemite, Fe_2O_3, along surface sites (the presence of only Fe^{3+} may not have facilitated the reduction of Cu species).

(2) A higher porosity of the layer on the sulfide grain relative to the layer in the interior of the organic residue. A higher porosity and permeability may result in an efficient removal of metallic Cu NPs formed along adsorption sites as there is a constant flux to and away from the alteration layer.

(3) The higher positive surface-charge of the Fe-oxide layer on the sulfide coupled with the positive surface charge of Cu NPs would facilitate a higher mobilization of the Cu-NPs within this layer. The pzc of synthetic Cu NPs is shown to be 9.4,[109] and therefore metallic Cu NPs would be positively charged at pH = 5. The iron oxide layer on the sulfide grain likely has a greater positive surface charge relative to the layer within the OM as the former layer is likely exposed to pore-water of higher acidity than the latter one.

(4) A larger proportion of DOM in and around the layer within the OM. Maghemite surface sites that form through the reduction of Cu^{1+} to Cu^{0} in the interior of the organic residue may be transformed back to magnetite as the influx of DOM species would provide plenty of Fe^{3+} reducers.

However, as metallic Cu is identified within OM where no magnetite occurred, an additional reduction mechanism for $Cu^{1+/2+}$ must be considered. Native copper has been experimentally proven to form by the direct reduction of Cu ions by reduced functional groups on soil HS.[52] Research shows that HS can act as electron shuttles where redox-active functional groups gain electrons from soil microorganisms and subsequently donate those electrons to oxidized metal species. This process is effective for the reduction of various metals by soil or aquatic fulvic and humic acids.[28,49,52,110] A variety of functional groups have been identified in HS, however only those capable of accepting and transferring electrons may induce metal reduction. This redox activity of HS can be primarily attributed to the quinone-hydroquione and phenolic moieties.[50] Although soil HA cannot induce the reduction of Ag^{+} to metallic Ag NPs at room temperture[28] and aquatic FA can only reduce Cu^{2+} ions to the monovalent species[54], Fulda *et al.*[52] shows that soil HA are capable of reducing Cu^{2+} to metallic Cu NPs. As such, the vast amount of Cu NPs dispersed throughout the OM in the second FIB section (Fig. 11) suggests that the corresponding OM has experienced significant reduction prior to Cu ions diffusion, subsequently enabling functional groups such as quinone or phenolic groups to reduce $Cu^{1+/2+}$ into Cu^{0}.

2.4.3.3 The formation of covellite

The predominant Cu-bearing NPs identified in the colloidal fraction of the surficial 1 cm soil layer is covellite, however covellite NPs have rarely been reported to form in a soil environment. One can consider here two approaches that can lead to the formation of the covellite NPs: a top-down or bottom-up approach. The top-down approach would involve the formation of covellite NPs through the breakdown of larger (micrometer-size) grains of covellite. However, electron microprobe analysis of sulfide grains attached to OM do not indicate the presence of grains with Cu:S:Fe ratios of 50:50:0 (Fig. S9). This is not unexpected as the pzc value of pristine covellite or surface-oxidized covellite has been reported to be less than 4.[111] As no positively-charged Fe-(hydr)oxide layer can form through the alteration of covellite, the surface of the covellite grains is likely negative charged and would prevent electrostatic attachment to organic residues. Furthermore, no Cu-Fe-sulfide nanoparticles are observed within the leachate, which would be expected if the breakdown of larger grains contributes to the formation of mobile nanoparticles.

An alternative explanation for the occurrence of the covellite NPs can be explained with a bottom-up approach. Gramp *et al.*[112] show that in the presence of sulfate-reducing bacteria, a $CuSO_4$ solution reacts to form large precipitates of covellite. Weber *et al.*,[113] suggests that the formation of these precipitates in solution may be environmentally relevant for low concentrations of reactants within soil. Here the formation of covellite colloids (< 150 nm) occurs through the reaction of reduced Cu species with biogenic sulfide which forms through the reaction of sulfate and sulfate-reducing bacteria.[113] Under these experimental conditions, the formation of covellite NPs may be most relevant within redox-variable soils with sufficient sulfide gradients.[113] Upon heavy rain or snow, soils may become temporarily flooded, causing the reduction of Cu^{2+} into Cu^{1+} or Cu^0, at which point biogenic sulfur can react with the reduced Cu to form covellite NPs.

Although the mobile covellite nanoparticles observed in our study may have formed through the reactions indicated by Weber,[113] they may also originate from organic residues similar to those analyzed in FIB section 1. In this case, covellite most likely formed through the reaction between $Cu^{1+/2+}$ and H_2S released from the attached sulfide or from dissolved sulfur present in the pore spaces of the OM (Fig. 14). Upon degradation of a NP-containing organic residue, organic colloids containing covellite NPs may be released into the soil pore water. Though it is noted that H_2S is a stronger reducer than Fe^{2+}, it is still weak and it is unlikely to be strong enough to induce copper reduction prior to the formation of a kinetically favourable copper sulfide product.

The mobilization of covellite NPs within the 1 cm fraction at site 1 is clearly facilitated by organic material (Fig. 12a,b). The following observations strongly suggest that these covellite NPs formed within the organic material:

(1) The covellite NPs are always fully embedded in organic material. Although it is possible that minor concentrations of covellite could be stable in oxic pore water,[114] nanoscale analysis of the leachate have not indicated the presence of covellite particles in the absence of organic matter.

(2) The negative surface charges of covellite and the organic material at pH = 5 have not favored the attachment of colloid NPs to the surface of the large organic colloids.

2.4.3.4 Formation and agglomeration of nanoparticles

The formation of NPs requires a decrease in total free energy and the ability for many nuclei to develop which can occur by sudden changes in supersaturation, an increase in reaction sites, or Eh/pH conditions.[12,115,116] Hence, the formation of spherical metallic Cu and covellite NPs is most likely induced by a sudden change in the environmental conditions upon the adsorption and reduction of Cu species by OM or magnetite. Their formation in the organic residues is most likely

promoted by a high number of reductive sorption sites present on or within organic material or magnetite. Through an increase in porosity around surface rims and larger pores, these sorption sites become available for the adsorption of Cu or S species, the reduction of $Cu^{1+/2+}$-bearing species and the subsequent nucleation of metallic Cu or covellite NPs.

Upon the formation of metallic Cu or covellite, the NPs either attach or repel one another upon collision which is controlled by weak attractive van der Waals forces or attraction-repulsion forces such electrostatic interactions.[117] Nanoparticles naturally agglomerate in order to reduce the free energy and thus to increase their stability. However, a limit can be reached where the agglomeration of particles no longer increases stability, but rather decreases it. At this point, the process of agglomeration would require minimization of repulsion forces, and therefore the charged particles must be screened or exhibit a neutral surface charge. Crystalline NPs can attach to a surface of a growing aggregate or crystal either in a specific crystallographic orientation (*i.e.*, orientated attachment), or in a random orientation. The orientated attachment requires the rotation of NPs upon attachment and is controlled by Coulombic and Lewis acid/base interactions between the surface atoms of the NPs and aggregate.[118] Attachment of a single NP in a random orientation requires subsequent structural re-organization for their full integration into the aggregate or bulk crystal.[47]

As it has been observed in this study, the agglomeration of spherical metallic Cu NPs results in the formation of larger aggregates (< 30 nm) in non-spherical moieties (Fig. 11). Smaller covellite NPs agglomerate into larger (< 20 nm) particles within organic material (Fig. 13). The observed aggregations are likely related to charge screening by DOM or effective van der Walls forces. In the case of the growing aggregates of covellite NPs, attachment of the NPs occurs in an orientated (Fig. 13d) and non-orientated fashion (Fig. 13a)

2.4.4 Colloidal versus solute transport of copper

During their transport in the soil column, the negatively-charged covellite-bearing organic colloids may become immobilized through sorption to positively-charged Fe-(hydr)oxides surfaces. Alternatively, microbial activity could degrade their organic material[119] which would result in the release and oxidative-dissolution of the covellite NPs by the oxic pore water. In the latter case, $CuSO_4$ or $Cu^{1+/2+}$ could be recycled by sulfur-reducing bacteria (see above) or through their adsorption and diffusion into organic residues and their subsequent precipitation as covellite or metallic Cu within organic residues.

However, the covellite-bearing colloids likely have a small impact on the transport of Cu to greater depths as (a) the colloidal fraction of Cu represents only 11.4 % of the total Cu in the leachate, and (b) larger organic colloids (> 200 nm) commonly have a lower mobility than Cu-bearing aqueous species. The Cu-bearing aqueous species in the leachate have been adsorbed to surface sites of the OM and released by the electrolyte solution through the competitive effect between Ca^{2+} and $Cu^{1+/2+}$ species.

The observed exponential decrease (Fig. S4) in the Cu concentration with depth suggests that the strength of the Cu-OM adsorption complexes significantly limits the transport of Cu to greater depth. As such, the observed low mobility of Cu in the organic rich soils in Timmins and smelter-impacted areas elsewhere[17,18] is most likely a result of (a) the low solubility of most Cu-bearing PM,[9] (b) the attachment of Cu-bearing PM onto organic residues, (c) the sequestration of Cu within the organic residue, (d) the minor proportion of Cu-bearing NPs in the colloidal fraction, (e) the occurrence of Cu-bearing NPs embedded into larger less mobile organic colloids, and (f) complexation of Cu aqueous species by OM.

2.5 Conclusion

The majority of information gathered within this study revolves around the application of nanoscale techniques. Without these precise, in-depth analytical methods, data gathered from the microscale would have been generalized and therefore approximated. For instance, Cu detected throughout the organic grains with SEM likely would have been noted to occur as absorbed species. Additionally, the Cu-Fe-sulfides found to be attached to organic grains would have been mainly identified as chalcopyrite. From our work, we know that neither of those two situations are correct, highlighting the importance of nanoscale analyses.

The presence of metallic Cu NPs and covellite within surficial, oxic soils has not been observed until this study. Their occurrence indicates that even within a soil solution that has a high oxidative-reduction potential, Cu can remain in its reduced, native form or in association with S as Cu^{1+}. The apparent stability of reduced Cu-bearing NPs in the examined soil is of great importance for remediation strategies of Cu-contaminated soils using organic-rich substances. For example, Kumpmane *et al.*[120] show that the addition of coal fly ash and peat to contaminated soils decreases the amount of leachable metals by 98.2 and 99.9 % for Cu and Pb, respectfully. The authors indicate that this reduction of exchangeable metals is due in part to the formation of Cu- and Pb-bearing inorganic phases as well as an increase in metal sorption to additional surface sites provided by the fly ash and peat. While these explanations are likely true, the results of our study suggest that the observed Cu retention could also be attributed to the absorption of Cu by the porous organic materials and its subsequent reduction and sequestration to its native form.

On a broader scale, this study may help to fill in potential gaps in research centered on interactions between Cu and organic material. The majority of previous studies focused on the interaction between ionic Cu and its sorption to organics or the formation of stable inorganic

compounds, independent of the organic-rich environment it may reside in. Adsorption of metals is predominantly thought of as a transient mechanism of retention where ionic metal species are weakly retained until stronger inner-sphere complexes occur. This study shows that Cu can be adsorbed by organic material through the in-situ formation of inorganic Cu NPs which leads subsequently to its immobilization within the organic host. Hence, future research studies on the retention and sequestration of Cu in organic-rich environments should consider this additional mechanism when interpreting their results.

Chapter 3

3.1 Conclusion

In the present study, we characterized at the nanoscale selected areas in two Cu-rich organic residues from soils surrounding the Kidd Creek smelter in Timmins, Ontario. Using a combination of FIB technology, column experiments, centrifugation, and TEM analysis, we identified the occurrence of numerous phases at the interface between organic material and an anthropogenic sulfide grain, along a Cu-rich rim of an organic residue, and in dissolved organic matter. This study specifically revealed that Cu-Fe-sulfide grains were attached to organic material via porous iron oxide layers and this type of attachment effectively sequestered the grains in the upper soil layer. The Fe-oxide alteration layer was a product of an oxidation and dissolution/precipitation process. The highlights of this study were, however, the identification of the Cu-bearing phases, metallic Cu and covellite, within organic residues and DOM within the upper 5 cm of an organic-rich, oxic, and acidic soil horizon. Until this study, metallic Cu NPs have only been observed as nano-sized inclusions in Fe-bearing sheet silicates and organic material in bogs, wetlands, and floodplains under anoxic conditions. In the organic residues, metallic Cu NPs were identified on the surface of magnetite/maghemite inclusions and finely distributed within organic material. The existence of metallic Cu NPs in these environments was attributed to both the presence of reduced humic substances within OM and ferrous iron in the surface structure of magnetite. Nanoparticles of covellite were predominantly found in the colloidal, mobile fraction of the top soil layer (0-1cm) in which they occurred embedded in organic material. The identification of metallic Cu and covellite NPs were unexpected and suggested that confined pore spaces within organic material effectively sequestered and preserved phases which were otherwise not stable in the oxic and acidic surface layers of the soils.

The occurrence of these NPs may affect the perceived mobility of Cu within similar soils or influence potential reclamation tactics. The depth profile of the sampling site indicated an exponential decrease in the concentrations of the trace metals from the surficial soil layers to deeper layers, indicative of atmospheric deposition of particulate matter. This observation also indicated that the majority of metals in the surficial soil layer were relatively immobile. The column experiments showed that the proportions of Cu in the colloidal fraction (~10%) were much smaller than those in the dissolved fraction (90%) which suggested that the mobilization of covellite-bearing colloids would not contribute significantly to the overall mobility of Cu.

3.2 Future Work

The information gained in this study might influence the direction of future reclamation practices in the Kidd Creek area. Common techniques involve the application of a chelating agent coupled with DOM, however this method may not have an effect on the reduced Cu species. On a broader scale, the identification of metallic Cu NPs within organic material in surficial soil layers may impact future studies on the fate of Cu in organic-rich soils. Finally, I recommend that researchers planning to characterize soil organic material (or similar soft material) with a combination of FIB and TEM should use other sample preparation techniques, such as cryo-FIB or ultramicrotoming, as this would prevent significant loss of sample material and minimize the deposition of Ga^+ within the sample.

References

1. J. O. Nriagu, A History of Global Metal Pollution, *Science*, 1996, **272**, 223.

2. P. Adamo, S. Dudka, M. J. Wilson and W. J. McHardy, Chemical and mineralogical forms of Cu and Ni in contaminated soils from the Sudbury mining and smelting region, Canada, *Environmental Pollution*, 1996, **91**, 11-19.

3. P. J. Henderson, I. McMartin, G. E. Hall, J. B. Percival and D. A. Walker, The chemical and physical characteristics of heavy metals in humus and till in the vicinity of the base metal smelter at Flin Flon, Manitoba, Canada, *Environmental Geology*, 1998, **34**, 39-58.

4. J. Kierczak, A. Potysz, A. Pietranik, R. Tyszka, M. Modelska, C. Néel, V. Ettler and M. Mihaljevič, Environmental impact of the historical Cu smelting in the Rudawy Janowickie Mountains (south-western Poland), *Journal of Geochemical Exploration*, 2013, **124**, 183-194.

5. B. Kříbek, V. Majer, F. Veselovský and I. Nyambe, Discrimination of lithogenic and anthropogenic sources of metals and sulphur in soils of the central-northern part of the Zambian Copperbelt Mining District: A topsoil vs. subsurface soil concept, *Journal of Geochemical Exploration*, 2010, **104**, 69-86.

6. A. Davis, M. V. Ruby, M. Bloom, R. Schoof, G. Freeman and P. D. Bergstrom, Mineralogic Constraints on the Bioavailability of Arsenic in Smelter-Impacted Soils, *Environmental Science & Technology*, 1996, **30**, 392-399.

7. V. Ettler, B. Kříbek, V. Majer, I. Knésl and M. Mihaljevič, Differences in the bioaccessibility of metals/metalloids in soils from mining and smelting areas (Copperbelt, Zambia), *Journal of Geochemical Exploration*, 2012, **113**, 68-75.

8. J. S. Rieuwerts, The mobility and bioavailability of trace metals in tropical soils: a review, *Chemical Speciation & Bioavailability*, 2007, **19**, 75-85.

9. V. Ettler, Z. Johan, B. Kříbek, F. Veselovský, M. Mihaljevič, A. Vaněk, V. Penížek, V. Majer, O. Sracek, B. Mapani, F. Kamona and I. Nyambe, Composition and fate of mine- and smelter-derived particles in soils of humid subtropical and hot semi-arid areas, *Science of The Total Environment*, 2016, **563-564**, 329-339.

10. S. Lanteigne, M. Schindler and A. McDonald, Distribution of metals and metalloids in smelter-derived particulate matter in soils and mineralogical insights into their retention and release in a low-T environment, *The Canadian Mineralogist*, 2014, **52**, 453-471.

11. S. Lanteigne, M. Schindler, A. M. McDonald, K. Skeries, Y. Abdu, N. M. Mantha, M. Murayama, F. C. Hawthorne and M. F. Hochella, Mineralogy and Weathering of Smelter-Derived Spherical Particles in Soils: Implications for the Mobility of Ni and Cu in the Surficial Environment, *Water, Air, & Soil Pollution*, 2012, **223**, 3619-3641.

12. M. Schindler and M. F. Hochella, Sequestration of Pb-Zn-Sb- and As-bearing incidental nanoparticles by mineral surface coatings and mineralized organic matter in soils, *Environmental Science: Processes & Impacts*, 2017, **19**, 1016-1027.

13. C. Samuelsson and B. Björkman, *Dust forming mechanisms in the gas cleaning system after the copper converting process: (II). Thermodynamic studies*, 1998.

14. J. Csavina, J. Field, M. P. Taylor, S. Gao, A. Landázuri, E. A. Betterton and A. E. Sáez, A review on the importance of metals and metalloids in atmospheric dust and aerosol from mining operations, *Science of The Total Environment*, 2012, **433**, 58-73.

15. V. Ettler, A. Vaněk, M. Mihaljevič and P. Bezdička, Contrasting lead speciation in forest and tilled soils heavily polluted by lead metallurgy, *Chemosphere*, 2005, **58**, 1449-1459.

16. V. Ettler, M. Mihaljevič and M. Komárek, ICP-MS measurements of lead isotopic ratios in soils heavily contaminated by lead smelting: tracing the sources of pollution, *Analytical and Bioanalytical Chemistry*, 2004, **378**, 311-317.

17. G. Spiers, C. Hawson and F. Prevost, Metal Levels in the Soils of the Sudbury Smelter Footprint, *Sudbury Regional Soils Project*, 2004.

18. T. Sterckeman, F. Douay, N. Proix and H. Fourrier, Vertical distribution of Cd, Pb and Zn in soils near smelters in the North of France, *Environmental Pollution*, 2000, **107**, 377-389.

19. F. Degryse, E. Smolders and D. R. Parker, Partitioning of metals (Cd, Co, Cu, Ni, Pb, Zn) in soils: concepts, methodologies, prediction and applications – a review, *European Journal of Soil Science*, 2009, **60**, 590-612.

20. J. L. Everhart, D. McNear, E. Peltier, D. van der Lelie, R. L. Chaney and D. L. Sparks, Assessing nickel bioavailability in smelter-contaminated soils, *Science of The Total Environment*, 2006, **367**, 732-744.

21. M. Vítková, V. Ettler, J. Hyks, T. Astrup and B. Kříbek, Leaching of metals from copper smelter flue dust (Mufulira, Zambian Copperbelt), *Applied Geochemistry*, 2011, **26**, S263-S266.

22. *Canadian Mineral Production in 2016*, Natural Resources Canada, 2017.

23. Kidd Creek Copper and Zinc Mine, Ontario, Canada, http://www.mining-technology.com/projects/kidd_creek, (accessed May 1, 2017).

24. P. Coursol, N. Tripathi, P. Mackey, T. Leggett and A. Salomon de Friedberg, Slag Chemistry of the Mitsubishi S and Cl Furnaces at the Xstrata Copper-Kidd Metallurgical Site, *Canadian Metallurgical Quarterly*, 2010, **49**, 255-262.

25. Environmental Monitoring and Reporting Branch, *Timmins Air Quality Study 2003*, Ontario Ministry of the Environment, Canada, 2004.

26. J. A. Richard, Quaternary Geology of the Pamour Area, Map 2655.*Journal*, 2001.

27. D. L. Sparks, *Environmental Soil Chemistry*, Elsevier Science & Technology Books, 2nd edn., 2003.

28. N. Akaighe, R. I. MacCuspie, D. A. Navarro, D. S. Aga, S. Banerjee, M. Sohn and V. K. Sharma, Humic Acid-Induced Silver Nanoparticle Formation Under Environmentally Relevant Conditions, *Environmental Science & Technology*, 2011, **45**, 3895-3901.

29. F. H. Frimmel, F. von der Kammer and H. C. Flemming, *Colloidal Transport in Porous Media*, Springer Berlin Heidelberg, 2010.

30. K. H. Tan, *Humic Matter in Soil and the Environment: Principles and Controversies*, CRC Press, 2003.

31. G. Sposito, *The Chemistry of Soils*, Oxford University Press, 1989.

32. L. Kummer, V. d. F. Melo and Y. J. Barros, Lead and zinc in the structure of organic and mineral soil components, *Revista Brasileira de Ciência do Solo*, 2013, **37**, 438-449.

33. E. J. Elzinga and D. L. Sparks, Nickel Sorption Mechanisms in a Pyrophyllite–Montmorillonite Mixture, *Journal of Colloid and Interface Science*, 1999, **213**, 506-512.

34. O. Selinus and B. J. Alloway, *Essentials of Medical Geology: Impacts of the Natural Environment on Public Health*, Elsevier Academic Press, 2005.

35. M. F. Benedetti, W. H. Van Riemsdijk, L. K. Koopal, D. G. Kinniburgh, D. C. Gooddy and C. J. Milne, Metal ion binding by natural organic matter: From the model to the field, *Geochimica et Cosmochimica Acta*, 1996, **60**, 2503-2513.

36. S. Boudesocque, E. Guillon, M. Aplincourt, E. Marceau and L. Stievano, Sorption of Cu(II) onto vineyard soils: Macroscopic and spectroscopic investigations, *Journal of Colloid and Interface Science*, 2007, **307**, 40-49.

37. K. Flogeac, E. Guillon and M. Aplincourt, Surface Complexation of Copper(II) on Soil Particles: EPR and XAFS Studies, *Environmental Science & Technology*, 2004, **38**, 3098-3103.

38. A. R. Jacobson, S. Dousset, F. Andreux and P. C. Baveye, Electron Microprobe and Synchrotron X-ray Fluorescence Mapping of the Heterogeneous Distribution of Copper

in High-Copper Vineyard Soils, *Environmental Science & Technology*, 2007, **41**, 6343-6349.

39. D. G. Strawn and L. L. Baker, Speciation of Cu in a Contaminated Agricultural Soil Measured by XAFS, μ-XAFS, and μ-XRF, *Environmental Science & Technology*, 2008, **42**, 37-42.

40. D. G. Strawn and L. L. Baker, Molecular characterization of copper in soils using X-ray absorption spectroscopy, *Environmental Pollution*, 2009, **157**, 2813-2821.

41. P. J. C. Favas, J. Pratas, M. E. P. Gomes and V. Cala, Selective chemical extraction of heavy metals in tailings and soils contaminated by mining activity: Environmental implications, *Journal of Geochemical Exploration*, 2011, **111**, 160-171.

42. J. Yang, J. Liu, J. J. Dynes, D. Peak, T. Regier, J. Wang, S. Zhu, J. Shi and J. S. Tse, Speciation and distribution of copper in a mining soil using multiple synchrotron-based bulk and microscopic techniques, *Environmental Science and Pollution Research*, 2014, **21**, 2943-2954.

43. T. E. Alcacio, D. Hesterberg, J. W. Chou, J. D. Martin, S. Beauchemin and D. E. Sayers, Molecular scale characteristics of Cu(II) bonding in goethite–humate complexes, *Geochimica et Cosmochimica Acta*, 2001, **65**, 1355-1366.

44. L. Warren and E. Haack, Biogeochemical controls on metal behavior in freshwater environments, *Earth-Science Reviews*, 2001, **54**, 261-320.

45. C. L. Peacock and D. M. Sherman, Copper(II) sorption onto goethite, hematite and lepidocrocite: a surface complexation model based on ab initio molecular geometries and EXAFS spectroscopy1 1Associate editor: D. L. Sparks, *Geochimica et Cosmochimica Acta*, 2004, **68**, 2623-2637.

46. G. R. Aiken, H. Hsu-Kim and J. N. Ryan, Influence of Dissolved Organic Matter on the Environmental Fate of Metals, Nanoparticles, and Colloids, *Environmental Science & Technology*, 2011, **45**, 3196-3201.

47. J. P. Gustafsson, P. Pechová and D. Berggren, Modeling Metal Binding to Soils: The Role of Natural Organic Matter, *Environmental Science & Technology*, 2003, **37**, 2767-2774.

48. S. E. Fendorf, G. M. Lamble, M. G. Stapleton, M. J. Kelley and D. L. Sparks, Mechanisms of chromium(III) sorption on silica. 1. Chromium(III) surface structure derived by extended x-ray absorption fine structure spectroscopy, *Environmental Science & Technology*, 1994, **28**, 284-289.

49. D. T. Scott, D. M. McKnight, E. L. Blunt-Harris, S. E. Kolesar and D. R. Lovley, Quinone Moieties Act as Electron Acceptors in the Reduction of Humic Substances by Humics-Reducing Microorganisms, *Environmental Science & Technology*, 1998, **32**, 2984-2989.

50. Z. Struyk and G. Sposito, Redox properties of standard humic acids, *Geoderma*, 2001, **102**, 329-346.

51. M. Aeschbacher, M. Sander and R. P. Schwarzenbach, Novel Electrochemical Approach to Assess the Redox Properties of Humic Substances, *Environmental Science & Technology*, 2010, **44**, 87-93.

52. B. Fulda, A. Voegelin, F. Maurer, I. Christl and R. Kretzschmar, Copper Redox Transformation and Complexation by Reduced and Oxidized Soil Humic Acid. 1. X-ray Absorption Spectroscopy Study, *Environmental Science & Technology*, 2013, **47**, 10903-10911.

53. B. Gu, Y. Bian, C. L. Miller, W. Dong, X. Jiang and L. Liang, Mercury reduction and complexation by natural organic matter in anoxic environments, *Proceedings of the National Academy of Sciences*, 2011, **108**, 1479-1483.

54. A. N. Pham, A. L. Rose and T. D. Waite, Kinetics of Cu(II) Reduction by Natural Organic Matter, *The Journal of Physical Chemistry A*, 2012, **116**, 6590-6599.

55. R. Kretzschmar and H. Sticher, Transport of Humic-Coated Iron Oxide Colloids in a Sandy Soil: Influence of Ca2+ and Trace Metals, *Environmental Science & Technology*, 1997, **31**, 3497-3504.

56. R. Kretzschmar and T. Schäfer, Metal Retention and Transport on Colloidal Particles in the Environment, *Elements*, 2005, **1**, 205-210.

57. M. Schindler and M. F. Hochella, Nanomineralogy as a new dimension in understanding elusive geochemical processes in soils: The case of low-solubility-index elements, *Geology*, 2016, **44**, 515-518.

58. Y. Yang, B. Chen, J. Hower, M. Schindler, C. Winkler, J. Brandt, R. Di Giulio, J. Ge, M. Liu, Y. Fu, L. Zhang, Y. Chen, S. Priya and M. F. Hochella, Discovery and ramifications of incidental Magnéli phase generation and release from industrial coal-burning, *Nature Communications*, 2017, **8**, 194.

59. Y. Yang, B. P. Colman, E. S. Bernhardt and M. F. Hochella, Importance of a Nanoscience Approach in the Understanding of Major Aqueous Contamination Scenarios: Case Study from a Recent Coal Ash Spill, *Environmental Science & Technology*, 2015, **49**, 3375-3382.

60. M. H. Loretto, *Electron Beam Analysis of Materials*, Springer Netherlands, 1st edn., 1984.

61. D. A. Skoog, F. J. Holler and S. R. Crouch, *Principles of Instrumental Analysis*, Thomson Brooks/Cole, 6th edn., 2007.

62. F. Hofer, F. P. Schmidt, W. Grogger and G. Kothleitner, Fundamentals of electron energy-loss spectroscopy, *IOP Conference Series: Materials Science and Engineering*, 2016, **109**, 012007.

63. My Scope: Transmission Electron Microscopy, http://www.ammrf.org.au/myscope/tem/introduction/, (accessed November 12, 2017).

64. F. Krumeich, Electron Microscopy - Electron Diffraction, http://www.microscopy.ethz.ch/ED-1.htm, (accessed December 4, 2017).

65. M. Law, Crystal Structure Analysis, http://www.chem.uci.edu/~lawm/263 4.pdf, (accessed December, 2017).

66. J. Yu, J. Liu, J. Zhang and J. Wu, TEM investigation of FIB induced damages in preparation of metal material TEM specimens by FIB, *Materials Letters*, 2006, **60**, 206-209.

67. N. D. Bassim, B. T. De Gregorio, A. L. D. Kilcoyne, K. Scott, T. Chou, S. Wirick, G. Cody and R. M. Stroud, Minimizing damage during FIB sample preparation of soft materials, *Journal of Microscopy*, 2012, **245**, 288-301.

68. J. Mayer, L. A. Giannuzzi, T. Kamino and J. Michael, TEM Sample Preparation and FIB-Induced Damage, *MRS Bulletin*, 2011, **32**, 400-407.

69. National Pollutant Release Inventory, *Summary Report: Reviewed Facility-Reported Data 2015*, Environment and Climate Change Canada, 2016.

70. V. Ettler, Soil contamination near non-ferrous metal smelters: A review, *Applied Geochemistry*, 2016, **64**, 56-74.

71. B. Qasim, M. Motelica-Heino, E. Joussein, M. Soubrand and A. Gauthier, Potentially toxic element phytoavailability assessment in Technosols from former smelting and mining areas, *Environmental Science and Pollution Research*, 2015, **22**, 5961-5974.

72. R. Knight and P. J. Henderson, Smelter dust in humus around Rouyn-Noranda, Quebec, *Geochemistry: Exploration, Environment, Analysis*, 2006, **6**, 203-214.

73. M. D. Buatier, S. Sobanska and F. Elsass, TEM-EDX investigation on Zn- and Pb-contaminated soils, *Applied Geochemistry*, 2001, **16**, 1165-1177.

74. N. M. Mantha, M. Schindler, M. Murayama and M. F. Hochella, Silica- and sulfate-bearing rock coatings in smelter areas: Products of chemical weathering and atmospheric

pollution I. Formation and mineralogical composition, *Geochimica et Cosmochimica Acta*, 2012, **85**, 254-274.

75. J. N. Caplette, M. Schindler and T. K. Kyser, The black rock coatings in Rouyn-Noranda, Québec: fingerprints of historical smelter emissions and the local ore, *Canadian Journal of Earth Sciences*, 2015, **52**, 952-965.

76. M. Schindler and M. F. Hochella, Soil memory in mineral surface coatings: Environmental processes recorded at the nanoscale, *Geology*, 2015, **43**, 415-418.

77. M. Schindler, S. Lanteigne, A. McDonald and M. F. Hochella, Evidence of Cu- and Ni-bearing Surface Precipitates and Adsorption Complexes in Remediated Soils At the Nanoscale: a Tem, Micro-raman, and Laser-ablation Icp-ms Study of Mineral Surface Coatings, *The Canadian Mineralogist*, 2016, **54**, 285-309.

78. A. Neagoe, V. Iordache and I. C. Fărcăşanu, in *Bio-Geo Interactions in Metal-Contaminated Soils*, eds. E. Kothe and A. Varma, Springer Berlin Heidelberg, Berlin, Heidelberg, 2012, DOI: 10.1007/978-3-642-23327-2_15, pp. 297-325.

79. A. Kabata-Pendias, *Trace Elements in Soils and Plants, Fourth Edition*, Taylor & Francis, New York, 2010.

80. J. Xu, W. Tan, J. Xiong, M. Wang, L. Fang and L. K. Koopal, Copper binding to soil fulvic and humic acids: NICA-Donnan modeling and conditional affinity spectra, *Journal of Colloid and Interface Science*, 2016, **473**, 141-151.

81. National Pollutant Release Inventory, *Historical Substance Reports: Falconbridge Ltd-Kidd Metallurgical Div./Kidd Metallurgical Site: Total Particulate Matter*, Environment and Climate Change Canada, 2017.

82. F. Amirault and O. M. Burnham, in *Summary of Field Work and Other Activities 2013, Open File Report 6290*, Ontario Geological Survey, 2013, pp. 43-41 to 43-45.

83. in *British Columbia Environmental Laboratory Manual*, ed. J. Austin, Environmental Monitoring, Reporting & Economics Section, Knowledge Management Branch, B.C. Ministry of Environment, Victoria, BC, 2015.

84. O. M. Burnham, in *Summary of Field Work and Other Activities, Open File Report 6333*, Ontario Geological Survey, 2017, pp. 31-31 to 31-10.

85. J. L. Pouchou and F. Pichoir, *New model for quantitative x-ray microanalysis. Part I: Application to the analysis of homogeneous samples [English Ed.]*, 1984.

86. K. Winterhalder, *Early History of Human Activities in the Sudbury Area and Ecological Damage to the Landscape*, 1995.

87. E. I. B. Chopin and B. J. Alloway, Trace element partitioning and soil particle characterisation around mining and smelting areas at Tharsis, Ríotinto and Huelva, SW Spain, *Science of The Total Environment*, 2007, **373**, 488-500.

88. M. Kosmulski, *Surface Charging and Points of Zero Charge*, CRC Press, 2009.

89. H. I. Adegoke, F. A. Adekola, O. S. Fatoki and B. J. Ximba, Sorptive interaction of oxyanions with iron oxides: A review, *Pol J Environ Stud*, 2013, **22**, 7-24.

90. P. M. Bertsch and J. C. Seaman, Characterization of complex mineral assemblages: Implications for contaminant transport and environmental remediation, *Proceedings of the National Academy of Sciences*, 1999, **96**, 3350.

91. Y. Li, N. Kawashima, J. Li, A. P. Chandra and A. R. Gerson, A review of the structure, and fundamental mechanisms and kinetics of the leaching of chalcopyrite, *Advances in Colloid and Interface Science*, 2013, **197-198**, 1-32.

92. S. W. Goh, A. N. Buckley, R. N. Lamb, R. A. Rosenberg and D. Moran, The oxidation states of copper and iron in mineral sulfides, and the oxides formed on initial exposure of chalcopyrite and bornite to air, *Geochimica et Cosmochimica Acta*, 2006, **70**, 2210-2228.

93. M. L. Farquhar, P. L. Wincott, R. A. Wogelius and D. J. Vaughan, Electrochemical oxidation of the chalcopyrite surface: an XPS and AFM study in solution at pH 4, *Applied Surface Science*, 2003, **218**, 34-43.

94. R. M. Cornell and U. Schwertmann, *The Iron Oxides: Structure, Properties, Reactions, Occurrence and Uses*, 2003.

95. J. Baumgartner, A. Dey, P. H. H. Bomans, C. Le Coadou, P. Fratzl, N. A. J. M. Sommerdijk and D. Faivre, Nucleation and growth of magnetite from solution, *Nature Materials Letters*, 2013, **12**, 310-314.

96. V. Barrn and J. Torrent, Evidence for a simple pathway to maghemite in Earth and Mars soils, *Geochimica et Cosmochimica Acta*, 2002, **66**, 2801-2806.

97. X. Gong, J. Li, Y. Lin, X. Liu, L. Chen, J. Li and D. Li, Formation of highly crystalline maghemite nanoparticles from ferrihydrite in the liquid phase, *Chinese Science Bulletin*, 2014, **59**, 3904-3911.

98. A. Putnis, Mineral Replacement Reactions, *Reviews in Mineralogy and Geochemistry*, 2009, **70**, 87-124.

99. E. S. Ilton and D. R. Veblen, Copper inclusions in sheet silicates from porphyry Cu deposits, *Nature*, 1988, **334**, 516.

100. E. S. Ilton and D. R. Veblen, Origin and mode of copper enrichment in biotite from rocks associated with porphyry copper deposits; a transmission electron microscopy investigation, *Economic Geology*, 1993, **88**, 885-900.

101. E. S. Ilton, D. Earley, D. C. Marozas and D. R. Veblen, Reaction of some trioctahedral micas with copper sulfate solutions at 25 degrees C and 1 atmosphere; an electron microprobe and TEM investigation, *Economic Geology*, 1992, **87**, 1813-1829.

102. J. H. Ahn, H. Xu and P. R. Buseck, Transmission electron microscopy of native copper inclusions in illite, *Clay and Clay Minerals*, 1997, **45**, 295-297.

103. R. E. W. Lett and W. K. Fletcher, Syngenetic sulphide minerals in a copper-rich bog, *Mineralium Deposita*, 1980, **15**, 61-67.

104. T. S. Lovering, *Organic precipitation of metallic copper: Chapter C in Contributions to economic geology (short papers and preliminary reports), 1927: Part I - Metals and nonmetals except fuels*, Report 795C, Washington, D.C., 1927.

105. B. Fulda, A. Voegelin, K. Ehlert and R. Kretzschmar, Redox transformation, solid phase speciation and solution dynamics of copper during soil reduction and reoxidation as affected by sulfate availability, *Geochimica et Cosmochimica Acta*, 2013, **123**, 385-402.

106. K. Yang, G. Miao, W. Wu, D. Lin, B. Pan, F. Wu and B. Xing, Sorption of Cu2+ on humic acids sequentially extracted from a sediment, *Chemosphere*, 2015, **138**, 657-663.

107. E. J. O'Loughlin, S. D. Kelly, K. M. Kemner, R. Csencsits and R. E. Cook, Reduction of AgI, AuIII, CuII, and HgII by FeII/FeIII hydroxysulfate green rust, *Chemosphere*, 2003, **53**, 437-446.

108. A. F. White and M. L. Peterson, Reduction of aqueous transition metal species on the surfaces of Fe(II) -containing oxides, *Geochimica et Cosmochimica Acta*, 1996, **60**, 3799-3814.

109. D. Collins, T. Luxton, N. Kumar, S. Shah, V. K. Walker and V. Shah, Assessing the Impact of Copper and Zinc Oxide Nanoparticles on Soil: A Field Study, *PLOS ONE*, 2012, **7**, e42663.

110. A. Manceau, C. Lemouchi, M. Enescu, A.-C. Gaillot, M. Lanson, V. Magnin, P. Glatzel, B. A. Poulin, J. N. Ryan, G. R. Aiken, I. Gautier-Luneau and K. L. Nagy, Formation of Mercury Sulfide from Hg(II)–Thiolate Complexes in Natural Organic Matter, *Environmental Science & Technology*, 2015, **49**, 9787-9796.

111. M. K. Nduna, A. E. Lewis and P. Nortier, A model for the zeta potential of copper sulphide, *Colloids and Surfaces A: Physicochemical and Engineering Aspects*, 2014, **441**, 643-652.

112. J. P. Gramp, K. Sasaki, J. M. Bigham, O. V. Karnachuk and O. H. Tuovinen, Formation of Covellite (CuS) Under Biological Sulfate-Reducing Conditions, *Geomicrobiology Journal*, 2006, **23**, 613-619.

113. F.-A. Weber, A. Voegelin, R. Kaegi and R. Kretzschmar, Contaminant mobilization by metallic copper and metal sulphide colloids in flooded soil, *Nature Geoscience*, 2009, **2**, 267-271.

114. T. F. Rozan, M. E. Lassman, D. P. Ridge and G. W. Luther, III, Evidence for iron, copper and zinc complexation as multinuclear sulphide clusters in oxic rivers, *Nature*, 2000, **406**, 879+.

115. Y.-S. Jun, D. Kim and C. W. Neil, Heterogeneous Nucleation and Growth of Nanoparticles at Environmental Interfaces, *Accounts of Chemical Research*, 2016, **49**, 1681-1690.

116. G. A. Waychunas, C. S. Kim and J. F. Banfield, Nanoparticulate Iron Oxide Minerals in Soils and Sediments: Unique Properties and Contaminant Scavenging Mechanisms, *Journal of Nanoparticle Research*, 2005, **7**, 409-433.

117. E. M Hotze, T. Phenrat and G. Lowry, *Nanoparticle Aggregation: Challenges to Understanding Transport and Reactivity in the Environment*, 2010.

118. J. J. De Yoreo, P. U. P. A. Gilbert, N. A. J. M. Sommerdijk, R. L. Penn, S. Whitelam, D. Joester, H. Zhang, J. D. Rimer, A. Navrotsky, J. F. Banfield, A. F. Wallace, F. M. Michel, F. C. Meldrum, H. Cölfen and P. M. Dove, Crystallization by particle attachment in synthetic, biogenic, and geologic environments, *Science*, 2015, **349**.

119. J. Hur, B.-M. Lee and H.-S. Shin, Microbial degradation of dissolved organic matter (DOM) and its influence on phenanthrene–DOM interactions, *Chemosphere*, 2011, **85**, 1360-1367.

120. J. Kumpiene, A. Lagerkvist and C. Maurice, Stabilization of Pb- and Cu-contaminated soil using coal fly ash and peat, *Environmental Pollution*, 2007, **145**, 365-373.

121. R. T. Downs and M. Hall-Wallace, The American Mineralogist Crystal Structure Database, *American Mineralogist*, 2003, **88**, 247-250.

122. K. Koto and N. Morimoto, The crystal structure of anilite, *Acta Crystallographica Section B*, 2007, **26**, 915-924.

123. G. G. Christoph, C. E. Corbato and D. A. Hofmann, The Crystal Structure of Boehmite, *Clays and Clay Minerals*, 1979, **27**, 81-86.

124. G. Tunell and C. E. Adams, On the symmetry and crystal structure of bornite, *American Mineralogist*, 1949, **34**, 824-829.

125. G. Will, E. Hinze and A. R. M. Abdelraham, Crystal structure analysis and refinement of digenite, Cu1.8S, in the temperature range 20 to 500 C under controlled sulfur partial pressure, *American Mineralogist*, 2002, **14**, 591-598.

126. I. K. Suh, H. Ohta and Y. Waseda, High-temperature thermal expansion of six metallic elements measuredby dilatation method and X-ray diffraction, *Journal of Materials Science*, 1988, **23**, 757-760.

127. L. G. Berry, The crystal structure of covellite, CuS and klockmannite, CuSe, *American Mineralogist*, 1954, **39**, 504-509.

128. E. Prince and R. G. Treuting, The structure of tetragonal copper ferrite, *Acta Crystallographica*, 1956, **9**, 1025-1028.

129. R. J. Hill, Crystal structure refinement and electron density distribution in diaspore, *Physics and Chemistry of Minerals*, 1979, **5**, 179-200.

130. C. Pecharroman, T. Gonzalez-Carreno and J. E. Iglesias, The infrared dielectric properties of maghemite, gamma-Fe2O3, from reflectance measurement on pressed powders, *Physics and Chemistry of Minerals*, 1995, **22**, 21-29.

131. B. A. Wechsler, D. H. Lindsley and C. T. Prewitt, Crystal structure and cation distribution in titanomagnetites (Fe3-xTixO4), *American Mineralogist*, 1984, **69**, 754-770.

132. S. R. Hall and J. F. Rowland, The crystal structure of synthetic mooihoekite, Cu9Fe9S16, *Acta Crystallographica B*, 1973, **29**, 2365-2372.

Appendices

Appendix A. The following are tables and figures considered to be supplementary information.

Table S1. ICP-MS data for Cu, Zn, and Pb for the depth profiles of site 1.

Depth (cm)	Concentration (ppm)		
	Cu	Pb	Zn
1	9220	447	3280
2	8510	518	2770
3	7480	495	2440
4	5470	358	2390
5	3500	262	2721
6	2808	190	2295
7	1743	119	1942
8	1449	97	1600
9	911	75	1576
10	265	38	964
12.5	106	27	682

Table S2. Compiled data regarding the relative molar ratios and corresponding volumes between mooihoekite/ferrihydrite/ magnetite/maghemite. Sample calculations given below table.

Transformation Reaction	Molar Ratio	Molar Volumes (cm^3/mol)	Volume (cm^3)
$10Cu_9Fe_9S_{16} \rightarrow 9Fe_{10}O_{14}(OH)_2$	1 : 0.9	363 → 167	363 → 150
$3Fe_{10}O_{14}(OH)_2 \rightarrow 10Fe_3O_4$	1 : 3.3	167 → 45	150 → 149
$2Fe_3O_4 \rightarrow 3Fe_2O_3$	1 : 1.5	45 → 44	149 → 66

Sample calculation for molar ratio.

Assume 1 mol of mooihoekite (Mhk) dissolves to form ferrihydrite (Fhyd).

$$x \text{ mol Fhyd} = 9 \text{ mol Fhyd} \times \frac{1 \text{ mol Mhk}}{10 \text{ mol Mhk}} \quad \text{[as per stoichiometry]}$$

$$x \text{ mol Fhyd} = 0.9 \text{ mol Fhyd} \quad \text{[per 1 mol Mhk]}$$

Sample calculation for volumes produced after the transformation of Mhk to Fhyd.

$$x \text{ Volume Fhyd} = 0.9 \text{ mol Fhyd} \times 167 \text{ cm}^3/\text{mol} \quad \text{[as per molar ratio]}$$

$$x \text{ Volume Fhyd} = 150 \text{ cm}^3 \text{ Fhyd}$$

Figure S1. Site 1 vegetation and 0-15 cm soil profile. GPS Coordinates (latitude/longitude) 48.544719/-81.067873.

Figure S2. Site 2 (control) soil profile. GPS coordinates (48.599656/-81.009367)

Figure S3. Site 3 (control) soil profile. GPS coordinates (48.55593/-81.055307)

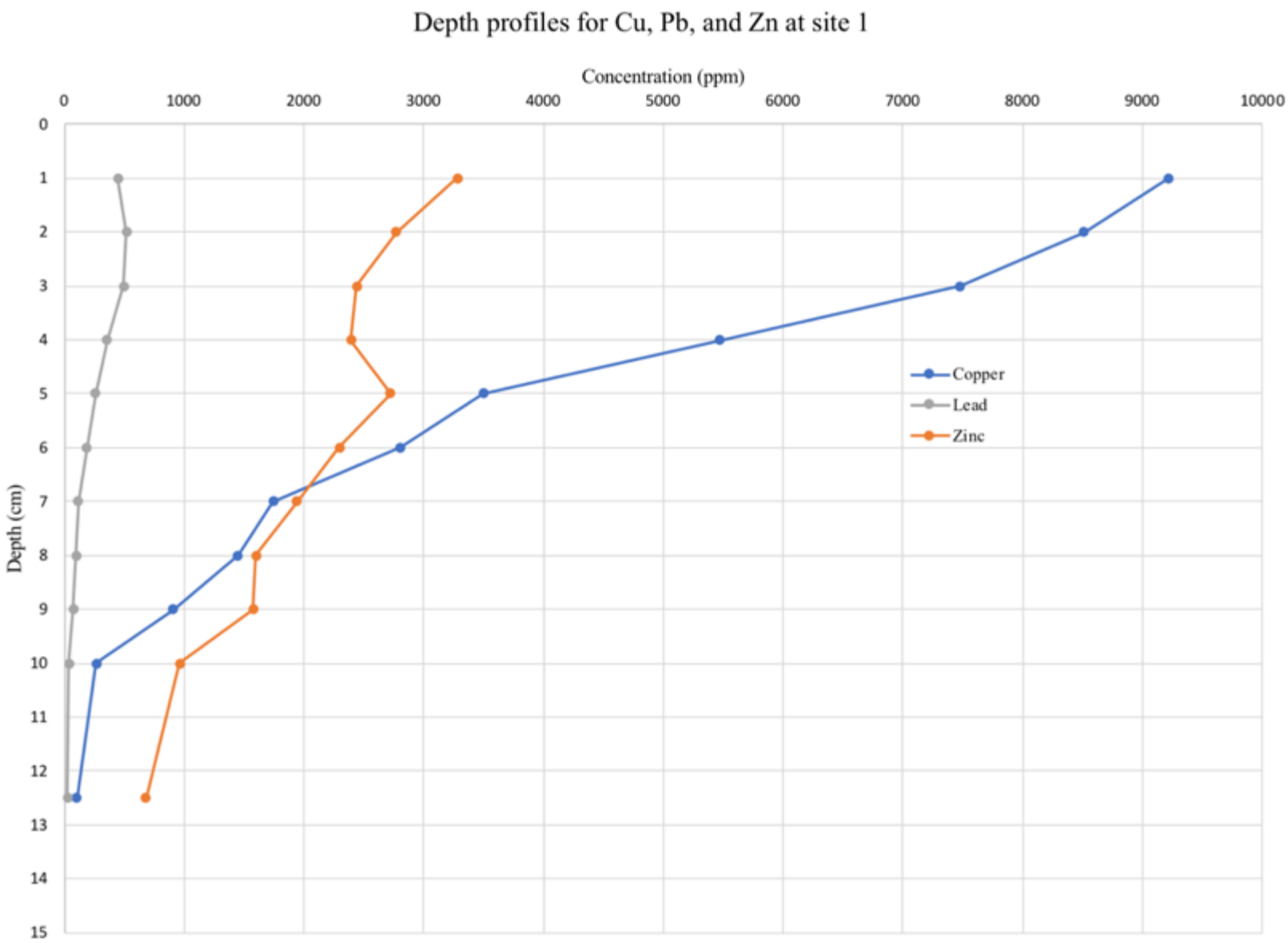

Figure S4. Depth profile of Cu (blue), Pb (gray), and Zn (orange) at site 1. The first 10 cm were digested and analyzed in 1 cm increments, then the 10-15 cm layer was analyzed as one fraction. Soil was digested using a reverse aqua regia digest and ICP-MS measurements were done at the Geo Labs.

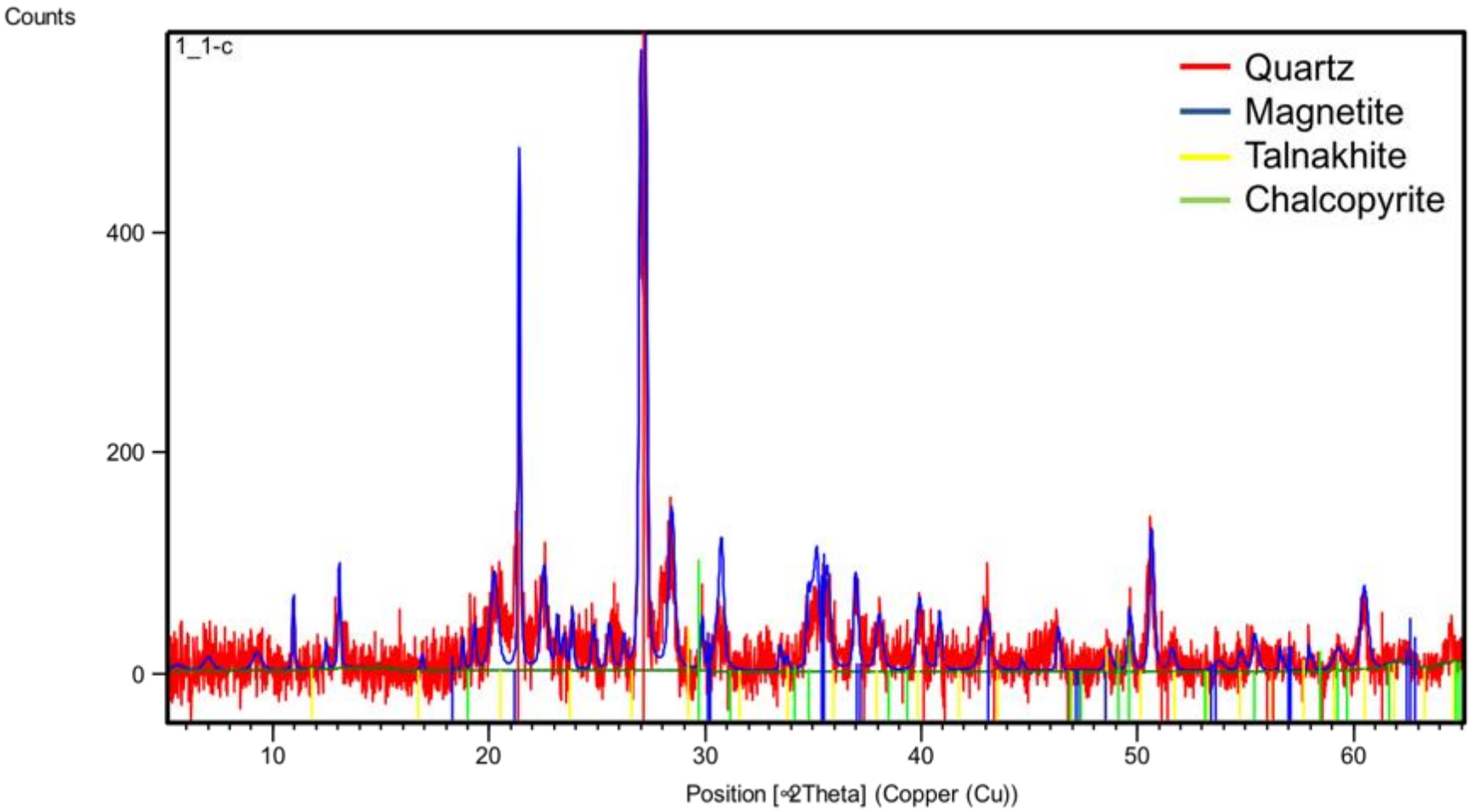

Figure S5. X-ray diffraction pattern of the coarse fraction from the 0-5 cm fraction of site 1, indicated by the blue outline. Coloured lines underneath the spectrum indicate the identified minerals.

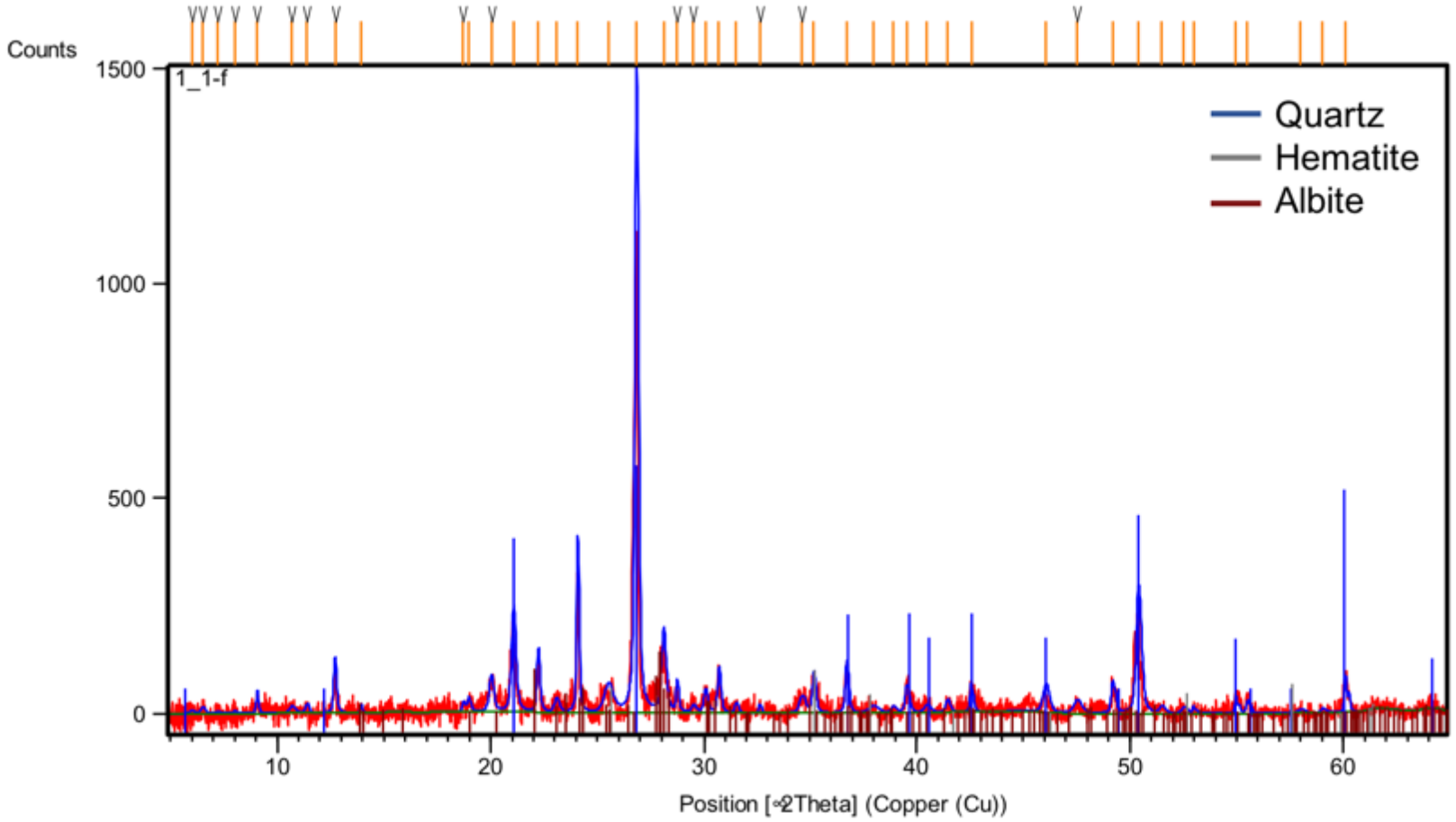

Figure S4. X-ray diffraction pattern of the fine fraction from the 0-5 cm fraction of site 1, indicated by the blue outline. Coloured lines underneath the spectrum indicate the identified minerals.

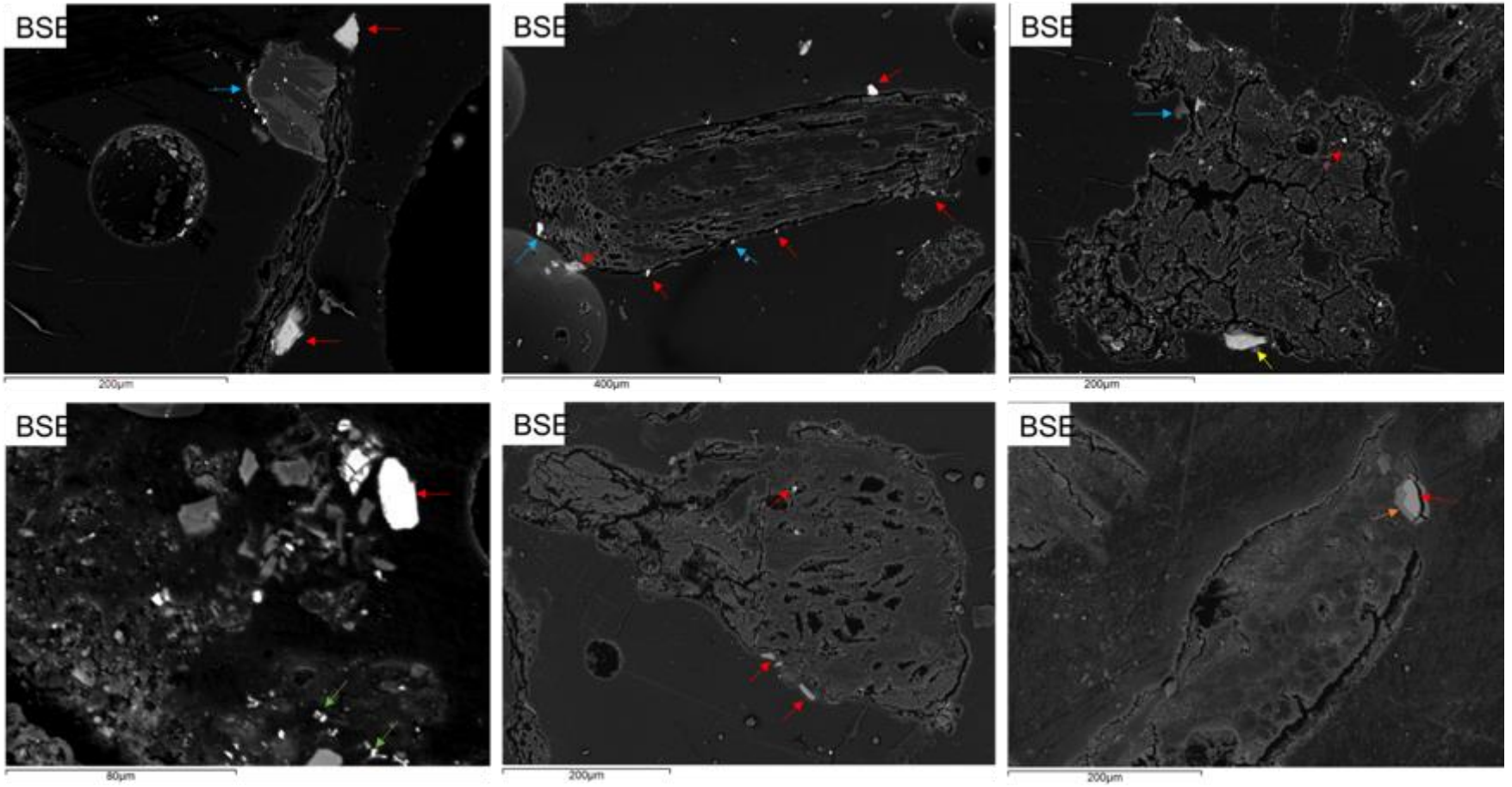

Figure S5. SEM backscattered electron images from the 0-5 cm, coarse fraction from site 1 indicating the predominance of Cu-Fe-sulfide grains (red arrows), minor amounts of silicon-based grains (blue arrows), and rare occurrences of various non-sulfide copper species (green arrows) or iron sulfides (yellow arrow). Orange arrow shown in last pane indicates an iron oxide layer.

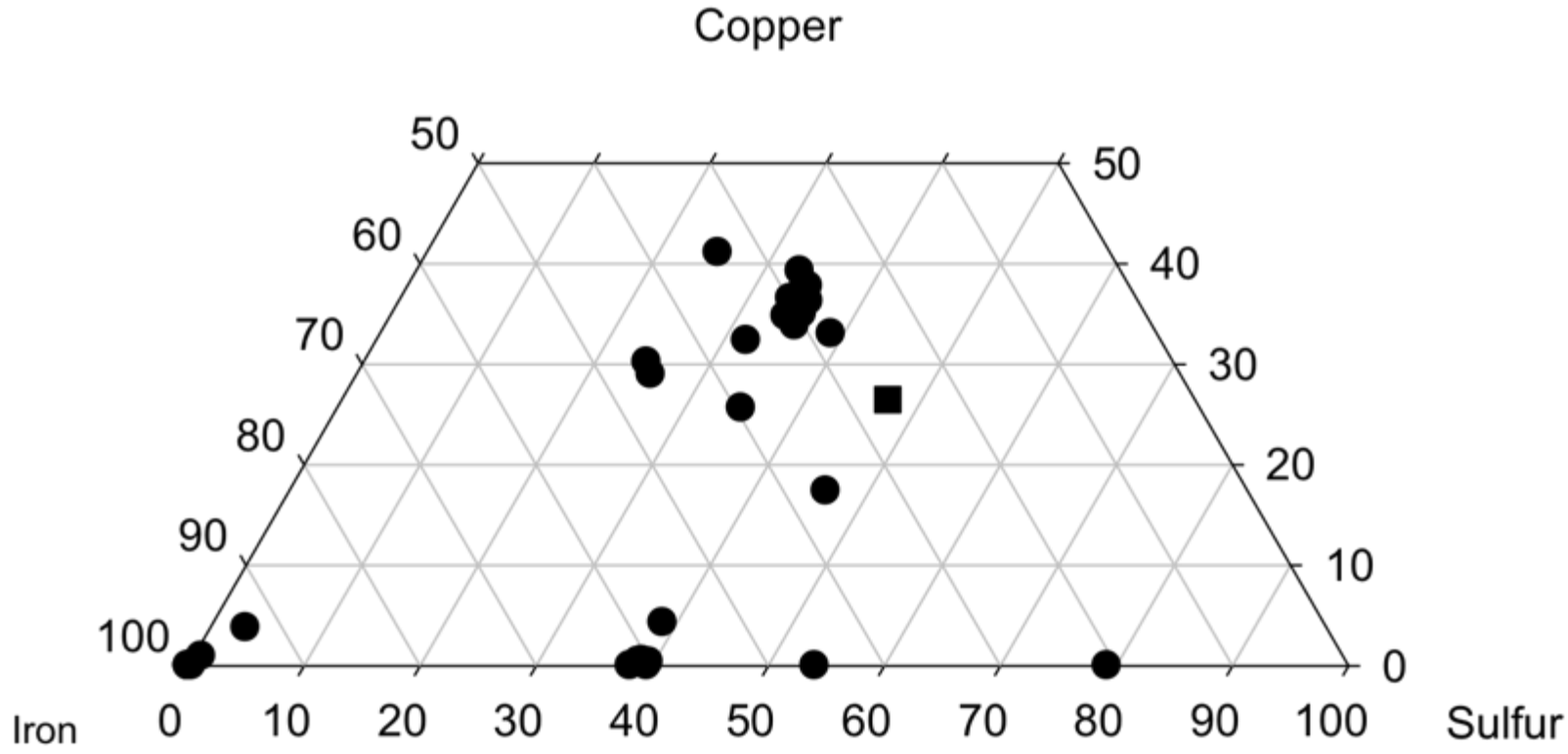

Figure S6. Ternary plot compiled using data from electron microprobe analysis of 63 mineral grains attached to organic residues in the coarse fraction of site 1. Circular dots in the middle represent a Cu/Fe/S fraction of 35:65:50, those on the Fe/S axis are likely iron sulfide minerals, and those that appear to be 100 % Fe are likely iron oxide species. The square dot indicates the ratio of Cu/Fe/S of mooihoekite.

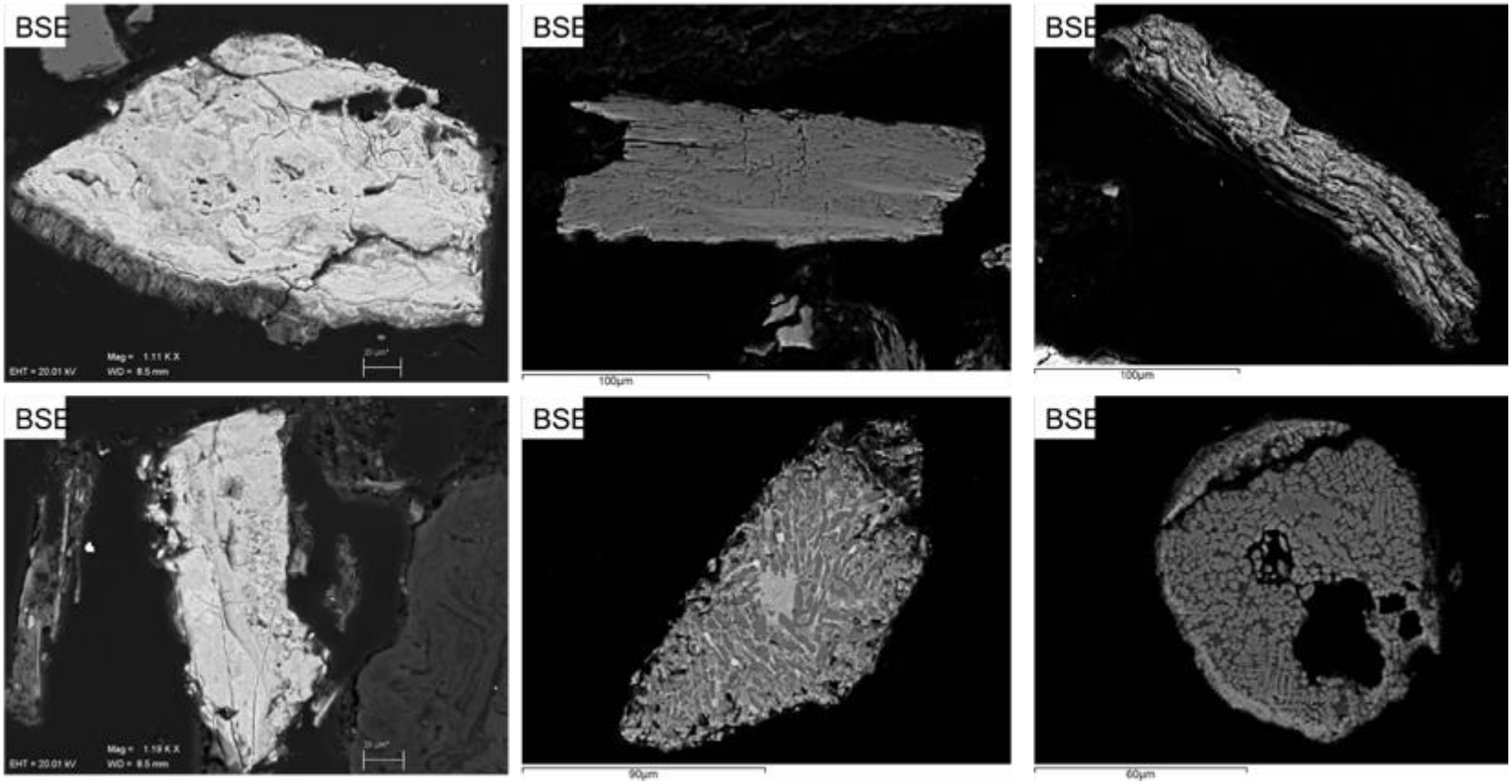

Figure S7. SEM backscattered electron images from the 0-5 cm, fine fraction (< 180 mm) from site 1 indicating silicified organic material, wind-blown slag particles, and smelter-derived PM

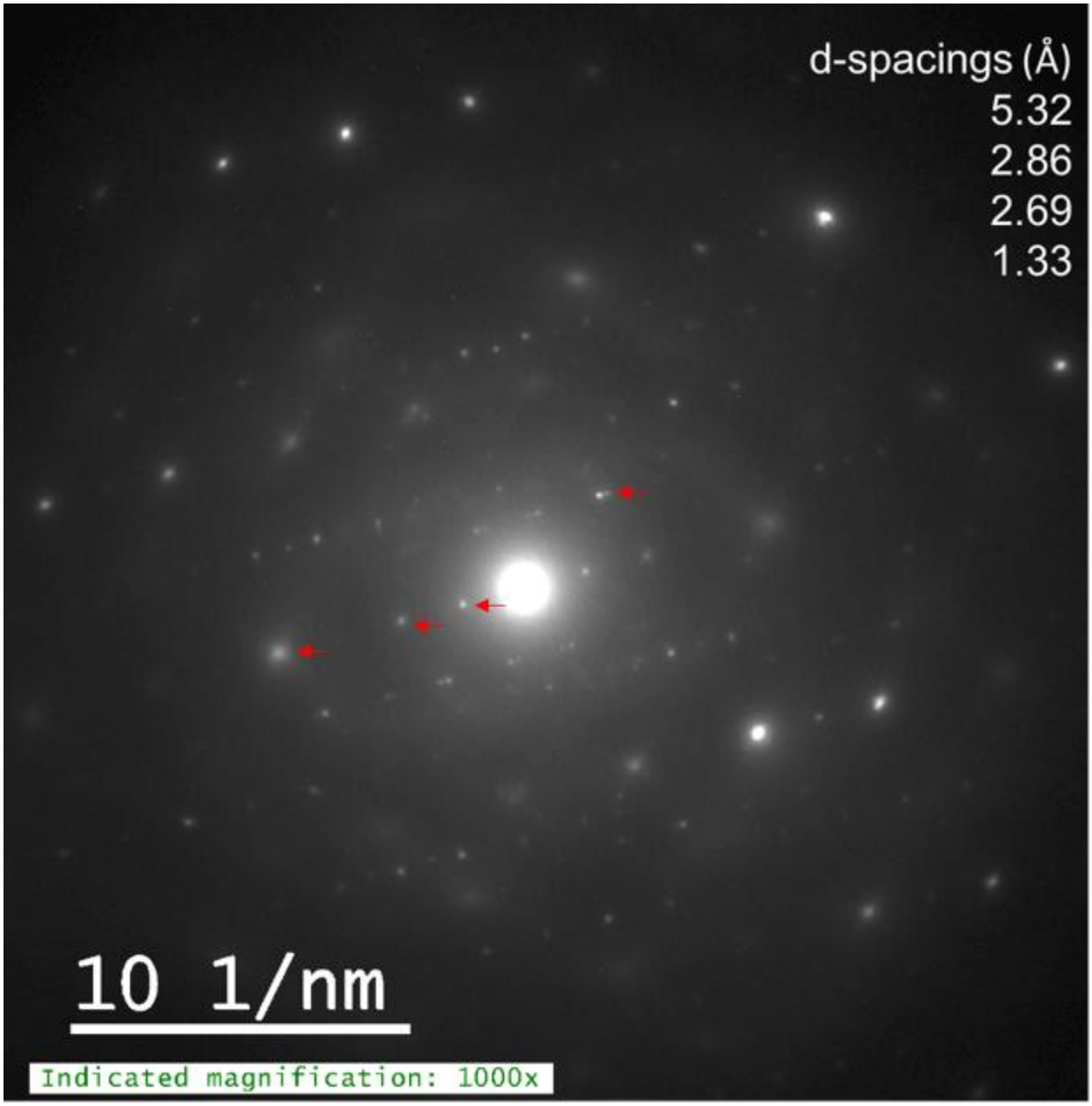

Figure S8. Selected area electron diffraction pattern of the main sulfide grain, mooihoekite.

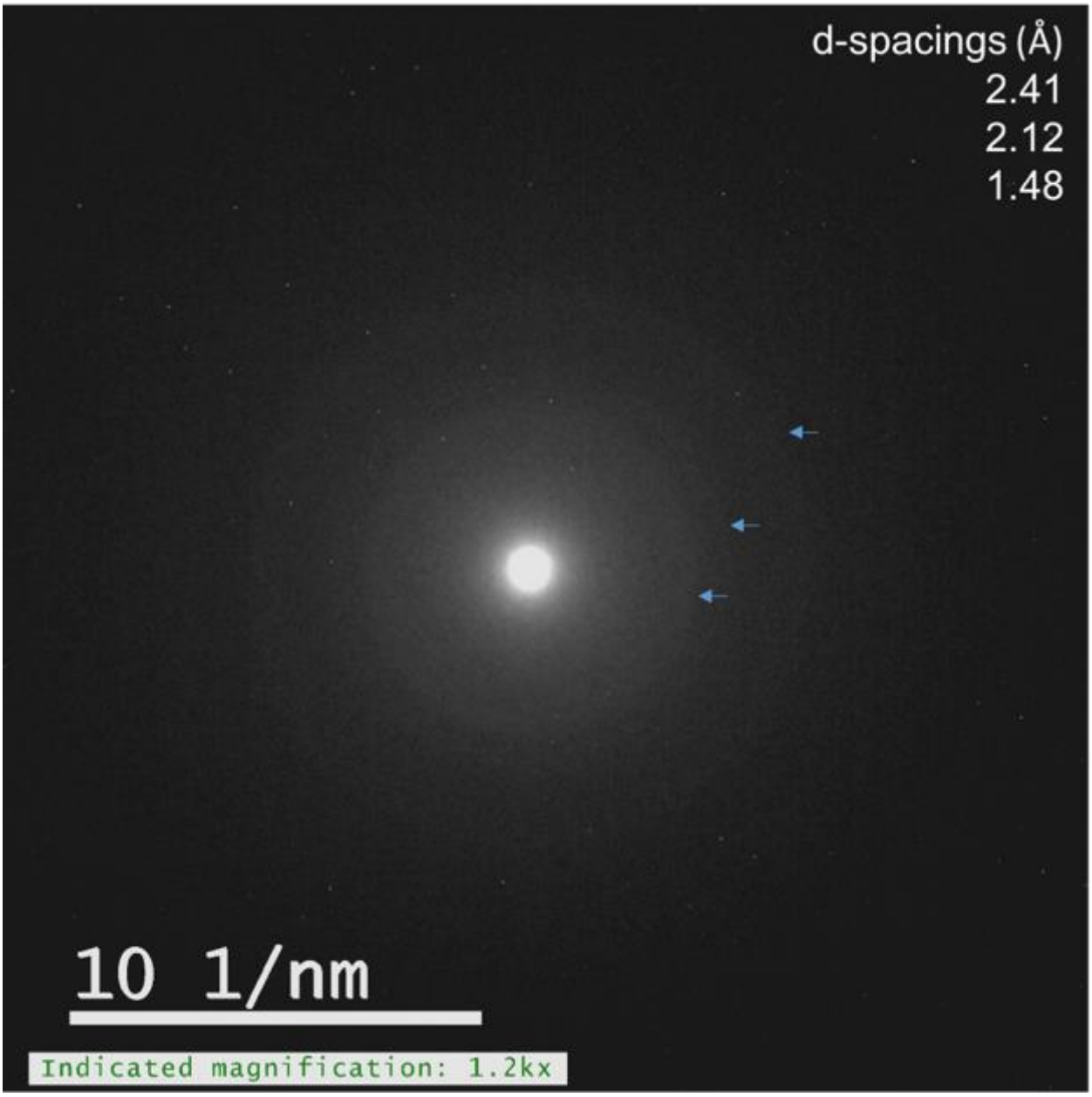

Figure S9. Selected area electron diffraction pattern of the alteration layer.

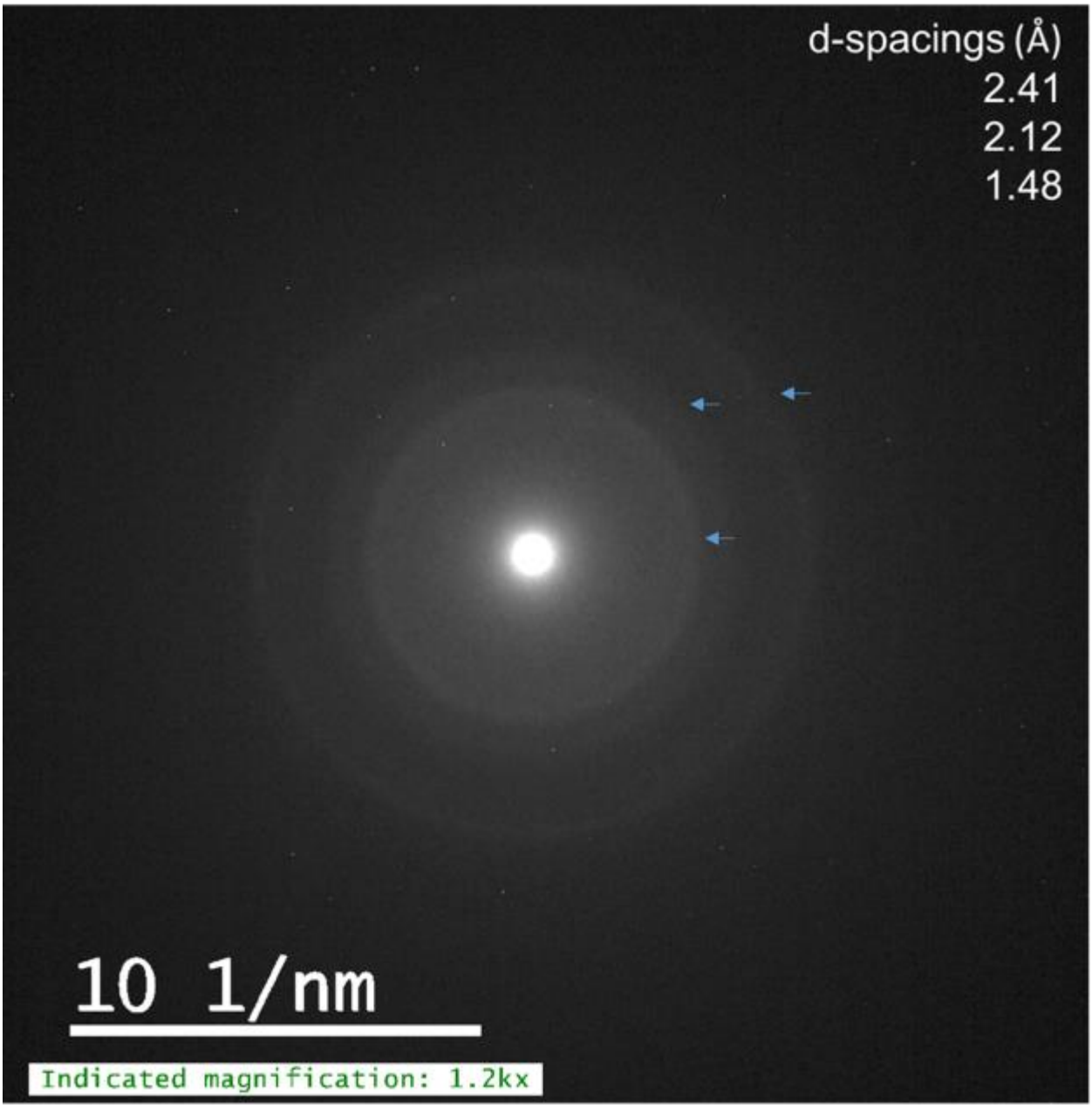

Figure S10. Selected area electron diffraction pattern of the iron oxide fragment at the interface.

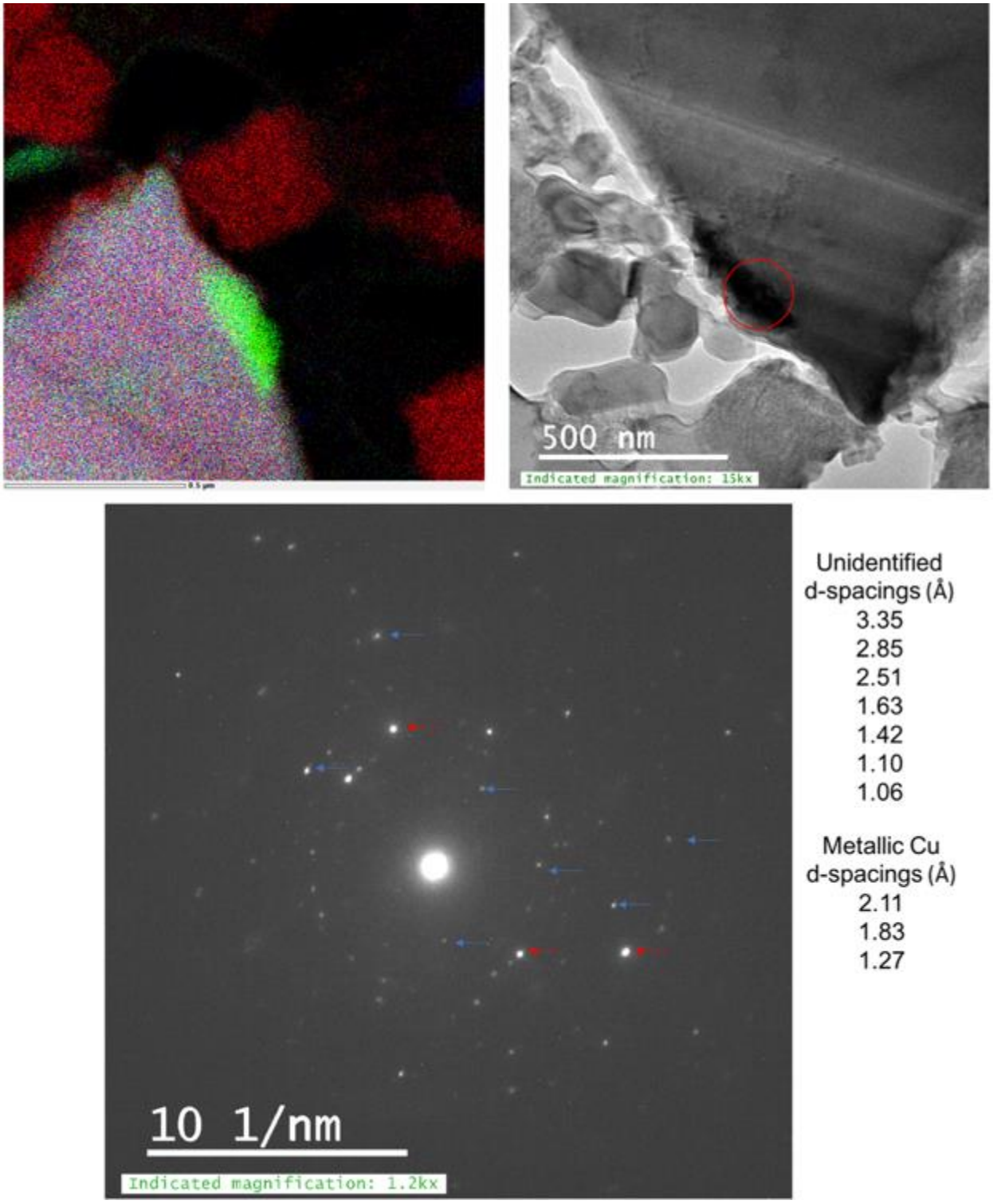

Figure S11. EDS mapping with Cu (green), Fe (red), and S (blue), revealing the Cu-rich rim. Rotated 180 ° STEM image with corresponding SAED pattern (red circle) of the Cu-rich area on the edge of the main sulfide where red arrows indicate d-spacings for metallic copper and blue arrows are various other spacings. EDS quantification indicated a ratio of 56/17/27 for Cu/Fe/S.

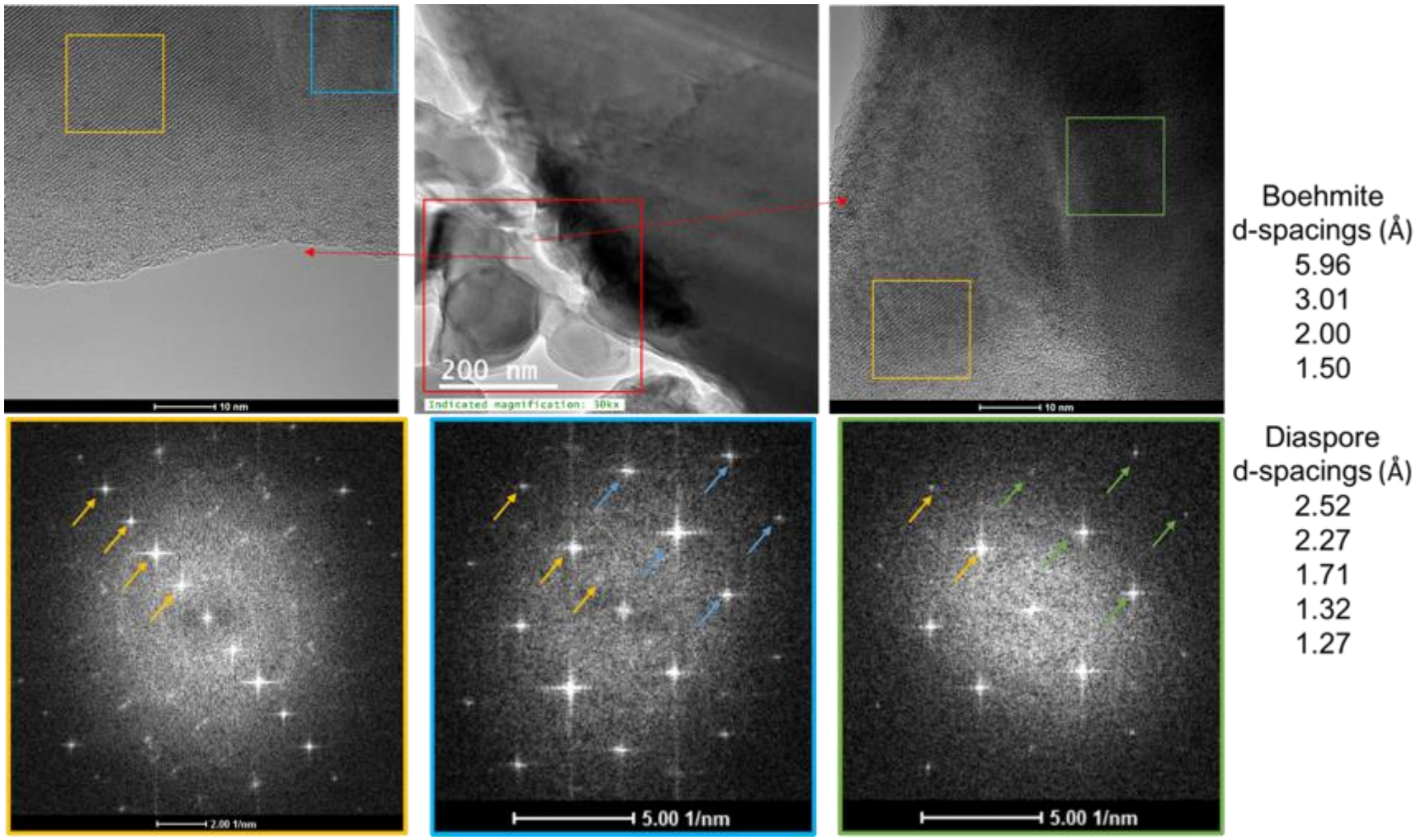

Figure S12. Scanning-TEM images and fast Fourier transformation patterns of aluminum hydroxides, boehmite (yellow) and diaspore (blue, green). Both diaspore patterns are mixed with boehmite. Select d spacings are indicated by arrows of matching colour.

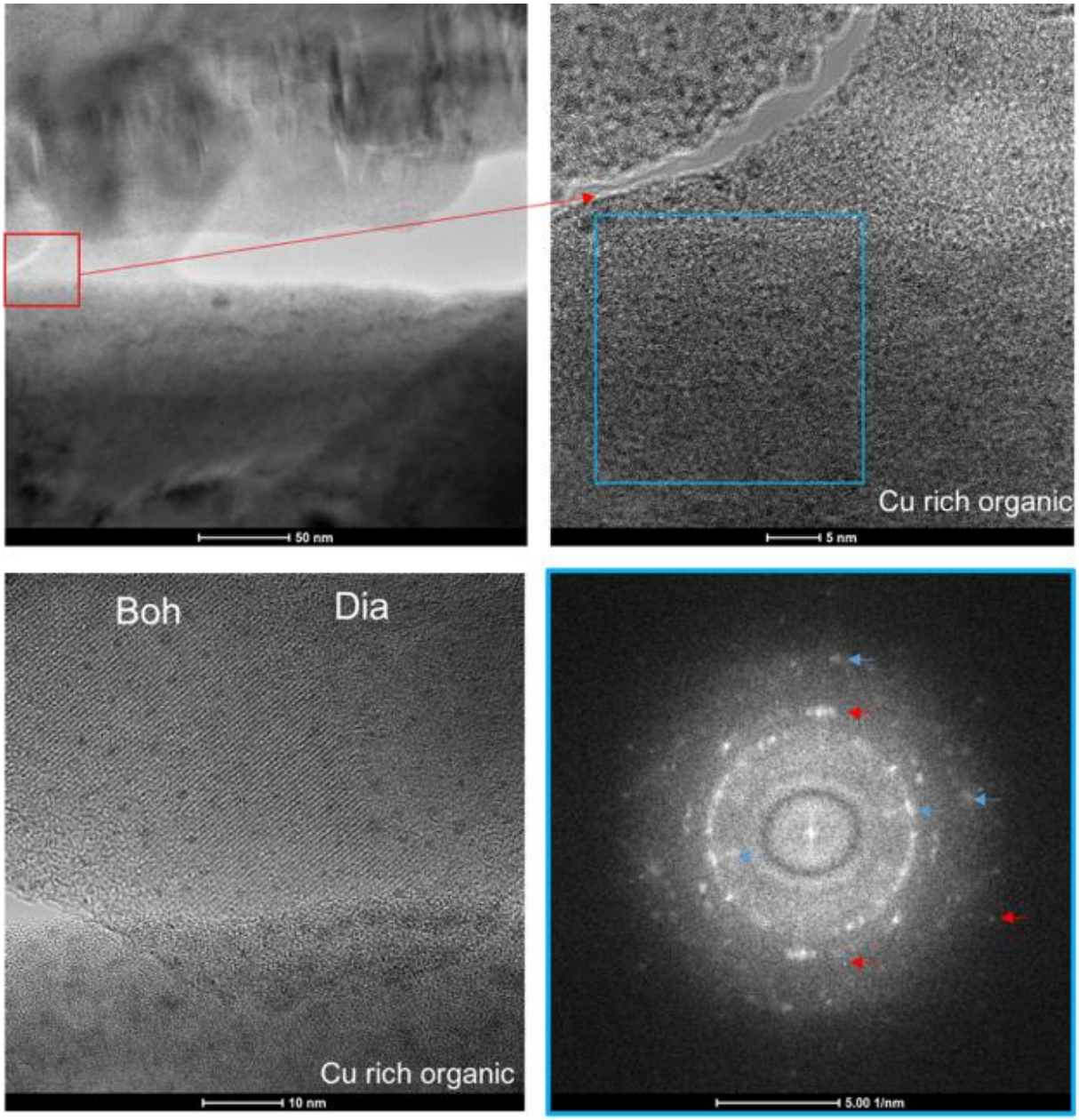

Metallic Cu d-spacings (Å)	Unidentified d-spacings (Å)
2.04	3.08
1.80	2.38
1.29	1.54
	1.40

Figure S13. Scanning-TEM images and fast Fourier transformation pattern of lattice fringes of nanoparticles within organic material and boehmite (Boh) and diaspore (Dia). Red arrows in FFT indicate metallic Cu, blue arrows indicate unknown d spacings.

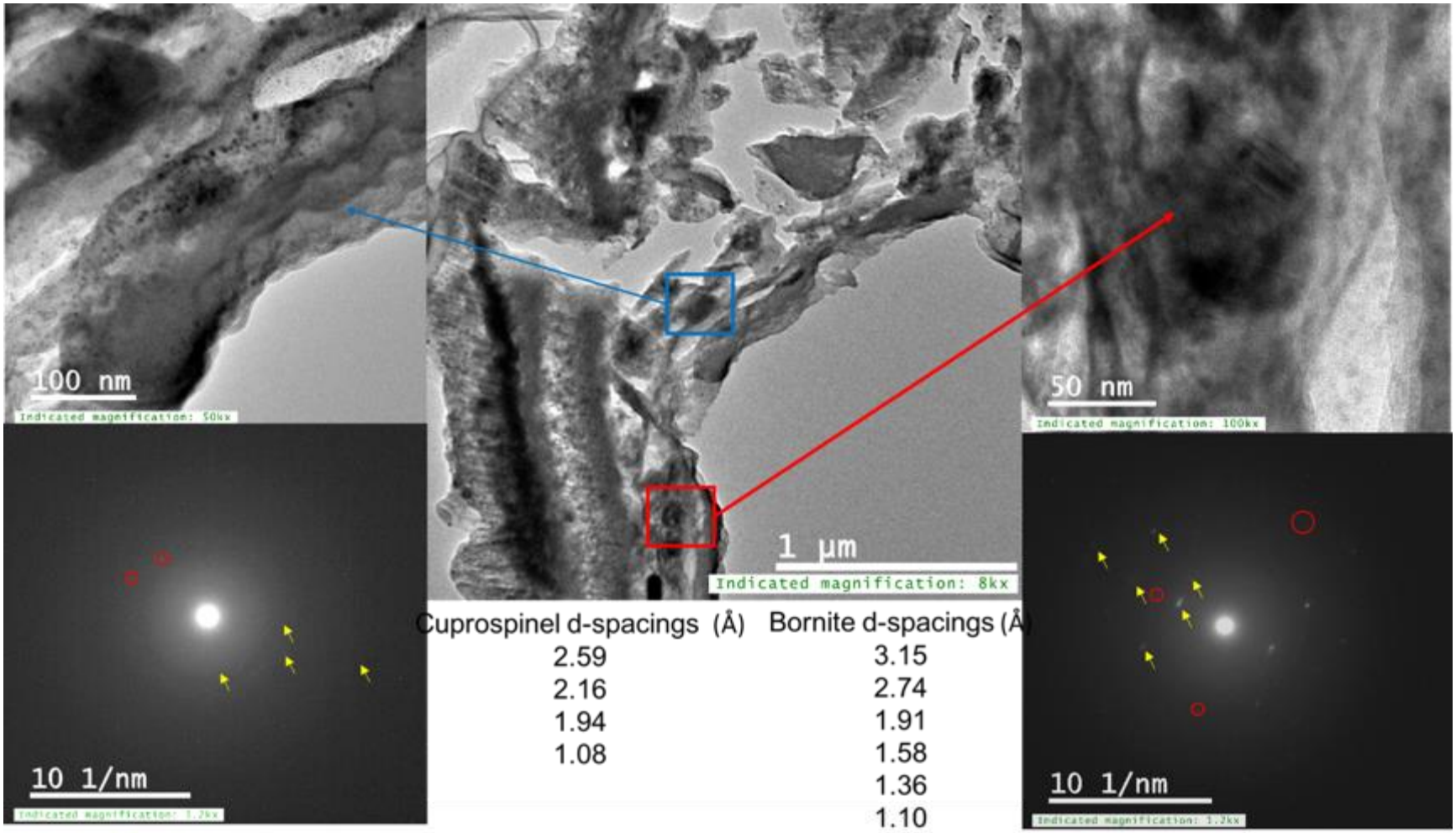

Cuprospinel d-spacings (Å)	Bornite d-spacings (Å)
2.59	3.15
2.16	2.74
1.94	1.91
1.08	1.58
	1.36
	1.10

Figure S14. Scanning-TEM images and SAED patterns of divalent copper minerals. Area highlighted in blue is cuprospinel + Cu^0. Area highlighted in red is bornite + Cu^0. Red circles in SAED patterns indicate metallic copper and yellow arrows represent the corresponding mineral.

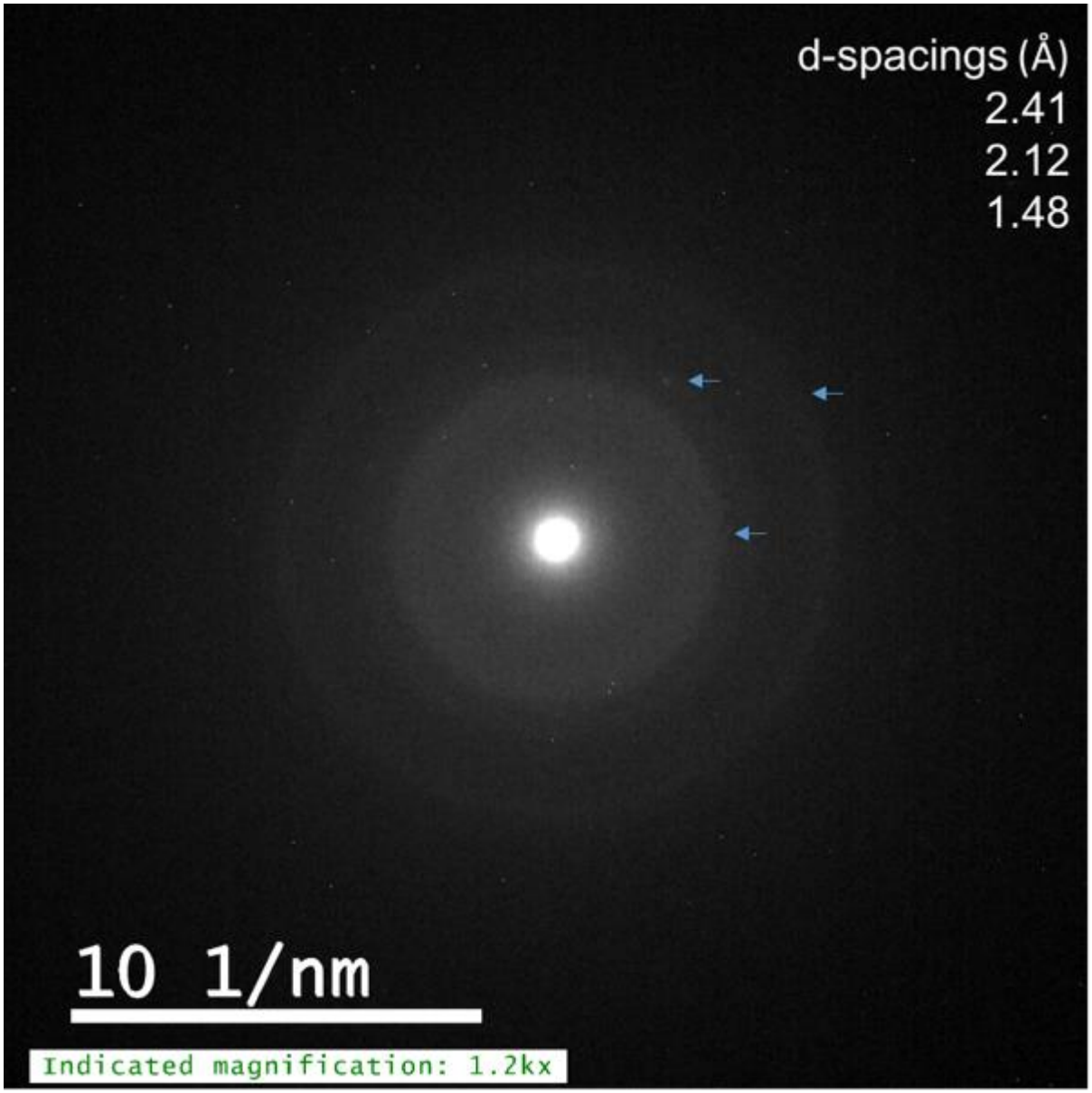

Figure S15. Selected area electron diffraction pattern of the iron oxide core surrounded by organic material.

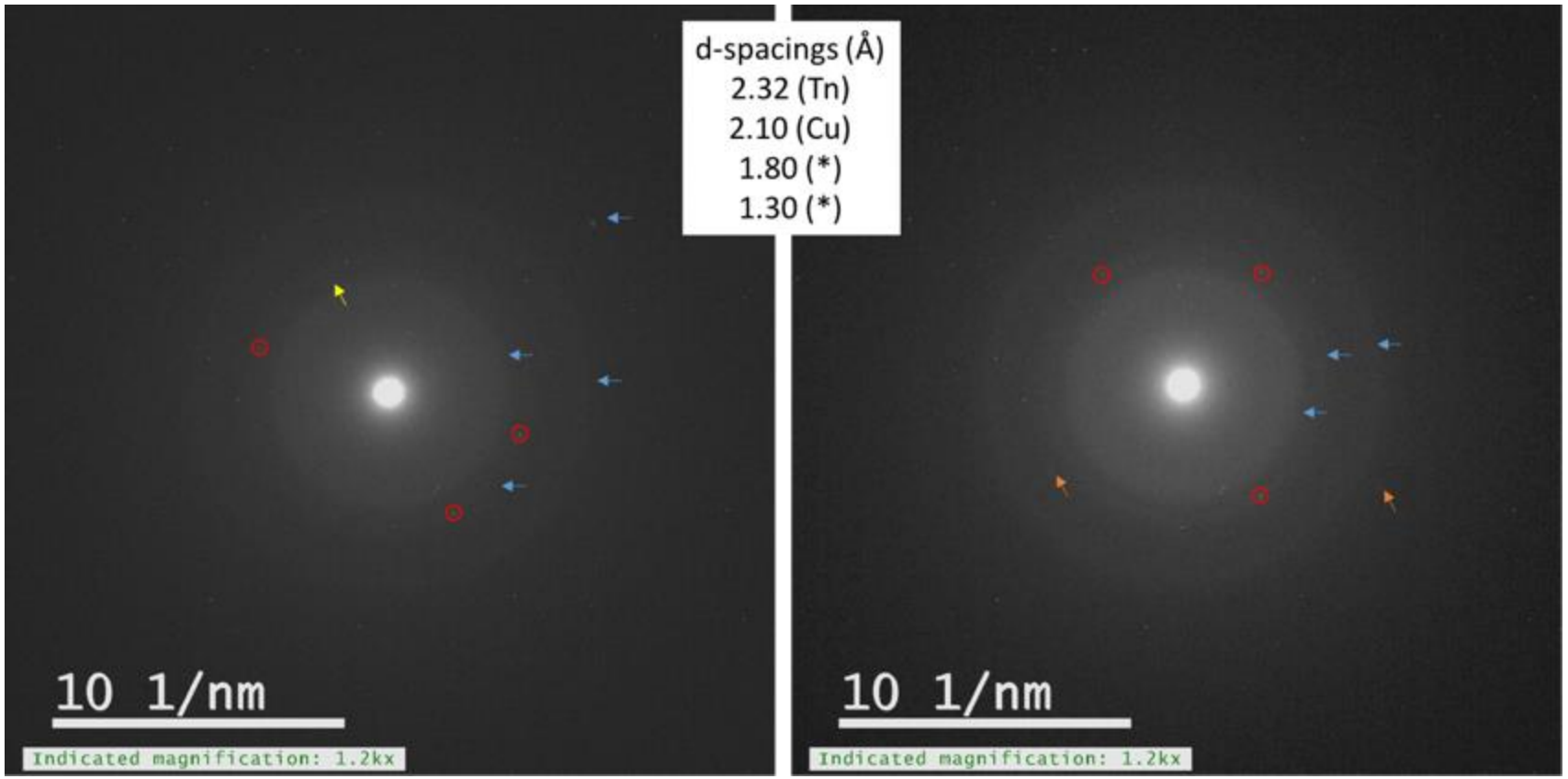

Figure S16. Selected area diffraction patterns of Cu-based nanoparticles within and surrounding the iron oxide core. Red circles indicate metallic Cu, yellow arrows indicate tenorite (Tn), orange arrows can be either metallic copper or tenorite (*), and blue arrows indicate magnetite/maghemite.

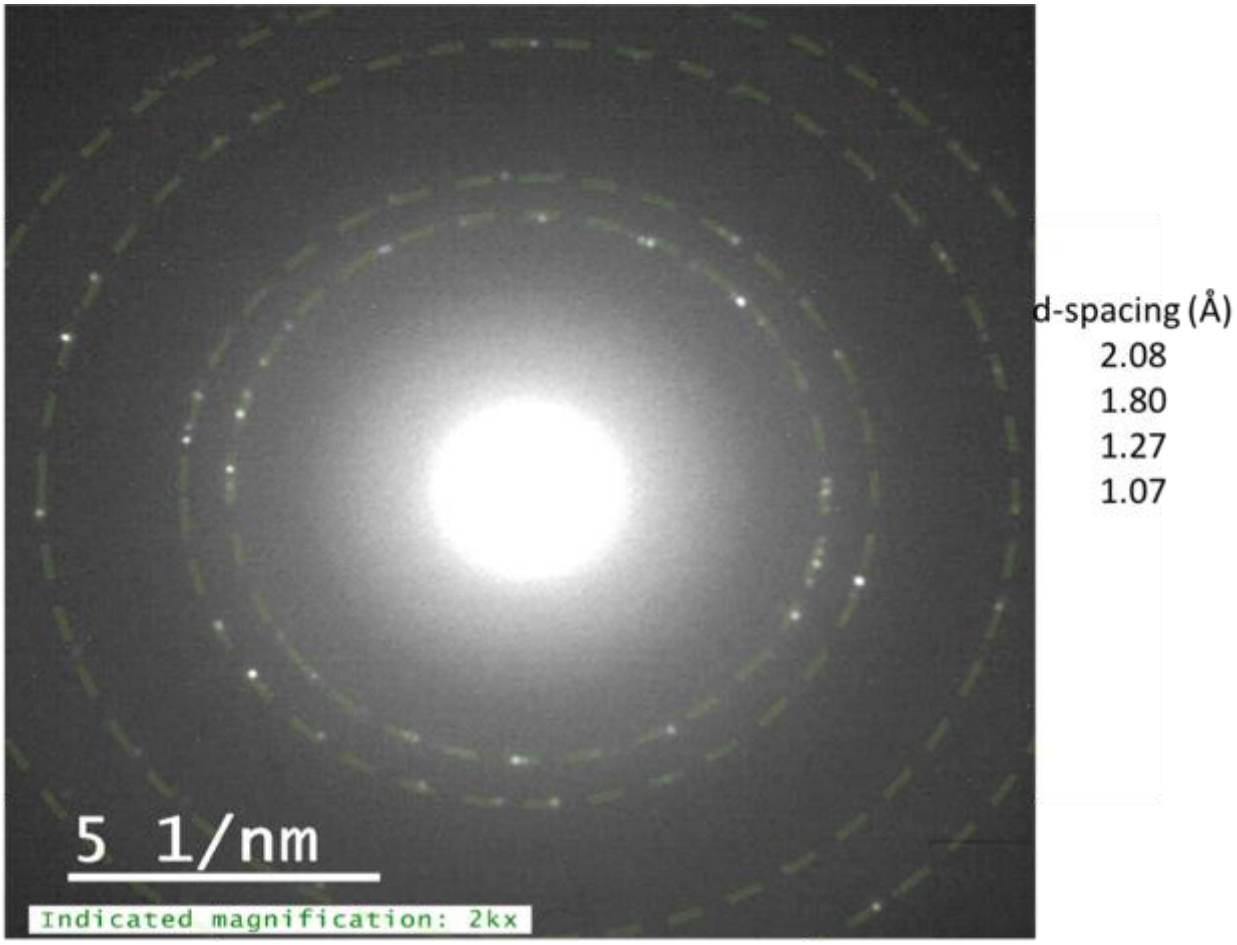

Figure S17. SAED pattern of Cu-based nanoparticles in the second FIB. The 3 green circles indicate the (111), (200), and (220) planes of metallic copper, while the fourth indicates the (311) plane which is sometimes listed in diffraction data.

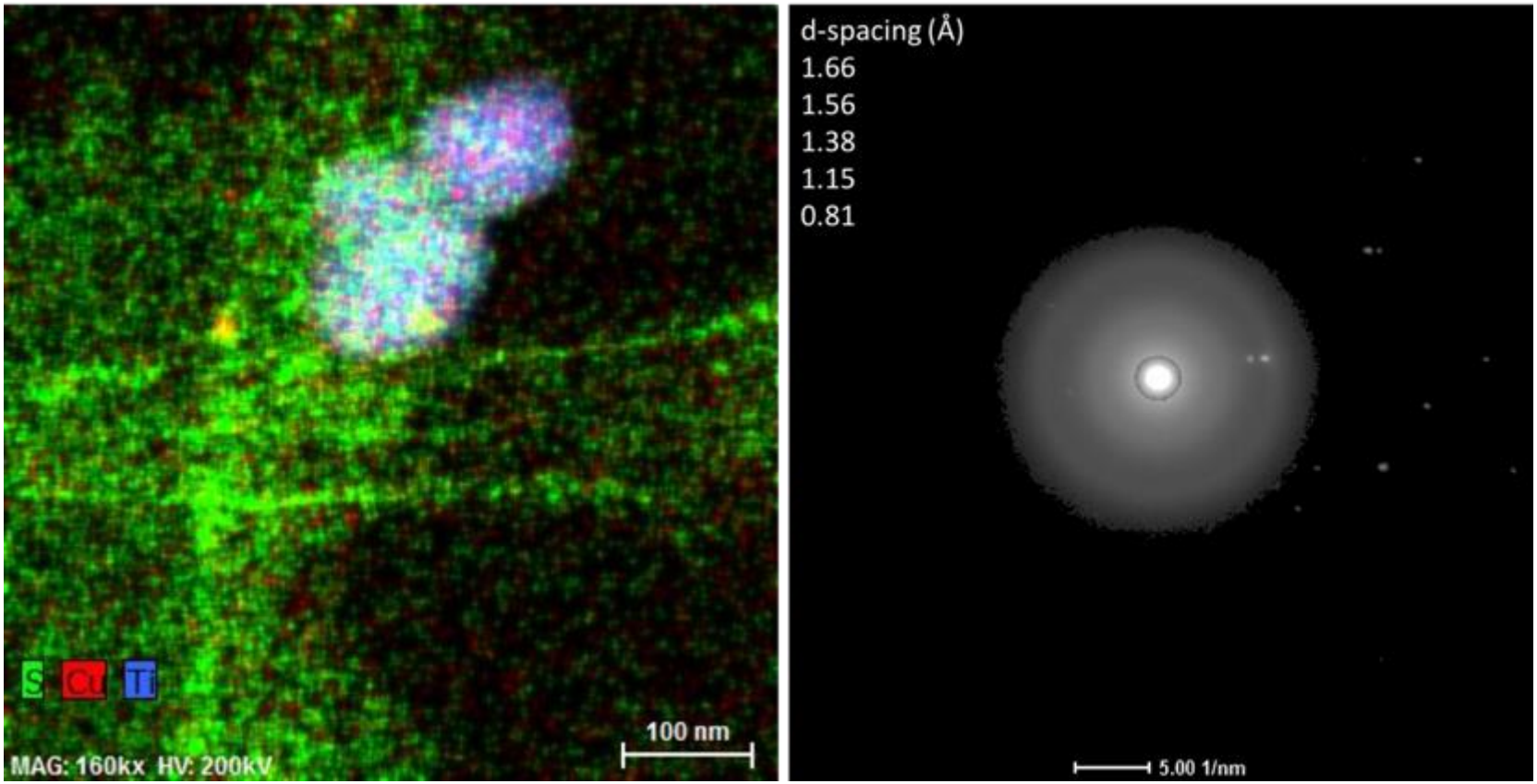

Figure S18. Scanning-TEM-EDS chemical distribution map showing the presence of copper sulfide (yellow) NPs on the titanium oxide colloid and the SAED pattern of the unidentified titanium oxide crystals.

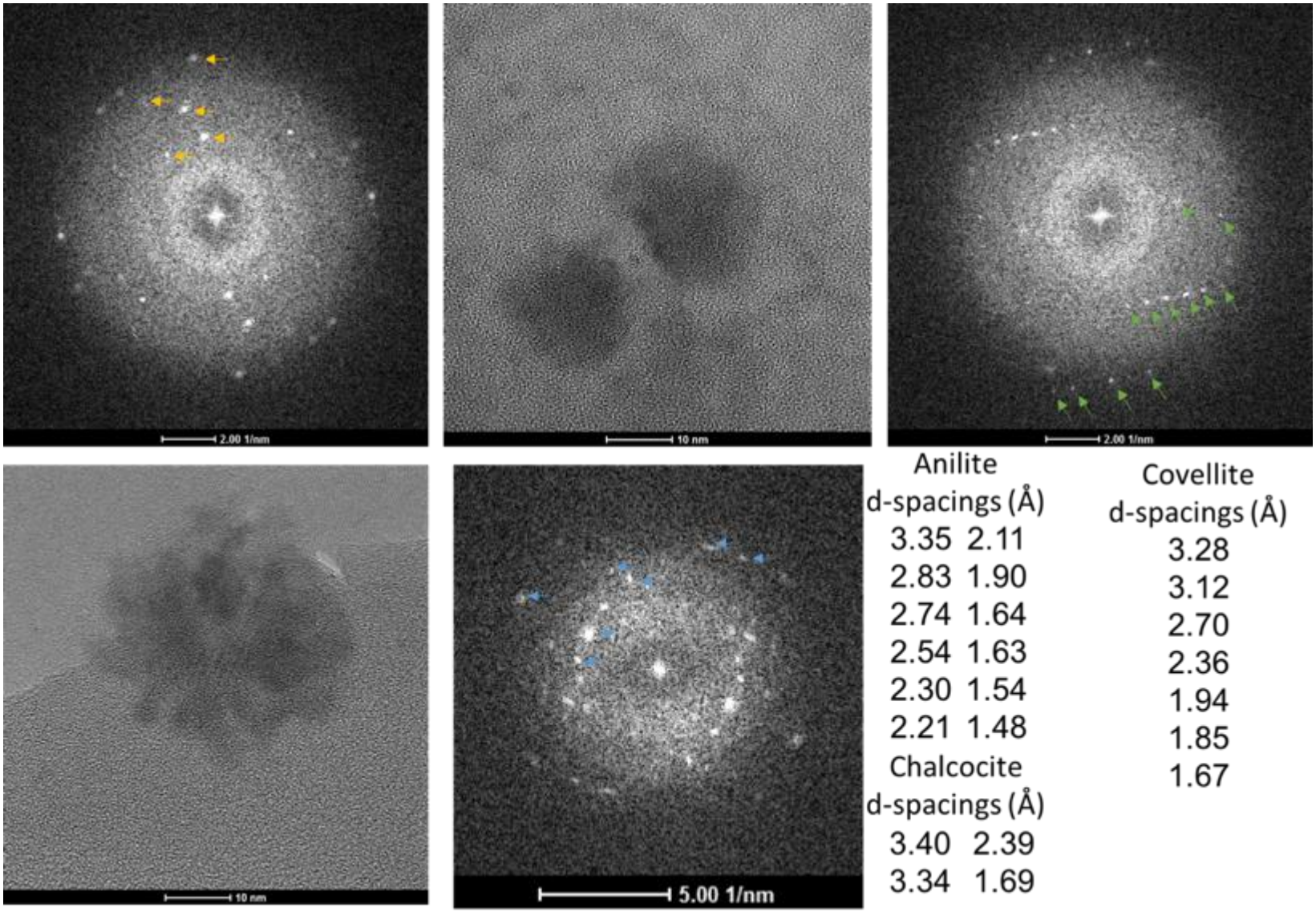

Figure S19. SAED patterns and corresponding STEM images of various Cu-bearing nanoparticles in the colloidal fraction. Arrows show prominent d spacings of chalcocite (orange), anilite (green), and covellite (blue).

Appendix B. The following is a compilation of data from the American Crystal Structure Database. All minerals discussed or identified in this study are indicated here, along with their respective d-spacing, *hkl* plane notations, and relative intensities.

Table B1. Diffraction data for anilite.[121,122]

Intensity	d-spacing (Å)	H	K	L
7.59	6.4133	1	0	1
2.98	6.3863	0	1	1
2.53	3.9450	2	0	0
13.51	3.9124	1	1	2
45.62	3.3563	2	1	1
24.26	3.3447	1	2	1
21.68	3.3276	1	0	3
13.26	3.3238	0	1	3
36.20	3.2066	2	0	2
10.47	3.1932	0	2	2
3.28	3.0631	1	1	3
1.32	2.9680	2	1	2
55.37	2.7807	2	2	0
19.34	2.7525	0	0	4
39.51	2.6960	2	2	1
10.49	2.6870	2	0	3
27.60	2.5989	1	0	4
3.62	2.5580	3	0	1
29.53	2.5427	0	3	1
18.90	2.5419	2	1	3
22.97	2.5368	1	2	3
8.56	2.4319	3	1	1
3.19	2.4201	1	3	1
21.54	2.3731	3	0	2
4.96	2.2617	1	3	2
19.36	2.2163	2	2	3
6.24	2.1787	2	3	0
47.40	2.1661	1	2	4
17.74	2.1423	3	2	1
6.62	2.1372	2	3	1
22.03	2.1288	0	3	3
8.49	2.1209	1	0	5
3.42	2.1200	0	1	5
9.09	2.0625	3	1	3
23.66	2.0553	1	3	3
21.31	1.9725	4	0	0
38.17	1.9600	0	4	0
100.00	1.9562	2	2	4
16.88	1.9416	4	0	1
4.41	1.9228	2	0	5
15.13	1.9015	3	0	4
2.98	1.8847	4	1	1
10.02	1.8768	3	2	3
6.18	1.8674	2	1	5
3.46	1.8654	1	2	5
1.20	1.8569	4	0	2
7.07	1.8479	3	1	4
2.06	1.8428	1	3	4
1.79	1.8069	4	1	2
11.16	1.7979	1	4	2
5.28	1.7553	2	4	0
8.99	1.7375	4	0	3
4.19	1.6963	4	1	3
4.04	1.6888	1	4	3
2.14	1.6884	3	0	5
1.05	1.6839	0	3	5
16.11	1.6781	4	2	2
15.77	1.6723	2	4	2
3.73	1.6638	2	0	6
11.13	1.6619	0	2	6
2.97	1.6547	3	3	3
2.16	1.6468	1	3	5
2.28	1.6276	2	1	6
1.04	1.6262	1	2	6
2.19	1.5884	4	2	3
1.77	1.5835	2	4	3
2.35	1.5744	4	3	0
13.67	1.5585	4	3	1
1.25	1.5558	3	4	1
1.35	1.5523	0	5	1
9.92	1.5506	3	2	5
1.13	1.5487	2	3	5
9.54	1.5425	1	0	7
1.46	1.5421	0	1	7
2.68	1.5169	5	0	2
1.53	1.5137	4	3	2
1.29	1.5135	1	1	7
3.52	1.4800	2	4	4
3.38	1.4469	4	3	3
1.22	1.4447	3	4	3
7.21	1.4445	2	5	1
3.20	1.4395	1	4	5
2.54	1.4363	2	1	7
1.55	1.4184	1	5	3
9.28	1.4147	5	2	2
3.56	1.3903	4	4	0
4.87	1.3794	4	4	1

2.96	1.3758	4 2 5
3.04	1.3726	2 4 5
1.69	1.3648	3 4 4
3.32	1.3558	1 0 8
4.13	1.3543	2 5 3
2.07	1.3408	5 3 1
1.43	1.3368	3 5 1
4.08	1.3284	1 3 7
2.50	1.3067	0 6 0
3.59	1.3002	4 4 3
3.95	1.2880	6 1 1
1.16	1.2827	5 0 5
6.91	1.2813	1 2 8
4.50	1.2807	4 3 5
4.89	1.2763	3 2 7
4.59	1.2753	2 3 7
3.31	1.2677	5 3 3
2.93	1.2644	3 5 3
2.68	1.2552	1 6 2
2.35	1.2388	6 2 1
2.49	1.2334	2 2 8
3.96	1.2194	3 0 8
2.09	1.2163	1 6 3
1.77	1.2152	2 5 5

3.49	1.2127	5 3 4
6.05	1.2121	1 4 7
3.40	1.2097	3 5 4
1.75	1.2089	1 0 9
1.80	1.2049	3 1 8
1.40	1.2035	1 3 8
1.33	1.1993	3 3 7
1.28	1.1805	6 2 3
2.09	1.1804	0 6 4
1.32	1.1732	6 1 4
1.00	1.1641	4 5 3
1.29	1.1636	3 6 1
3.22	1.1446	3 6 2
1.38	1.1411	2 5 6
2.77	1.1357	6 2 4
4.31	1.1309	2 6 4
1.52	1.1287	4 0 8
2.32	1.1223	5 4 4
2.69	1.1175	6 1 5
2.91	1.1140	5 0 7
1.76	1.1042	7 0 2
2.07	1.0996	1 5 7
1.29	1.0972	1 3 9
1.38	1.0920	6 4 0

Table B2. Diffraction data for boehmite.[123]

Intensity	D-spacing (Å)	H K L
100	6.1070	0 2 0
42.9	3.1605	1 2 3
0.1	3.0535	0 4 0
0.1	2.7920	0 1 1
31.7	2.3446	0 3 1
0.2	2.2273	1 1 1
0.2	2.0357	0 6 0
3.4	1.9795	1 3 1
20.9	1.8596	0 5 1
14.1	1.8468	2 0 0
0.2	1.7828	1 6 0
4.4	1.7677	2 2 0
9.2	1.6610	1 5 1
0.1	1.5803	2 4 0
0.1	1.5403	2 1 1
2.9	1.5268	0 8 0
0.2	1.4906	0 7 1
7.7	1.4508	2 3 1
4.4	1.4340	0 0 2
0.2	1.4110	1 8 0
1.3	1.3960	0 2 2
5.3	1.3823	1 7 1
0.2	1.3678	2 6 0
8.2	1.3104	2 5 1
3.8	1.3058	1 2 2
0.1	1.2267	0 9 1
0.2	1.2246	1 4 2
0.6	1.2214	0 10 0
1.0	1.2069	3 2 0
1.8	1.1767	2 8 0
0.1	1.1642	1 9 1
2.2	1.1596	2 7 1
0.1	1.1419	3 4 0
2.5	1.1326	2 0 2
0.2	1.1265	3 1 1
0.1	1.1174	1 6 2
1.0	1.1136	2 2 2
0.2	1.0900	3 3 1

Table B3. Diffraction data for bornite.[121,124]

Intensity	D-spacing (Å)	H	K	L
38.80	3.1580	1	1	1
40.00	2.7350	2	0	0
100	1.9339	2	2	0
13.29	1.6493	3	1	1
8.97	1.5791	2	2	2
13.24	1.3675	4	0	0
4.53	1.2549	3	3	1
4.66	1.2331	4	2	0
4.66	1.2231	4	0	2
24.24	1.1166	4	2	2

Table B4. Diffraction data for chalcocite.[121,125]

Intensity	D-spacing (Å)	H	K	L
4.94	3.4927	1	0	0
39.48	3.3695	0	0	2
54.34	3.1009	1	0	1
64.68	2.4250	1	0	2
100	2.0165	1	1	0
91.09	1.8893	1	0	3
3.06	1.7463	2	0	0
30.30	1.7303	1	1	2
20.17	1.6847	0	0	4
3.14	1.5505	2	0	2
2.52	1.5174	1	0	4
6.76	1.3787	2	0	3
1.98	1.2955	2	1	1
3.36	1.2929	1	1	4
1.57	1.2574	1	0	5
5.33	1.2291	2	1	2
3.41	1.2125	2	0	4
5.57	1.1642	3	0	0
10.82	1.1381	2	1	3
1.68	1.1232	0	0	6
2.81	1.1004	3	0	2

Table B5. Diffraction data for metallic copper.[121,126]

Intensity	D-spacing (Å)	H	K	L
100	2.0860	1	1	1
45.55	1.8065	2	0	0
23.27	1.2774	2	2	0

Table B6. Diffraction data for covellite.[121,127]

Intensity	D-spacing (Å)	H K L
6.67	8.1800	0 0 2
1.22	4.0900	0 0 4
11.06	3.2874	1 0 0
14.95	3.2230	1 0 1
44.86	3.0503	1 0 2
100	2.8154	1 0 3
44.54	2.7267	0 0 6
9.47	2.3191	1 0 5
4.29	2.0987	1 0 6
4.57	2.0540	0 0 8
10.57	1.9048	1 0 7
62.56	1.8980	1 1 0
23.38	1.7364	1 0 8
1.23	1.6437	2 0 0
1.32	1.6355	2 0 1
4.35	1.6115	2 0 2
2.42	1.5908	1 0 9
12.58	1.5738	2 0 3
33.49	1.5578	1 1 6
1.60	1.4688	2 0 5
1.28	1.4647	1 0 10
5.47	1.3912	1 1 8
6.24	1.3551	1 0 11
2.39	1.3445	2 0 7
6.21	1.2812	2 0 8
2.68	1.2284	2 1 2
7.31	1.2115	2 1 3
1.00	1.1616	2 1 5
2.33	1.1028	2 0 11
3.75	1.1011	1 0 14
1.93	1.0971	2 1 7
5.75	1.0958	3 0 0

Table B7. Diffraction data for cuprospinel.[121,128]

Intensity	D-spacing (Å)	H	K	L
18.21	4.8310	1	0	1
28.47	2.9889	1	1	2
13.36	2.9000	2	0	0
64.89	2.6010	1	0	3
100	2.4864	2	1	1
17.92	2.4155	2	0	2
13.72	2.1825	0	0	4
21.42	2.0506	2	2	0
1.61	1.9363	2	1	3
4.87	1.7438	2	0	4
8.85	1.6909	3	1	2
14.47	1.6719	1	0	5
10.12	1.6103	3	0	3
25.69	1.5820	3	2	1
45.16	1.4945	2	2	4
19.68	1.4500	4	0	0
1.15	1.4078	3	2	3
1.91	1.3713	1	1	6
1.56	1.3046	3	3	2
2.83	1.3005	2	0	6
1.44	1.2969	4	2	0
4.26	1.2958	3	0	5
9.39	1.2665	4	1	3
5.09	1.2432	4	2	2
4.45	1.2077	4	0	4
1.83	1.1399	3	1	6
5.41	1.1240	2	1	7
1.77	1.1149	4	2	4
1.62	1.1007	5	1	2
5.40	1.0952	4	1	5
3.10	1.0912	0	0	8

Table B8. Diffraction data for diaspore.[121,129]

Intensity	D-spacing (Å)	H	K	L
8.00	4.7126	0	2	0
100	3.9875	1	1	0
6.42	3.2164	1	2	0
29.93	2.5570	1	3	0
1.73	2.4357	0	2	1
3.97	2.3893	1	0	1
8.50	2.3563	0	4	0
63.08	2.3161	1	1	1
46.13	2.1311	1	2	1
46.27	2.0773	1	4	0
1.75	1.9018	1	3	1
5.21	1.8148	0	4	1
1.38	1.7328	1	5	0
15.70	1.7116	2	1	1
2.54	1.6777	1	4	1
50.44	1.6328	2	2	1
12.63	1.6082	2	4	0
2.29	1.5709	0	6	0
5.75	1.5225	2	3	1
24.35	1.4799	1	5	1
5.73	1.4316	2	5	0
16.85	1.4226	0	0	2
3.50	1.4006	3	2	0
3.31	1.4000	2	4	1
19.49	1.3752	0	6	1
6.59	1.3399	1	1	2
7.61	1.3292	3	3	0
4.74	1.3038	3	0	1
1.68	1.2915	3	1	1
5.47	1.2876	1	7	0
1.95	1.2785	2	6	0
4.41	1.2566	3	2	1
5.53	1.2432	1	3	2
2.26	1.2179	0	4	2
5.20	1.2042	3	3	1
7.61	1.1737	1	4	2
3.18	1.1408	3	4	1
1.05	1.1002	4	0	0
4.84	1.0928	4	1	0

Table B9. Diffraction data of maghemite.[121,130]

Intensity	D-spacing (Å)	H	K	L
1.30	4.8093	1	1	1
33.71	4.9451	2	2	0
100	2.5116	3	1	1
4.00	2.4047	2	2	2
16.89	2.0825	4	0	0
11.16	1.7004	4	2	2
21.09	1.6031	5	1	1
7.03	1.6031	3	3	3
40.17	1.4725	4	4	0
4.00	1.3171	6	2	0
8.18	1.2703	5	3	3
2.30	1.2558	6	2	2
2.02	1.2023	4	4	4
4.155	1.1131	6	4	2

Table B10. Diffraction data for magnetite.[121,131]

Intensity	D-spacing (Å)	H	K	L
7.93	4.473	1	1	1
28.10	2.968	2	2	0
100	2.5314	3	1	1
8.27	2.4237	2	2	2
20.13	2.0989	4	0	0
9.59	1.7138	4	2	2
29.94	1.6158	5	1	1
6.40	1.6158	3	3	3
41.80	1.4842	4	4	0
3.54	1.3275	6	2	0
8.82	1.2803	5	3	3
3.94	1.2657	6	2	2
2.62	1.2118	4	4	4
3.92	1.1219	6	4	2
8.92	1.0930	7	3	1
5.54	1.0930	5	5	3

Table B11. Diffraction data for mooihoekite.[121,132]

Intensity	D-spacing (Å)	H	K	L
3.84	7.4847	1	1	0
1.21	5.3830	0	0	1
1.90	5.2925	2	0	0
2.22	4.3702	1	1	1
3.27	3.7740	2	0	1
1.29	3.7424	2	2	0
2.55	3.3473	3	1	0
100	3.0727	2	2	1
2.27	2.8425	3	1	1
5.82	2.6915	0	0	2
10.94	2.6463	4	0	0
1.12	2.4949	3	3	0
1.44	2.2636	3	3	1
1.20	2.1667	4	2	1
1.37	2.0975	3	1	2
51.15	1.8870	4	0	2
24.80	1.8712	4	4	0
10.99	1.6180	2	2	3
20.84	1.5982	6	2	1
3.20	1.5364	4	4	2
3.25	1.3457	0	0	4
6.06	1.3231	8	0	0
6.65	1.2239	6	2	3
3.22	1.2152	6	6	1
5.60	1.0925	4	4	4